Modeling earthquake-fluid interaction:
shallow effects on groundwater circulation and induced seismicity in deep geothermal exploitation

Presentata da: MASSIMO NESPOLI

Coordinatore Dottorato:
Prof.
NADIA PINARDI

Relatore:
Dott.ssa
MICOL TODESCO
Correlatore:
Prof.
MAURIZIO BONAFEDE

ABSTRACT

Key words: Earthquake-fluids interaction, poro-elasticity, water well's level, numerical simulations, methane oxidation, permeability, porosity, injection-induced seismicity.

The interaction between earthquakes and crustal fluids is a very complex topic due to several mechanisms that are involved and which influence each other. Some phenomena, like the alterations of springs discharge rates and fluid flow, liquefaction and changing of the water levels in phreatic wells are largely documented in the literature, but their explanation is not yet fully clear. Furthermore, these phenomena can greatly change with the rock type, the earthquake magnitude and the observation distance from the fault. Within a distance of a few fault lengths from the epicenter, an earthquake can alter both the regional stress field and the hydraulic properties of the rocks, influencing the underground fluid distribution. In this thesis, I apply the numerical simulator TOUGH2 to represent the changes in water level of some wells after the $M_L 5.9$ earthquake that took place in Italy in 2012. The model shows that the wells response to the seismic event can be represented imposing a static stress change and highlights the role of the soil stratigraphy. This zone is also well known for localized methane seepages associated with anomalous soil temperatures. I simulate the process and draw some conclusions on the nature of this phenomenon and on the possible interactions with the local seismicity. Finally, I study the earthquake-fluid interaction from the opposite point of view: looking at how fluids can promote seismicity. I present the results obtained by coupling the TOUGH2 geothermal simulator with a stochastic

seed model of seismicity. The coupled simulation could capture the main characteristics of the seismicity induced by the fluid injection in a seismically active area.

CONTENTS

CONTENTS

INTRODUCTION

In this thesis different methods are presented to model the interaction between earthquakes and fluids. The modelling approach is based on the numerical simulator of multiphase fluid flow through porous media TOUGH2 (Transport Of Unsaturated Groundwater and Heat). Chapter 1 describes the simulator and its main equations. Earthquakes are well known to affect shallow and deep groundwater, but modelling this phenomenon is quite complex, due to the several mechanisms that contribute to the interaction. The effect of an earthquake on fluids depends to a first approximation on the magnitude of the earthquake, the geometry of the fault and the faulting mechanism and therefore requires a thorough knowledge of the seismic source. An accurate knowledge of the fault model, however is not sufficient by itself to reproduce the effect of the earthquake on fluids, which heavily depends also on mechanical and hydrological characteristics of the soil. A model adequately capable of representing this phenomenon must be able to consider with sufficient realism both the mechanical response of the soil to the earthquake, and the fluid dynamics. Chapter 2 reports the main theory background on the basis of the physics used in this thesis and a brief discussion of the literature about eartquake-fluid interaction. Chapter 3 presents an application of the TOUGH2 simulator to describe the groundwater flow associated with the $M_L 5.9$ mainshock of the 2012 seismic sequence in Emilia (Italy). The results of the simulations are compared with the water level evolution in both deep and shallow water wells in the area. In some cases the earthquake can instead

change a phenomenon that already occurs, such as the gas seepage through the soil, modifying the hydrological characteristics of the rocks. Chapter 4 illustrates the case of the Terre Calde di Medolla, literally "hot lands of Medolla" (Italy), close to the epicenter of 2012 mainshock. This area has been known since ancient times for the anomalous ground heating that prevents the accumulation of snow during the winter and for the diffuse methane seepage. The interest in this phenomenon has increased after the Emilia earthquake: I show that the heating mechanism can be unrelated to the seismicity of the area, although the earthquake may have enhanced it. In Chapter 5, I study the fluid-earthquake interaction the other way around, to model how fluids can affect the seismic activity. This chapter results from the coupling between the geothermal simulator TOUGH2 and an improved version of a stochastic seed model. A three-dimensional model is used to represent the stimulation of a deep geothermal reservoir with sufficient accuracy to grasp the main features of seismicity induced by human activity. In particular the accurate representation of the dynamics and thermodynamics of fluids of the TOUGH2 simulator, coupled with the representation of the stress field through the seed model, accurately reproduce both the temporal and spatial distribution of the events. In Chapter 6 I show the result of an application of the coupled model presented in the previous chapter. This chapter shows how to represent a real case of induced seismicity due to the geothermal activity in Basel (Switzerland). Starting from the data of the injection flow rates and from the stress field computed in literature I catch the temporal evolution of induced seismicity (magnitude and events occurrence) and the wellhead pressure.

CHAPTER 1

THE FLUID FLOW EQUATIONS

Contents

All simulations performed in this thesis were performed with the TOUGH2 geothermal simulator (Pruess et al., 1999). The simulator allows to represent the coupled flow of heat and fluid through porous media. The model accounts for the presence of different fluid components (water + non condensable gas(es)) and different fluid phases (gas and liquid), describing water phase changes and the dissolution/exsolution of non-condensible gas components in liquid water. The time is implicitly discretized with a finite difference method at first order and mass and energy are spatially discretized with the integral finite difference procedure. The computation follows the iterative method of Newton-Raphson. The simulator is able to represents with a good approximation most of the thermodynamic properties of a multiphase fluid, considering the effects of capillary pressure and the relative permeabilities of fluid phases. At each Newton-Raphson iteration the new phase conditions are computed in each grid blocks (or cell) and the primary variables are updated

accordingly. The fluid advection follows a multiphase Darcy law described in the following sections, while the heat flow depends on both conduction and convection, also accounting for latent heat in case of phase changes. The TOUGH2 simulator could be used with several equations of state (EOS), also called modules, which describe the properties of different fluid component(s). In the simulations presented in this thesis we used two different equations of state: the module EOS3 describes the transport of heat and two fluid components, air and water. We used this equation of state to simulate the eartquake-groundwater interaction in Chapter 3 and an improved version of this module was used in the THM coupling model presented in Chapter 5. To simulate the heating due to methane oxidation (Chapter 4), we used the EOS7C module (Oldenburg et al., 2004). This equation of state simulates multicomponent fluid mixtures with methane and another non condensible gas (carbon dioxide or nitrogen), water in aqueos and vapor phases and heat. The partitioning of non condensible gasses between aqueos and gas phases is computed with a chemical equilibrium approach, while the gaseous transport depends on advection and molecular diffusion.

1.0.1 TOUGH2 applications and alternatives

Thanks to the large number of equations of state, the TOUGH2 simulator offers a wide range of applications both in industry and in research, for example for studying geothermal energy (Borgia et al., 2011; Kim et al., 2015), natural gas reservoirs (Oldenburg et al., 2001), nuclear waste (Esha and Benedicta, 1996) and it is also used for simulations of hydrothermal circulation and volcanology (Todesco et al., 2010; Saibi, 2011; Rinaldi et al., 2010; Fournier and Chardot, 2012; Jasim et al., 2015). A powerful application of the TOUGH2 simulator was obtained coupling its source code with the geomechanical simulator FLAC. The TOUGH/FLAC simulator (Rutqvist, 2011) is suitable for studying the mechanical interaction between fluid and the porous matrix that in the normal version of TOUGH is assumed non deformable. In several works, the coupled model is used to simulate the CO_2 sequestration effects on fault reactivation (Rinaldi et al., 2015). Finally, the iTOUGH2 code (Finsterle, 1999) provides inverse modeling capabilities for the TOUGH2 simulator. The most used multiphase simulators, other than the TOUGH family, are SHAFT (Simultaneous Heat And Fluid Transport),

MULKOM (Multicomponent Model) (Pruess, 1982), FEHM (Finite Element Heat and Mass Transfer) (Kelkar et al., 2014) and HYDROTHERM (Kipp et al., 2008), but up to now TOUGH2 and FEHM simulators are the most widely used.

1.1 The Darcy law

The fluid flow in a porous medium is mainly driven by the pore pressure gradient and for an incompressible fluid it can be expressed by the Darcy equation, (Brown, 2002):

$$\mathbf{q} = -\frac{K_H}{\rho g}(\nabla p - \rho \mathbf{g}) \tag{1.1}$$

which relates the volumetric fluid flow $\mathbf{q}$ to the pressure gradient in excess of the hydrostatic value. In this equation, K_H is the *hydraulic conductivity* that can be expressed as a function of permeability k and fluid viscosity μ:

$$\mathbf{q} = -\frac{k}{\mu}(\nabla p - \rho \mathbf{g}) \tag{1.2}$$

Dimensionally, the vector $\mathbf{q}$ is a velocity, also called "*Darcy velocity*" and represents the volume of fluid that passes an area of one square meter in one second. This velocity differs from the fluid's particles speed $v = \mathbf{q}/\phi$, where ϕ is the porosity. In a multiphase system, the Darcy law must consider the different behaviour of the gas and liquid as well as phase interference: the generalized equation (1.5) in this case depends on properties of the two phases (Pinder and Gray, 2008).

$$\mathbf{q}_{gas} = -\frac{k_{gas}}{\mu_{gas}}(\nabla p_{gas} - \rho_{gas}\mathbf{g}) \tag{1.3}$$

$$\mathbf{q}_{liq} = -\frac{k_{liq}}{\mu_{liq}}(\nabla p_{liq} - \rho_{liq}\mathbf{g}) \tag{1.4}$$

To obtain a general form we can express equations 1.3 and 1.4 as

$$\mathbf{q}_\beta = -\frac{k_\beta}{\mu_\beta}(\nabla p_\beta - \rho_\beta \mathbf{g}) \tag{1.5}$$

where the subscript β indicates the fluid phase, while k_β is the effective permeability of phase β. To compute the multiphase fluid flow we can introduce the relative permeability of the fluid phase β, $k_{r\beta}$ defined as the ratio between the effective permeability of the phase, k_β and the absolute permeability (the permeability of a single fluid phase flow). The relative permeability depends on the volumetric fraction occupied by the fluid phase.

$$k_{r\beta} = \frac{k_\beta}{k} \tag{1.6}$$

1.2   Mass conservation

Considering an arbitrary volume V_n and its surface area Γ_n we can represent the integral form of the mass conservation equation as:

$$\frac{d}{dt}\int_{V_n}\left(\phi\sum_\beta S_\beta\rho_\beta X_\beta^c\right)dV_n =$$

$$\int_{\Gamma_n}\left\{\sum_\beta X_\beta^c\left[-k\frac{k_{r\beta}\rho_\beta}{\mu_\beta}\left(\nabla p_\beta - \rho_\beta\mathbf{g}\right)\right] - \sum_\beta \rho_\beta\mathbf{F}\nabla X_\beta^c\right\}\cdot\mathbf{n}d\Gamma_n + \int_{V_n}q^c dV_n \tag{1.7}$$

For a easier discussion, can be useful to group some terms of this equation. We can define the mass accumulation term M^c as

$$M^c = \phi\sum_\beta S_\beta\rho_\beta X_\beta^c \tag{1.8}$$

where S_β represents the saturation (i.e. the volumetric fraction) of the fluid phase β and X_β^c is the mass fraction of component c in phase β. We can also introduce the mass flux term $\mathbf{F}_\beta$ of phase β, computed as the Darcy velocity multiplied by the density as

$$\mathbf{F}_\beta = \rho_\beta\mathbf{q}_\beta = -k\frac{k_{r\beta}\rho_\beta}{\mu_\beta}\left(\nabla p_\beta - \rho_\beta\mathbf{g}\right) \tag{1.9}$$

To obtain the total advective flux we have to sum the mass fluxes of each phase as

$$\mathbf{F}_{adv}^c = \sum_\beta X_\beta^c \mathbf{F}_\beta = \sum_\beta X_\beta^c \left[-k \frac{k_{r\beta}\rho_\beta}{\mu_\beta} \left(\nabla p_\beta - \rho_\beta \mathbf{g} \right) \right] \tag{1.10}$$

Now can be useful to isolate the term $\mathbf{F}_{dif}^c$ that represents the molecular diffusion (Gennes, 1983; Marsily, 1986).

$$\mathbf{F}_{dif}^c = -\sum_\beta \rho_\beta \mathbf{F} \nabla X_\beta^c \tag{1.11}$$

The diffusion $\mathbf{F}$ in our notation can be written as (Pruess et al., 1999).

$$\mathbf{F} = \phi \tau_0 \tau_\beta d_\beta^c \tag{1.12}$$

d_β^c is the molecular diffusion coefficient, τ_0 is the factor of tortuosity, dependent on the properties of porous medium, while τ_β depends on phase saturation. The whole fluid flux can be expressed as

$$\mathbf{F}^c = \mathbf{F}_{adv}^c + \mathbf{F}_{dif}^c \tag{1.13}$$

At this point we can rewrite equation 1.7 as

$$\frac{d}{dt} \int_{V_n} M^c dV_n = \int_{\Gamma_n} \mathbf{F}^c \cdot \mathbf{n} d\Gamma_n + \int_{V_n} q^c dV_n \tag{1.14}$$

This means that the time derivative of the integration of M^c over the volume must equal the integration of mass flux M^c over the surface Γ_n. If we want to simulate sink or sources we should add another terms q^c integrated over the volume. In the end the mass balance for each component can be written as:

$$\frac{\partial M^c}{\partial t} = -\nabla \cdot (\mathbf{F}^c) + q^c \tag{1.15}$$

1.3 The heat equation

The general heat equation for a multiphase and multicomponent fluid can be found starting from the general heat equation of fluid in a permeable media

(1.16).

$$\rho_f c_f \left(\frac{\partial T_f}{\partial t} + \mathbf{v} \cdot \nabla T_f \right) = \lambda_f \nabla^2 T_f \tag{1.16}$$

T is the temperature, c is the specific heat and λ is the thermal conductivity. The pedix "f" indicates the fluid phase. Instead, the heat equation for the solid phase can be expressed as

$$\rho_s c_s \left(\frac{\partial T_s}{\partial t} \right) = \lambda_s \nabla^2 T_s \tag{1.17}$$

where subscript "s" indicates the solid matrix. Now we can compute the density ρ_m and the thermal conductivity λ_m of the rock-fluid mixture (subscript m) as

$$\rho_m = \phi \rho_f + (1 - \phi)\rho_s \tag{1.18}$$

$$\lambda_m = (1 - \phi)\lambda_s + \phi\lambda_f \tag{1.19}$$

The rock-fluid mixture specific heat for one volume unit is

$$\rho_m c_m = \phi \rho_f c_f + (1 - \phi)\rho_s c_s \tag{1.20}$$

Multiplying equation 1.16 by ϕ and equation 1.17 by $(1 - \phi)$ and assuming the thermal equilibrium between the fluid and the porous rock we obtain

$$\rho_m c_m \frac{\partial T}{\partial t} + \rho_f c_f \phi \mathbf{v} \cdot \nabla T = \lambda_m \nabla^2 T \tag{1.21}$$

Finally, using $v = \mathbf{q}/\phi$ we can rewrite (1.16) as

$$\rho_m c_m \frac{\partial T}{\partial t} + \rho_f c_f \left(\mathbf{q} \cdot \nabla \right) T = \lambda_m \nabla^2 T \tag{1.22}$$

The heat equation generalized for multiphase system that consider avvection

and conduction could be written as (Todesco, 2008):

$$(1 - \phi)\, \rho_s c_s \frac{\partial T}{\partial t} + \phi \sum_\beta \frac{\partial \left(u_\beta \rho_\beta S_\beta\right)}{\partial t} + \nabla \cdot \left(\sum_\beta \mathbf{q}_\beta \rho_\beta h_\beta\right) - \nabla \cdot (\lambda_m \nabla T) - R_E = 0$$

$$(1.23)$$

where u_β and h_β respectively are the internal energy and the enthalpy of phase β, S_β is the phase saturation, while R_E is the energy sink (if it is negative) or source (if it is positive). Also in this case can be useful to group some terms of the equation and considering the heat as the last (NC+1) "component" of the fluid simulation we can define the energy accumulation term as

$$M^{NC+1} = (1 - \phi)\rho_s c_s T + \phi \sum_\beta S_\beta \rho_\beta u_\beta \tag{1.24}$$

Instead, the heat flux can be written in it's short form as

$$\mathbf{F}^{NC+1} = -\lambda_m \nabla T + \sum_\beta h_\beta \mathbf{F}_\beta \tag{1.25}$$

In Appendix 1 are reported further information about the discretization of these fluid flow equations in the TOUGH2 numerical simulator.

CHAPTER 2

EARTHQUAKES AND FLUIDS

Contents

The seismicity is closely linked to underground fluids. On one hand, the earthquakes can act on the saturated porous medium, mainly by changing the stress field in the rock; on the other hand, the increasing pressure of fluids

can facilitate the sliding of faults, triggering earthquakes in a seismic area. The influence of fluids in the subsoil in several cases can have a significant importance in the study of the seismicity of the area. The hydrological phenomena associated with an earthquake can very different:

- changing the stream flow and its direction

- generating or removing fluid springs

- producing shallow soil liquefaction

- changing the water level in wells

The full understanding of the earthquake-fluid interaction is not trivial because of the large number of processes that can act together to generate these phenomena like strain variations and changes of the stress field. An earthquake can also alter the hydraulic properties of the saturated rock, such as the permeability and the porosity, irreversibly changing the hydraulic characteristics of the subsoil. Changes in the stress field can easily lead to a pore pressure variation of the interstitial fluid and in first approximation the static stress variations induced by an earthquake have the greatest effects on the hydrology of the area surrounding the fault. The next sections report background information on static and dynamic effects of earthquakes on fluids, paying particular attention to the effects on the water level of wells.

2.1 Static and dynamic effects

2.1.1 Static stress: hints of poroelasticity

The theory of poroelasticity (Biot, 1941; Rice and Cleary, 1976) allows to compute the effects of the permanent stress changes on the porous medium. The theory of poroelasticity uses the following assumptions:

- Linearity of the constitutive equations

- Isotropy

- At equilibrium the relation between stress and strain are reversible

- The fluid flow follows the Darcy law

The drained conditions

For an elastic medium with no (or constant) pore pressure ($p = 0$) the strain tensor ϵ_{ij} can be written as function of stress tensor σ_{ij} as:

$$\epsilon_{ij} = \frac{1}{2G}\left[\sigma_{ij} - \frac{\nu}{1+\nu}\sigma_{kk}\delta_{ij}\right] \tag{2.1}$$

G is the rigidity of the porous medium while ν is the drained Poisson modulus. With the adjective "*drained*" we are assuming that the fluid contained in the pores can freely move from the volume element during the deformation. The opposite situation, in which the fluid cannot move from the volume element is called "*undrained*". To obtain a complete draining the porous matrix requires some time to equilibrate the pore pressure to the initial one. The water volume change v could be expressed thanks to the linearity as $v = \sigma_{kk}/3H_1$. In the linear approximation the effect of a pore pressure variation on the strain tensor can be written in a tensorial form as $\epsilon_{ij} = b_{ij}p$ (where the tensor b_{ij} is a multiple of the identity matrix I), or in a simpler way as $\epsilon_{ij} = p\delta_{ij}/3H_2$ (assuming no stress changes). $1/H_1$ and $1/H_2$ respectively represent the volume change of fluid (i) due to stress variation with a constant pore pressure and (ii) due to pore pressure variation with a constant stress. From the conservation of energy derives that $H_1 = H_2 = H$, and H is called Biot's constant. In a general situation where both stress and pore pressure change, we can obtain the final equations combining the deformation with constant pore pressure and the constant stress variations:

$$\epsilon_{ij} = \frac{1}{2G}\left(\sigma_{ij} - \frac{\nu}{1+\nu}\sigma_{kk}\delta_{ij}\right) + \frac{1}{3H}p\delta_{ij} \tag{2.2}$$

$$v = \frac{1}{3H}\sigma_{kk} + \frac{1}{R}p \tag{2.3}$$

$1/R$ is the fluid volume change in the matrix due to the rock dilatation for a unit pore pressure increase. Following these equations the deviatoric strain

$\epsilon'_{ij} = \epsilon_{ij} - \epsilon_{kk}\delta_{ij}/3$ does not depend on pore pressure so it is not necessary to discriminate between a drained/undrained rigidity. The drained Poisson modulus ($p = 0$) can be expressed as the following equation.

$$\nu = -\left[\frac{\epsilon_{22}}{\epsilon_{11}}\right]_{p=0} \text{ in uniassial tension with } \sigma_{11} \neq 0 \tag{2.4}$$

As in the field of elasticity we can define a drained compressibility and a drained Young modulus as

$$K = \frac{2G(1+\nu)}{3(1-2\nu)} \tag{2.5}$$

$$E = \left[\frac{\sigma_{11}}{\epsilon_{11}}\right]_{p=0} = 2G(1+\nu) \text{ (uniassial stress } \sigma_{11} \neq 0) \tag{2.6}$$

Defining a incompressibility of the solid phase K_s (the incompressibility of the rock matrix without pores), or the more general K'_s that considers the presence of isolated pores, we can obtain the Equation 2.7 directly from the Equation 2.2.

$$\frac{1}{H} = \frac{1}{K} - \frac{1}{K'}_s \tag{2.7}$$

The parameter $1/R$ (fluid volume change in the matrix due to the rock dilatation for a pore pressure increase of one unit), can be expressed as Equation 2.8, where v_0 is the initial fluid content.

$$\frac{1}{R} = \frac{1}{H} - \frac{v_0}{K''_s} \tag{2.8}$$

The parameter K''_s contains also the possibility of incomplete filling of the pores. Generally a reasonable approximation in geophysics is $K'_s = K_s = K''_s$ (all pores are saturated ad interconnected).

The effective stress

Now we can introduce the *effective stress* definition starting from a general configuration of stress and pore pressure. Thanks to the linearity of the

equations we can represent a general configuration of stress following two steps. Firstly we can impose that the confining pressure is equal to the pore pressure, as

$$\sigma_{ij}^{p \neq 0} = -p\delta_{ij} \tag{2.9}$$

Then we need to increase the stress value until it reaches the final value, as

$$\sigma_{ij}^{p=0} = \sigma_{ij} - \sigma_{ij}^{p \neq 0} = \sigma_{ij} + p\delta_{ij} \tag{2.10}$$

Also the total deformations can be found following two step, so

$$\epsilon_{ij}^{p \neq 0} = \frac{-p}{3K_s'}\delta_{ij} \tag{2.11}$$

$$\epsilon_{ij}^{p=0} = \frac{1}{2G}\left(\sigma_{ij}^{p=0} - \frac{\nu}{1+\nu}\sigma_{kk}^{p=0}\delta_{ij}\right) \tag{2.12}$$

The final expression of deformation can be expressed with few passages as

$$\epsilon_{ij} = \frac{1}{2G}\left(\sigma_{ij} - \frac{\nu}{1+\nu}\sigma_{kk}\delta_{ij}\right) + \left(\frac{1}{3K} + \frac{1}{3K_s'}\right)p\delta_{ij} \tag{2.13}$$

Isolating the isotropic and the deviatoric terms, we can rewrite the deformation as

$$\epsilon_{ij} = \frac{1}{2G}\left(\sigma_{ij} - \frac{1}{3}\sigma_{kk}\delta_{ij}\right) + \frac{1}{9K}\left(\sigma_{kk} + 3\frac{K}{H}p\right)\delta_{ij} \tag{2.14}$$

At this point can be very useful to define the "*effective stress*" as

$$\sigma_{ij}^{eff} = \sigma_{ij} + \frac{K}{H}p\delta_{ij} \tag{2.15}$$

Thanks to this assumption we can finally rewrite the deformation in a similar way of elastic unsaturated material equation as

$$\epsilon_{ij}^{eff} = \frac{1}{2G}\left(\sigma_{ij}^{eff} - \frac{1}{3}\sigma_{ij}^{eff}\delta_{ij}\right) + \frac{1}{9K}\epsilon_{ij}^{eff}\delta_{ij} \tag{2.16}$$

The undrained conditions

The undrained conditions are obtained on short time scales: in that period the fluid flow has not yet been able to change the initial mass m_0 of the fluid in the rock but only it's volume. Of course this assumption implies that the fluid is compressible. The mass variation can be expressed as:

$$\Delta m = m - m_0 = (\rho_0 + \Delta\rho)(v_0 + \Delta v) - \rho_0 v_0 \approx \rho_0 \Delta v + v_0 \Delta\rho \quad (2.17)$$

In this case we need to insert also a fluid compressibility $K_f = p\rho/\Delta\rho$ and the fluid volume change is computed from Equations 2.3 and 2.8.

$$\Delta v = \frac{1}{3H}(\sigma_{kk} + 3p) - \frac{v_0}{K_s''}p \quad (2.18)$$

Substituting Equation 2.18 into Equation 2.17 we obtain the equation for the mass variation.

$$\Delta m = \rho_0 \frac{v_0}{K_f}p + \frac{\rho_0}{3H}(\sigma_{kk} + 3p) - \rho_0 \frac{v_0}{K_s''}p \quad (2.19)$$

Imposing the undrained conditions means that $\Delta m = 0$. At this stage can be advantageus to define a new quantity B, called Skempton's coefficient (Equation 2.20.

$$B = \frac{\dfrac{1}{H}}{\dfrac{v_0}{K_f} + \dfrac{1}{H} - \dfrac{v_0}{K_s''}} \quad (2.20)$$

With the Skempton's coefficient we can express the pore pressure in a very elegant way (Equation 2.21).

$$p = -\frac{1}{3}B\sigma_{kk} \quad (2.21)$$

Usually the Skempton's coefficient is closer to 0 when the rock and the fluid are very compressible, while in the sedimentary rocks filled with liquid water $B \approx 1$ (Makhnenko and Labuz, 2013). Also the strain equation (2.2) can be

rewritten using the Skempton's coefficient (2.22) .

$$2G\epsilon_{ij} = \sigma_{ij}\delta_{ij}\left[\frac{3\nu + B(1-2\nu)(1-K/K_s')}{3(1+\nu)}\right] \tag{2.22}$$

Now, defining a new quantity called *undrained Poisson's ratio*, ν_u (Equation 2.23) we obtain the final and shorter expression (Equation 2.24).

$$\nu_u = \frac{3\nu + B(1-2\nu)(1-K/K_s')}{3 - B(1-2\nu)(1-K/K_s')} \tag{2.23}$$

$$\epsilon_{ij} = \frac{1}{2G}\left(\sigma_{ij} - \frac{\nu_u}{1+\nu_u}\sigma_{kk}\delta_{ij}\right) \tag{2.24}$$

When $B \approx 1$, $\nu_u \approx 1/2$, while with $B \approx 0$, $\nu_u \approx \nu$.

2.1.2 Dynamic strain

With "*dynamic strain*" we refer to the strain variations due to the passage of seismic waves. The effects of the dynamic strain cannot lead permanent poro-elastic changes but they can be sufficient to change the permeability and the porosity of the shallow crust rocks leading to a pore pressure redistribution (Wang and Manga, 2014). Several authors indicate the dynamic strains as the responsible for changes of water level in water wells, increasing stream discharge and hot spring temperature (Roeloffs, 1998; Brodsky et al., 2003; Wang and Chia, 2008; Rojstaczer et al., 1995; Wang et al., 2004). In all cases the seismic energy can dislodge or break the obstacles that prevent the fluid flow. The dynamic strain is strictly dependent on wave propagation and attenuation in the porous medium, and in saturated rocks the wave speed is frequency dependent (Manga and Wang, 2007). For a plane seismic wave the strain is the ratio between amplitude of particle velocity and the wave propagation speed (phase velocity) $v_{particle}/v_{phase}$. For a given wave with frequency f, $v_{particle} = A/(2\pi f)$ and the seismic strain amplitude is $A/(2\pi f v_{phase})$, where A is the acceleration (Manga et al., 2012).

2.1.3 The deformations

A deformation that occurs in undrained conditions can lead great pore pressure changes. Permanent deformation of soil and sediments already occur between static strains of 10^{-4}-10^{-3} (Manga and Wang, 2007), while with strains of 10^{-2} usually failure occurs. The effects of static strain on the rocks is different in loose or dense deposits. In the loose deposit, usually shear deformation cause rearrangement of grains into the pre-existing pores and this process lead to a soil volume reduction, called "*consolidation*". Viceversa, in denser soils the shear strain tends to move the grains increasing the porosity ("*dilatancy*"). When strain occurs in brittle rocks, it can lead to microcracks, shear zone and rupture. The deformation due to dynamic strain is affected by inertial forces and depends on loading rates and number of loading cycles (Manga and Wang, 2007). In this case the permanent deformations are not only dependent on earthquake magnitude but also on the frequencies and even small dynamic strain (10^{-6}) could be important.

2.1.4 Permeability and porosity changes

The permeability is a fundamental parameter that influences the fluid flow, according to the Darcy law (Equation 1.2). In a low permeability soil the overpressure generated by an earthquake can remain for a long period and the effects on deformations and on fluid flow could be visible after several days or months. The static stress variations induced by the earthquakes can act on the hydraulic properties of the soil changing both the permeability and the porosity. In David et al. (1994) a confining pressure was applied to several rock samples of sandstones saturated with distilled water. They found that the permeability-pressure relation can be suitably represented with an exponential function (Equation 2.25).

$$k = k_0 e^{-\gamma(p_{eff}-p_0)} \tag{2.25}$$

p_{eff} is the effective pressure (the difference between confining and pore pressure) and p_0 is the reference effective pressure, 0.1 MPa (about the atmospheric pressure). A large pressure sensitivity parameter γ indicates a fast decrease of permeability with the pressure. This equation was used by several authors like Evans (1997); Wibberley and Shimamoto (2003). However,

for our purpose it can be convenient to introduce also the relation between permeability and porosity (Equation 2.27), where ϕ and ϕ_0 are the porosity corresponding to permeabilities k and k_0.

$$k = k_0(\phi/\phi_0)^{\alpha_s} \tag{2.26}$$

The exponent α_s is called *porosity sensitivity* and its value for a given material represents the overlap of two main mechanism of permeability enhancement with opposite effects David et al. (1994):

- Grain crushing

- Cracking

The grain crushing leads to a loss of rock cohesion and to a collapse of pore spaces and in this case there is a lowering of permeability. The extensive cracking can instead increase the pore space and reduce the tortuosity of flow paths, leading to an increase of permeability. In sedimentary rocks, the importance of a mechanism with respect to the other one greatly depends on the clay content of the rock (the permeability decrease is smaller in rocks containing clay). Dynamic strain can also lead to permeability variations, its effects are more difficult to measure, primarily because of the high sampling rate required to measure them, so there is a smaller quantity of literature about this topic. However Elkhoury et al. (2006) proposes the following equation that linearly depend on the peak ground velocity.

$$\Delta k = Q\frac{v_{particle}}{v_{phase}} \tag{2.27}$$

The parameter Q represents the characteristics of aquifer. This equation can be used also for an estimation of the dynamic strain effects in water wells level changes (in this case Q reflects the property of the whole well and aquifer system).

2.1.5 Distance from the source

Generally the hydrologic responses to the earthquakes depend on the distance of the seismic source (Manga and Wang, 2007). To distinguish the effects of the

earthquake on the basis of the distance from the hypocenter, could be useful to indicate as *near field* the area within 1 fault length, *intermediate field* as the area within a radius of few fault lengths and *far field* the zone at many fault lengths.

Table 2.1: Hydrologic influences in the near, intermediate and far field.

Field	Distance	Main mechanisms
Near Field	$r \approx 1$ Fault length	Static and dynamic strains permeability changes
Intermediate field	Few Fault lengths	Static and dynamic strains permeability changes due to dynamic strain
Far Field	Many fault lengths	Dynamic strains

Only in the near field the permeability variations are so effective to produce great changes of fluid path due to the combination of the static and dynamic strain. The static strain could be also important on the intermediate field but in the far field the dynamic strain prevails and it is the only mechanism that can lead to hydrologic responses.

2.1.6 Seismic energy density

The type and distribution of hydrologic responses could be roughly scaled with the earthquake magnitude M and the distance from the hypocenter r (Mogi et al., 1989; Roeloffs, 1998; Manga and Wang, 2007; Wang and Manga, 2010). Another useful parameter is the maximum seismic energy e contained in a unit volume, called "*seismic energy density*". This parameter is much easier to be compared with the laboratory measures. The expression of e is reported in Equation 2.28 (Wang and Manga, 2010; Lay and Wallace, 1995).

$$e = \frac{1}{2} \sum_i \frac{\rho}{T_i} \int v_i(t)^2 dt \qquad (2.28)$$

The i is the $i-th$ mode and T_i and v_i are the period and the particle velocity of each mode. The seismic energy density is proportional to the square of the PGV, *Peak Ground Velocity* (i.e. proportional to the dynamic strain) and can be estimated from the empirical Equation 2.29 (Wang and Manga, 2010;

Lay and Wallace, 1995).

$$\log r = 0.48M - 0.33 \log e - 1.4 \tag{2.29}$$

The dependence of hydrological effects on the magnitude M and on the distance from hypocenter, r is not a general law because the rock properies can be very different and the hydrological response to an earthquake also depends on the sensitivity of the rocks. The seismic energy density, instead is a more efficient parameter that allows a precise discrimination between the different hydrologic phenomena as reported in Table 2.2.

Table 2.2: Seismic energy density thresholds for earthquakes hydrologic responses.

$e\ (Jm^{-3})$	Hydrologic phenomenon
10^{-4}	Water-level changes; Triggered seismicity
10^{-3}	Groundwater changes
10^{-2}	Temperature changes in hot springs
10^{-1}	Streamflow increases; mud volcanoes; liquefation

Water level changes require a quite low energy density (from $10^{-4}(Jm^{-3})$), while the liquefaction and the mud volcanoes formation require an energy density greater than $10^{-1}(Jm^{-3})$.

2.2 Water level changes

The level of water wells reflects the pore pressure of the bottom holes. Observing the influence of the earthquakes on the wells can be useful to catch information about the groundwater system, the properties of the soil and the effects of the fault slip on the surrounding area. Several different kinds of response to the earthquakes were observed but we can distinguish between two different types:

- Level oscillations

- Poroelastic effects

2.2.1 Level oscillations

The passage of the seismic waves leads to oscillatory strain on the rocks. In case of fluid saturated rocks the pore pressure changes are proportional to the dilatational strain (Brodsky et al., 2003), that is mostly due to the Rayleigh waves. The pore pressure oscillations can be amplified from the water wells so their water level can also follow an oscillatory behaviour. Several cases of oscillatory water levels are reported by Brodsky et al. (2003). The $M_w = 7.1$ earthquake of 16 October 1999 (ground shaking of 1 mm/s) that hit the Hector Mine (California, USA) (Oglesby et al., 2003) caused water well level oscillations of about 10 cm (Figure 2.1). Another case of an oscillatory response was obtained after the Oaxaca (Mexico) $M_w = 7.4$ earthquake in 30 September 1999 (Singh et al., 2000). In that case the earthquake produced an instantaneous water level drop of 11 cm anticipated by small oscillations due to surface waves and followed by other oscillations. In this case the well is 3850 km far from the epicenter (very far field) and the static stress change could not have been the cause of the water level drop. A similar behaviour was obtained also in the $M_w = 7.9$ Denali (Alaska) earthquake, 3 November 2002 (Gomberg et al., 2004) with a great ground shaking of 4 mm/s where the earthquake led a water level drop of 12 cm followed by an oscillatory response. In this case the drop happened in correspondence of the passage of the Rayleigh wave. Another case of evident oscillatory behaviour was the $M_w = 8.4$ earthquake in Peru, the 2 June 2001 (Bilek and Ruff, 2002) that with a shaking of only 0.7 mm/s led to an oscillation with about 19 cm of amplitude. All of these cases show that wells can amplify the ground motions, particulary the long-period Rayleigh waves (Manga and Wang, 2007). A theoretical study of well amplification to the seismic waves was presented by Cooper et al. (1965).

2.2.2 Poroelastic effects

The coseismic step changes are the most frequent type of water level changes and several works focused on the importance of the coseismic static strain as the main mechanism to justify the well behaviour in the near and in the intermediate field. A perfect case to study coseismic changes is provided by the $M_w = 6.6$ Lushan earthquake on 20 April 2013 in Sichuan (China)
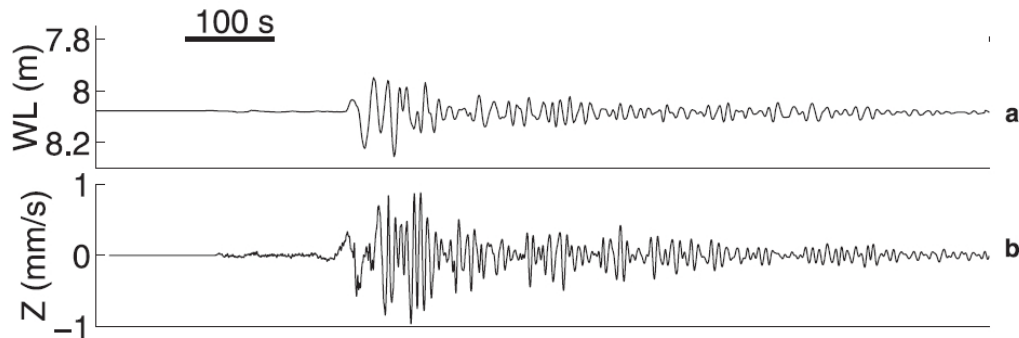
Figure 2.1: Hector Mine earthquake. (a) Water level response (b) z-component of seismogram. The figure is taken from Brodsky et al. (2003).

(Hao et al., 2013) and $M_w = 7.9$ Wenchuan (China) earthquake on 12 May 2008 (Lin et al., 2008). Several water well responses are provided by Shi et al. (2014) (Figure 2.2). Most of the water levels of the 12 wells had larger coseismic responses for the Wenchuan earthquake, up to 9.2 m and lower for the Lushan earthquake, up to 0.75 m. In the case of Wenchuan eartquake, the authors found a general pattern for water level changes: most of the wells along the fault strike generally had a fast increase, while wells placed in the fault sides had a level drop. They did not find a relationship between water level changes, magnitude and distance. Computing the coseismic strain field they found that generally there was a water level rise in contraction zone and a drop in dilated zone. This evidence is in agreement with the hypothesis that the static stress transfer in this case was the main mechanism that influenced the hydrologic response in the near field. In the case of the Lushan earthquake, there was no clear correlation between magnitude of static strain and water level change, so probably in that case the static strain was not the dominant mechanism. Other cases of strong correlation between poroelasticity and water level changes are reported by Akita and Matsumoto (2004) in connection with the $M = 8.0$ Tokachi-oki earthquake in Japan and by Lee et al. (2000) for the $M = 7.6$, 1999 Chi-Chi Taiwan earthquake. Finally Jónsson et al. (2003) found a strong co-seismic and also post-seismic correlation between water level and poroelasticity (Figure 2.3) for the two $M = 6.5$ earthquakes in the South Iceland on 2000. Using InSAR data they have shown that also the post seismic water level behaviour could be explained by the pore pressure recovery. In Chapter 3 I will show the water level evolution of some water wells in a time lapse around the 20 and 29 May 2012
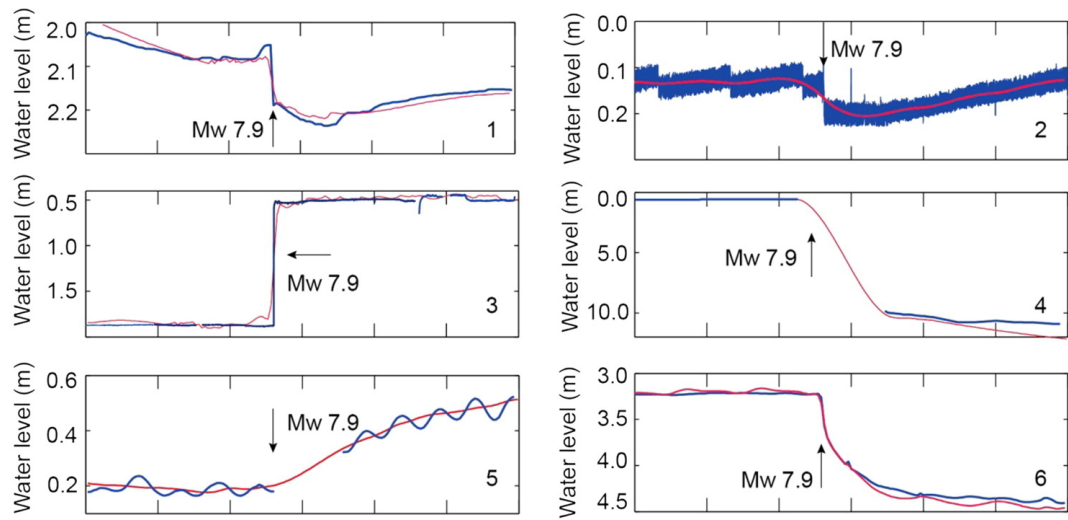
Figure 2.2: Water level evolution of 6 water wells in correspondence of Wenchuan earthquake. In the red curves tidal signals have been removed. Image modified from Shi et al. (2014).
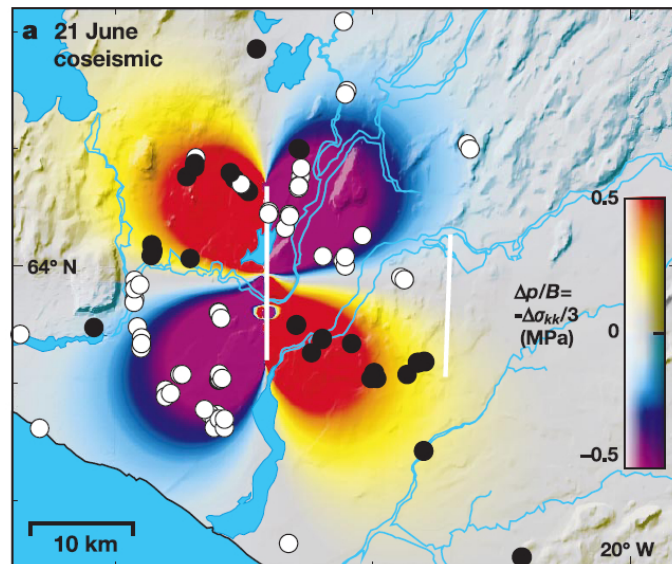

Figure 2.3: Coseismic water level changes in geothermal wells. The color represent the normalized pore pressure computed with the poroelasticity. Image taken from Jónsson et al. (2003).

earthquakes (M=5.9 and M=5.8) that struck Emilia Romagna (Italy). I shall show that also in this case the static stress change computed according to the theory of poroelasticity can explain the co-seismic hydrological response. We will see that the presence of several aquifers with different hydraulic properties can strongly influence the evolution of the pore pressure induced by the earthquake and a complete study of the water well behaviour must consider the soil stratigraphy.

2.3 The Mohr-Coulomb criterion

The Mohr-Coulomb criterion is a simple method to define the failure conditions of an isotropic material and therefore it is well suited to the study of induced seismicity. This method was applied in several physical and engineering works (Shuangyang et al., 2009; Cao and Zhang, 2005; Paterson and Wong, 2005; Palchik, 2006). The MC criterion uses the maximum σ_M and the minimum σ_m stress component that can be expressed in therms of normal (σ_n) and tangent (τ) stress component to the fault plane. The criterion can be expressed as Equation 2.30 (Labuz and Zang, 2012).

$$|\tau| = C + \mu_f |\sigma_n| \tag{2.30}$$

C is the "*cohesion*" acting as a shear strength, while μ_f is the "*friction*" that can be expressed as function of the friction angle, $\mu_f = \tan \Gamma$. Both parameters depend on the characteristics of the material. A geometric scheme of the Mohr-Coulomb criterion is shown in Figure 2.4. Equation 2.30 can be expressed as function of principal stresses as

$$\tau = \frac{\sigma_M - \sigma_m}{2}, \qquad \sigma_n = \frac{\sigma_M + \sigma_m}{2} \tag{2.31}$$

$$\sigma_M - \sigma_m = (\sigma_M + \sigma_m) \sin \Gamma + 2C \cos \Gamma \tag{2.32}$$

The failure occurs when the circle is tangent to the failure line, so in the MC criterion the medium stress component is not needed.
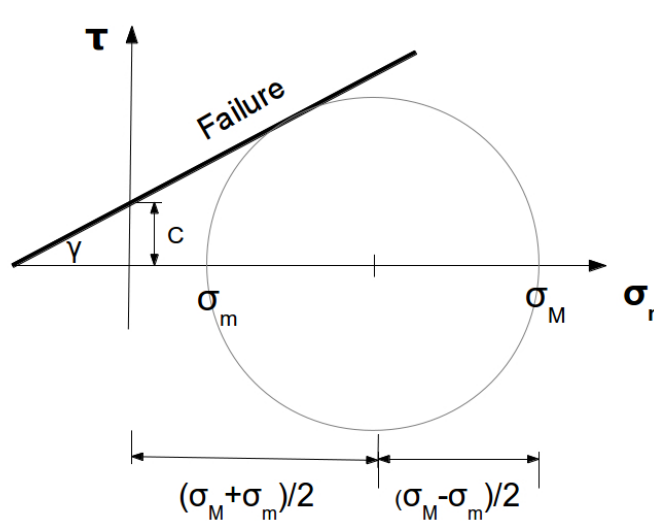
Figure 2.4: Scheme of the Mohr Circle.

2.3.1 Mohr Coulomb criterion in saturated material

The Mohr Coulomb criterion expressed in the previous paragraph must be modified to include the presence of fluids in the rocks pores. Starting from Equation (2.2), to express the failure condition for a saturated material, we must find a strain state with pore pressure that equals the critical strain state of the MC criterion without pore pressure, so:

$$\frac{1}{2G}\left(\sigma_{ij} - \frac{\nu}{1+\nu}\sigma_{kk}\delta_{ij}\right) + \frac{1}{3H}p\delta_{ij} = \frac{1}{2G}\left(\sigma_{ij}^{p=0} - \frac{\nu}{1+\nu}\sigma_{kk}^{p=0}\delta_{ij}\right) \quad (2.33)$$

By equating the deviatorics components we get:

$$\sigma_{ij} - \frac{1}{3}\sigma_{kk}\delta_{ij} = \sigma_{ij}^0 - \frac{1}{3}\sigma_{kk}^0\delta_{ij} \quad (2.34)$$

Instead, by equating the isotropic components:

$$\sigma_{kk} + \frac{3K}{H}p = \sigma_{kk}^0 \quad (2.35)$$

Substituting these results in Equation 2.33 we obtain that in the failure condition $\tau^{p=0} = \tau^{p\neq0}$ (here τ represents the tangential component of stress, not the stress tensor) and $\sigma_n^{p\neq0} = \sigma_n^{p=0} - \frac{K}{H}p$. The MC criterion in a saturated

rock can be written as Equation 2.36.

$$|\tau^{p \neq 0}| = C + \mu_f \left(|\sigma_n^{p \neq 0}| - \frac{K}{H}p \right) \tag{2.36}$$

The ratio K/H is about 1 when the material has several deformable pores and the Mohr-Coulomb criterion for a saturated material assumes its most widely used expression, Equation 2.37.

$$|\tau| = C + \mu_f \left(|\sigma_n| - p \right) \tag{2.37}$$

from Equation 2.37 we can derive that larger pore pressure facilitate the attainment of the failure.

2.3.2 The 3D formulation of MC criterion

In an arbitrarily oriented 3D stress field, the shear and the normal stress components to the fault can be found with several geometry passages (Zoback, 2010). Assuming that the stress field can be expressed as the following matrix:

$$\mathbf{S} = \begin{bmatrix} S_1 & 0 & 0 \\ 0 & S_2 & 0 \\ 0 & 0 & S_3 \end{bmatrix}$$

To express this stress field in a arbitrary oriented geographic coordinate system we need to perform an Euler rotation as follows:

$$\mathbf{S}_{geo} = \mathbf{R}_1^T \mathbf{S} \mathbf{R}_1 \tag{2.38}$$

$$\mathbf{R}_1 = \begin{bmatrix} \cos a \cos b & \sin a \sin b & -\sin b \\ \cos a \sin b \sin c - \sin a \cos c & \sin a \sin b \sin c + \cos a \cos c & \cos b \sin c \\ \cos a \sin b \cos c + \sin a \sin c & \sin a \sin b \cos c - \cos a \sin c & \cos b \cos c \end{bmatrix}$$

The three rotation angles are defined in the Table 2.3. To find the τ and σ_n components the stress tensor must be projected into the fault plane defined

Table 2.3: Three rotation angled for horizontal (strike dip) or vertical S_1 (dip slip)

Angle	Horizontal S_1	Vertical S_1
a	trend of S_1	trend of S_{Hmax} - $\pi/2$
b	- plunge S_1	- trend of S_1
c	rake S_2	0

by *strike* and *dip* angles.

$$\mathbf{R}_2 = \begin{bmatrix} \cos(Strike) & \sin(Strike) & 0 \\ \sin(Strike)\cos(Dip) & -\cos(Strike)\cos(Dip) & -\sin(Dip) \\ -\sin(Strike)\sin(Dip) & \cos(Strike)\sin(Dip) & -\cos(Dip) \end{bmatrix}$$

$$\mathbf{S}_{fault} = \mathbf{R}_2 \mathbf{S}_{geo} \mathbf{R}_2^T \tag{2.39}$$

The shear and the normal stress component can be easily found as follow:

$$S_n = \mathbf{S}_{fault}(3,3) \tag{2.40}$$

To find the shear stress we need to perform another rotation around the *rake* angle.

$$\mathbf{R}_3 = \begin{bmatrix} \cos(Rake) & \sin(Rake) & 0 \\ -\sin(Rake) & \cos(Rake) & 0 \\ 0 & 0 & 1 \end{bmatrix}$$

$$\mathbf{S}_{final} = \mathbf{R}_3 \mathbf{S}_{final} \mathbf{R}_3^T \tag{2.41}$$

$$\tau = \mathbf{S}_{final}(3,1) \tag{2.42}$$

The rake of the slip vector can be found following the Table 2.4. I applied this 3D Mohr-Coulomb criterion in our model of induced seismicity discussed

in Chapter 5.

Table 2.4: Three rotation angled for horizontal (strike dip) or vertical S_1 (dip slip)

Conditions	Rake
$S_{fault}(3,2) > 0 \wedge S_{fault}(3,1) > 0$ $\vee$ $S_{fault}(3,2) > 0 \wedge S_{fault}(3,1) < 0$	$\arctan\left(\dfrac{S_f(3,2)}{S_f(3,1)}\right)$
$S_{fault}(3,2) < 0 \wedge S_{fault}(3,1) > 0$	$180\,° - \arctan\left(\dfrac{S_f(3,2)}{-S_f(3,1)}\right)$
$S_{fault}(3,2) < 0 \wedge S_{fault}(3,1) < 0$	$\arctan\left(\dfrac{-S_f(3,2)}{-S_f(3,1)}\right) - 180\,°$

CHAPTER 3

MODELING EARTHQUAKE EFFECTS ON
GROUNDWATER LEVELS

Contents

The results shown in this chapter are published in Nespoli et al. (2015b).

Changes in water level are commonly reported in regions struck by a seismic event. The sign and amplitude of such changes depend on the relative position of measuring points with respect to the hypocenter, and on the poroelastic properties of the rock. I apply a porous media flow model (TOUGH2) to

31

describe groundwater flow and water level changes associated with the first ML5.9 mainshock of the 2012 seismic sequence in Emilia (Italy). I represent the earthquake as an instantaneous pressure step, whose amplitude was inferred from the properties of the seismic source inverted from geodetic data. The results are consistent with the evolution recorded in both deep and shallow water wells in the area, and suggest that our description of the seismic event is suitable to capture both timing and magnitude of water level changes. I draw some conclusions about the influence of material heterogeneity on the pore pressure evolution and I show that to reproduce the observed maximum amplitude it is necessary to take into account compaction in the shallow layer.

3.1   Introduction

Earthquakes are known to affect groundwater: this occurs when seismicity acts on saturated porous rocks, and the stress change is transferred from the solid grain to the interstitial fluids (Roeloffs, 1998; Ge and Stover, 2000; Manga and Wang, 2007). The seismic event then alters the distribution of the pore pressure within the aquifer, causing changes in water level and changes in the discharge of streams, springs or geysers. Co-seismic stress changes affect both the magnitude and the sign of the water level changes: here I assume that a negative stress change leads to rock compression, and hence to pore pressure increase, whereas positive stress changes, and the related rock expansion, lead to a pore pressure drop. When the seismically induced pressure gradients cause the mixing of different water bodies, changes of aquifer composition and temperature may also be recorded (Wang and Manga, 2010, and references therein). The aquifer poroelastic response to seismicity can extend to the post-seismic phase as shown in Iceland, where fluid set in motion by the earthquake drove transient deformation that was recorded by geodetic measurements and lasted a few months (Jónsson et al., 2003). Long-term effects can also be associated with permanent or transient changes in the properties of the rock, which may undergo undrained contraction, liquefaction or changes (both positive or negative) in porosity and permeability (Elkhoury et al., 2006; Manga and Brodsky, 2006; Manga et al., 2009, 2012; Shi et al., 2014). The observed hydrological changes reflect the coupling between mechanical and fluid-dynamic processes within the crust. Such coupling operates in both ways, as the presence of fluids

within the crust may itself trigger seismicity (Ellsworth, 2013; Grünthal, 2013, and references therein) and drive the evolution of aftershock sequences (Miller et al., 2004): the fluid pressure modifies the effective normal stress, therefore a pore pressure increase may favor the onset of seismicity, whereas a pressure drop may hinder it. Understanding the extent and functioning of this hydro-mechanical coupling is therefore useful for a proper assessment of seismic hazard, and has implications for all the industrial activities that involve massive fluid injection or withdrawal and the related growing concerns about the risk of induced seismicity. Several authors have focused on the co-seismic well response to static strain (Roeloffs, 1996; Roeloffs and Quilty, 1996; Grecksch et al., 1999; Ge and Stover, 2000; Jónsson et al., 2003; Shi et al., 2014) and explored dynamic effects associated with the passage of seismic waves (Roeloffs, 1998; Brodsky et al., 2003; Elkhoury et al., 2006; Wang and Chia, 2008; Wang et al., 2009; Weingarten and Ge, 2014; Shi et al., 2014). The hydrological effects of both static and dynamic stress changes are known to depend on magnitude and distance of the triggering earthquake (Wang and Manga, 2010, and references therein): in the near field (i.e., within a distance comparable to the size of the rupture along the fault) static and peak dynamic stress changes have a comparable magnitude, whereas in the far field (more than several times the size of the ruptured fault) permeability changes due to dynamic strain seem to control hydrological effects (Wang and Manga, 2010). Focusing on the near-field, some studies describe observed changes in water level and its temporal evolution based on the co-seismic static stress field (Ge and Stover, 2000; Jónsson et al., 2003). In this approach, the static stress change is used to compute the co-seismic pore pressure variation; its temporal evolution is then computed according to a diffusion equation over a homogeneous and uniform half-space (Ge and Stover, 2000). These results provided interesting insights on the hydro-mechanical coupling, although the details of the groundwater response cannot be entirely captured. In the present work, I take into account the effects of heterogeneous rock properties and the presence of an unsaturated region. The use of a multi-phase, multi-component porous flow model (TOUGH2, Pruess et al., 2012) allows us to track the groundwater flow and its temporal evolution within both confined and unconfined aquifers, accounting for the local geothermal gradient and for potential temperature changes associated with fluid migration. Following the approach described above, the effect of seismicity is represented as an instantaneous pore pressure change estimated from the static, coseismic,

33

strain field. The simulated effects on water level were tested against field data. Our case history is the seismic sequence that struck the plain of the Po river (northern Italy) in 2012 (Figure 3.1), for which hourly data on water level in monitored wells are available and display remarkable changes in the near-field (Figure 3.2). Here I provide information on both the seismic sequence and the observed water level changes, and present the results of numerical simulations.
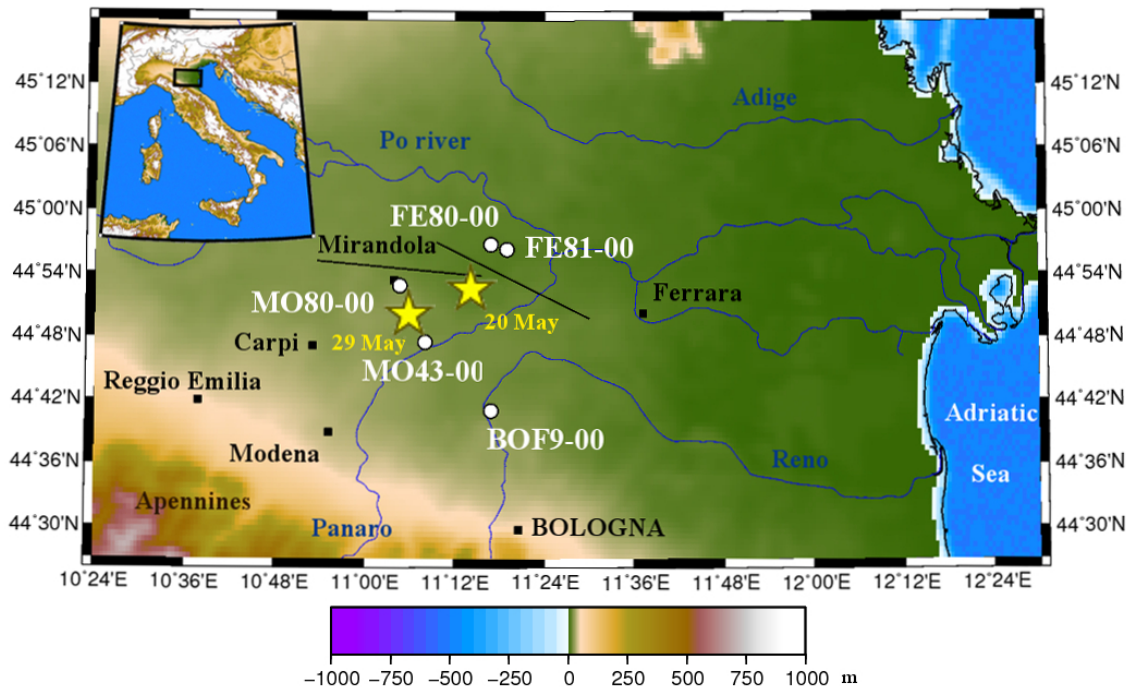
Figure 3.1: Map of the study area. White dots represent 5 water wells considered in this work; stars represent epicenters of two mainshocks of the 2012 Emilia seismic sequence; black lines represent the fault traces for the May 20 (north-east) and May 29 (to the west) events (Pezzo et al., 2013).

The first set of simulations focuses on the role of heterogeneity in controlling the aquifer response. I then evaluate the effects of compaction. The results show that:

- our representation of seismicity (i.e., the co-seismic deformation) within the groundwater model is adequate and provides a satisfactory description of the observed water level changes;

Figure 3.2: (a, e) Observed water level changes at different wells. Gray arrows indicate the events of May 20 and May 29, 2012. Note minor water level rise ("r" in figures 3.2 a,b) shortly after the first mainshock, in the shallow wells only.
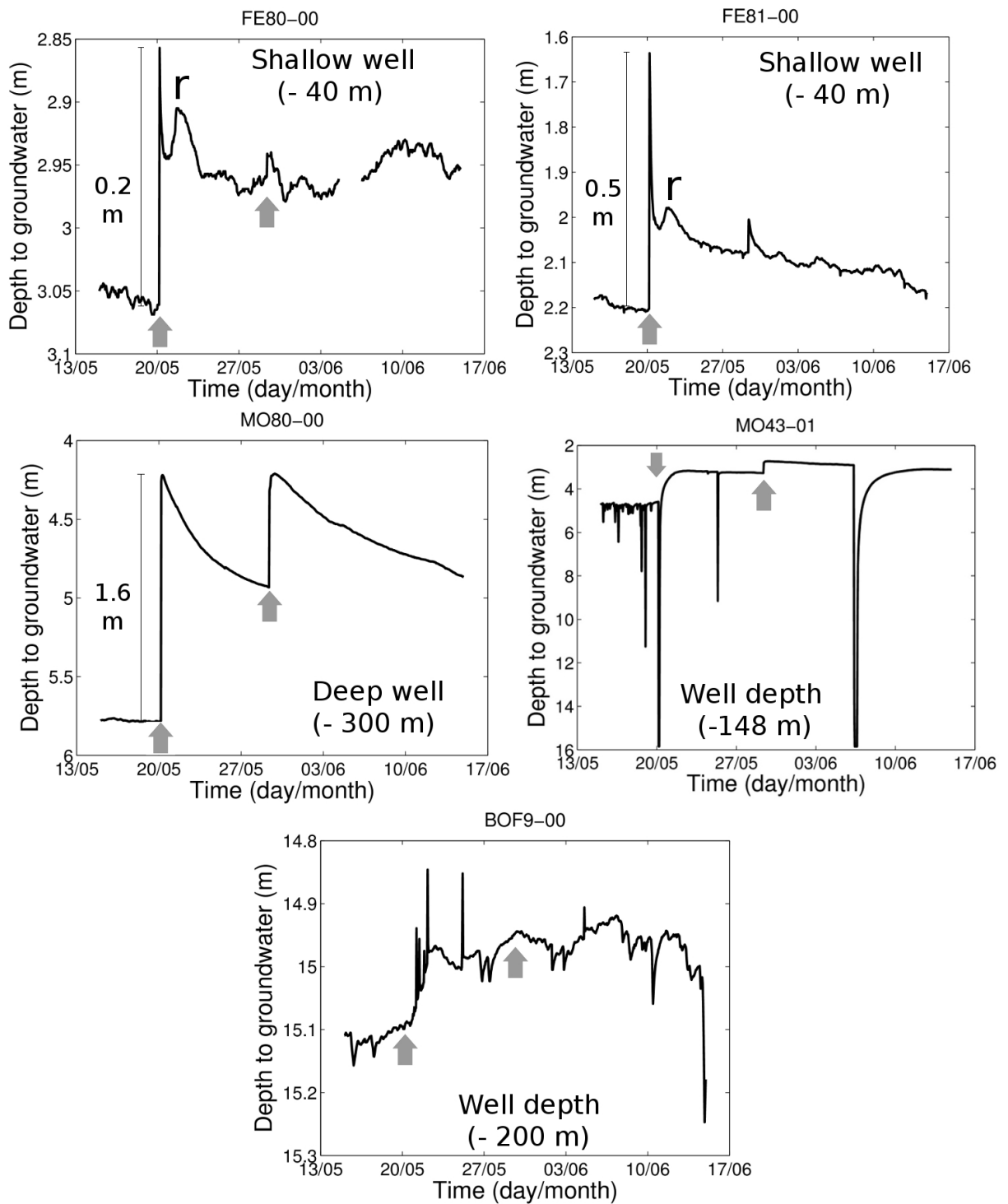
- heterogeneous rock properties control the different response observed at different wells;

- the details of the post-seismic water level evolution in shallow wells are better captured if the effects of rain fall and compaction are included.

3.2   The 2012 Emilia Seismic sequence

The seismic sequence that struck the Po Plain, Northern Italy, in 2012 (Figure 3.1), featured two main events: the first, on May 20 (4:04 AM, local time) with a magnitude ML=5.9, occurred near Finale Emilia at a depth of 6.3 km; the second took place on May 29 (9:00 AM, local time), 15 km southwest of the first event, near Mirandola, at a depth of 10.2 km and a magnitude ML=5.8 (Scognamiglio et al., 2012). Here I focus on the aquifer response to the May 20 event. The co-seismic slip associated with this event was inferred by various authors based on seismic and geodetic data (Cesca et al., 2013; Pezzo et al., 2013; Serpelloni et al., 2012). Here I consider the results by Pezzo et al. (2013), who performed a non-linear inversion of InSAR and GPS data, assuming dislocation in an elastic half-space, and a fault geometry constrained by geological and geophysical data. The resulting co-seismic slip is distributed along a fault model that has a surface trace of 34 km, a strike of 114 °and a rake of 90 °(Figure 3.3). According to Pezzo et al. (2013), the dip of the fault changes with depth, with a shallow and steeper portion (dipping 40 °SSW) that extends 11 km along dip, and a deeper and more gently dipping sector (20 °SSW) that extends 12 km along dip. The co-seismic slip, however, mostly occur on the upper portion of the fault, reaching a maximum value of 120 cm near its center (Figure 3.3).

3.3   Water wells response

The groundwater response to the seismic sequence was captured by the monitoring network of the regional agency for environmental protection (ARPA). The network consists of 40 instrumented water wells (Figure 3.4, Appendix C), evenly distributed across the region, that probe aquifers at different depths and provide hourly data on temperature, electrical conductivity and water level (Marcaccio and Martinelli (2012)). Only five wells, close to the

(a)

(b)
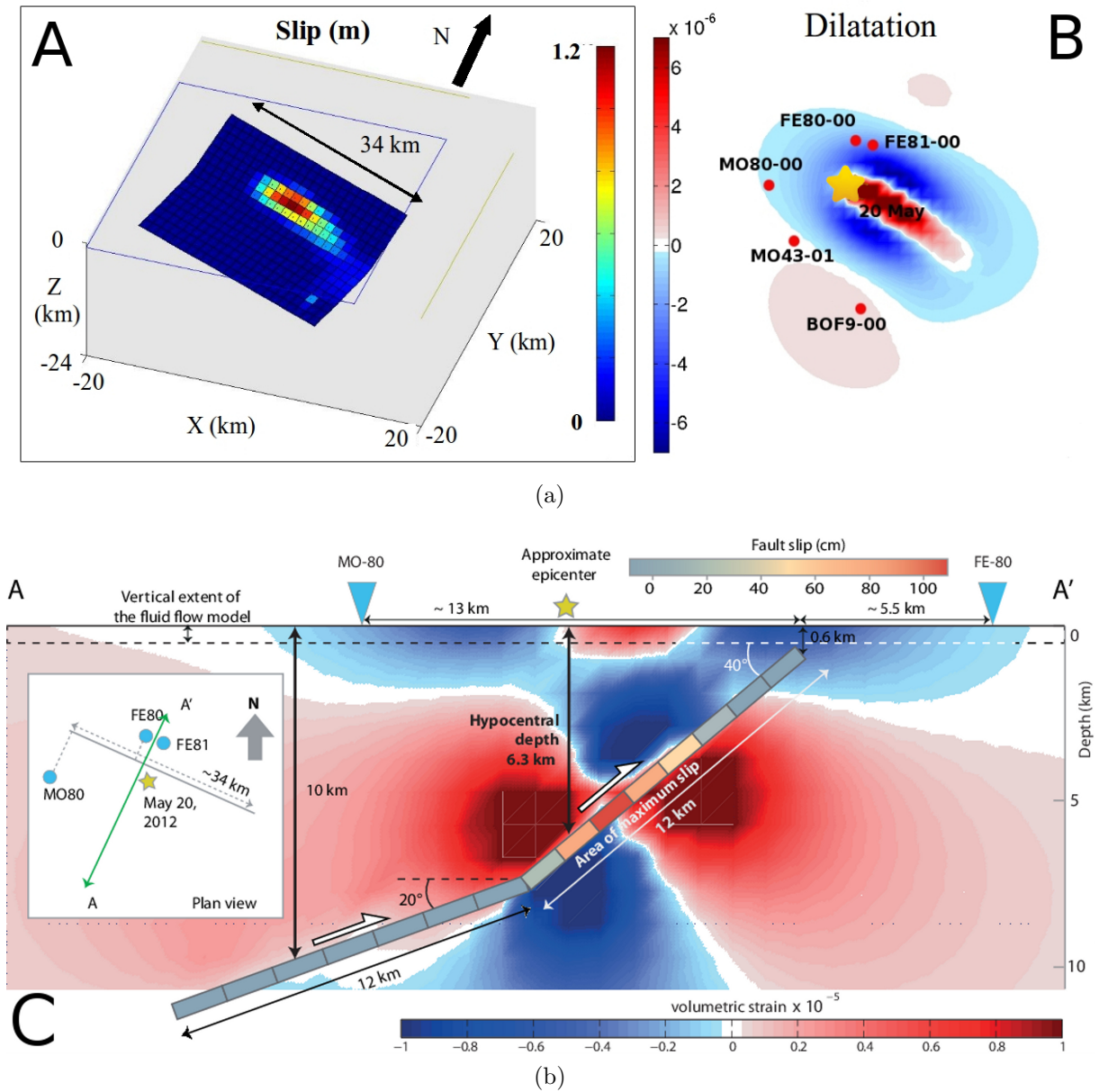
Figure 3.3: (a) Fault model of the May 20 earthquake, based on the inversion of GPS and InSAR data (after Pezzo et al. (2013)). Color represents the slip, which varies from 0 (blue) to a maximum of 1.2 m (red). (b) Volumetric strain at the surface computed for the May 20 earthquake. Computed strain ranges from ˘$6 \cdot 10^{-6}$ to $24 \cdot 10^{-6}$. Red dots represent the wells, and the yellow star represents the epicenter of the May 20, 2012 event. (c) Spatial relations between the inferred fault, slip distribution and water wells in the area. Panel (c) also highlights the different depths at which volumetric strain and fluid flow are computed.

Figure 3.4: Maps of the Emilia-Romagna region. Diamonds represent the water wells of the monitoring network of the regional agency for environmental protection (ARPA)

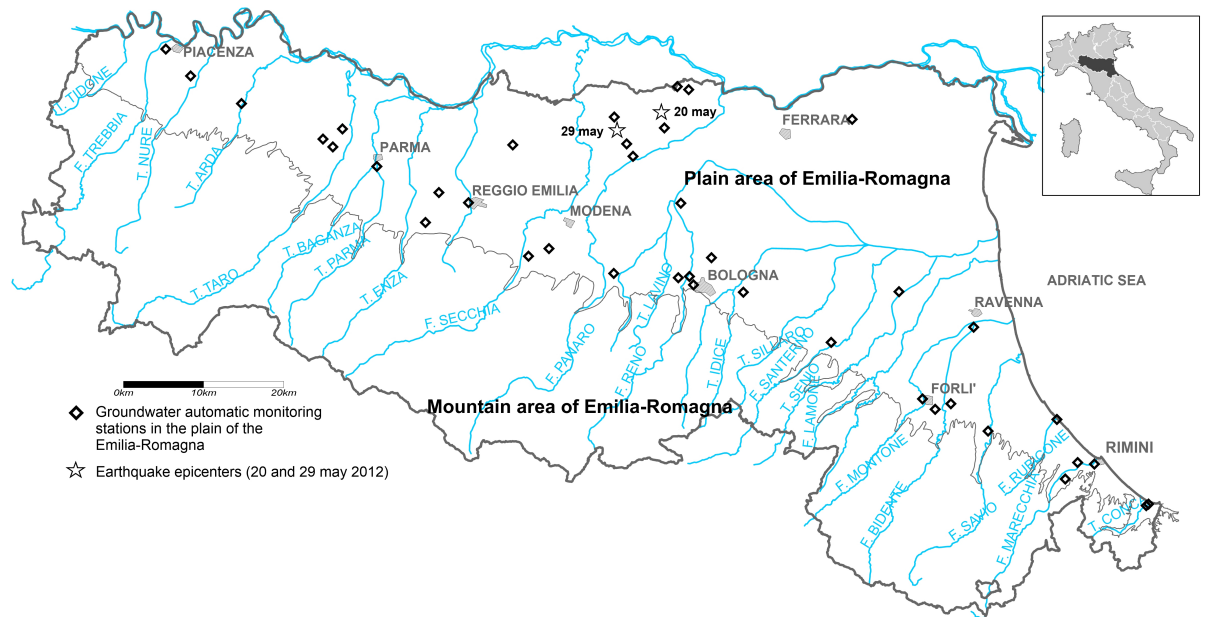epicentral area (Figure 3.1), recorded significant water level changes after the earthquake, suggesting that the seismic effects on the groundwater system are local. I cannot exclude far-field effects, sometimes associated with dynamic strain, owing to the low sampling rate ($1\ h^{-1}$) in these wells . In this area, the Po Plain is characterized by fine deposits that form superimposed, confined aquifers, while phreatic aquifers, sensitive to meteoric recharge, are only present at shallow depths (tens of m). The five wells that responded to the seismic events reach different depths (from -40 to -300 m) and all experienced a water level rise (Figure 3.2). No well in the entire network recorded a water level drop or a change in water temperature or salinity (Marcaccio and Martinelli, 2012). The temporal evolution of water level changes is shown in Figure 3.2 for the period from May 13 to June 17, 2012. The first measurement after the earthquake on May 20, took place about one hour after the event (5:00 AM, local time). The northernmost wells (FE80-00 and FE81-00) are both shallow (-40 m) and less than 3 km apart; their evolution is similar: water level undergoes an instantaneous increment (0.2 and 0.5 m, respectively) after the first earthquake. Then the water level

quickly drops, but doesn't recover its pre-earthquake elevation in the time span considered in this work (about a month). After the peak, both these wells feature a second water level rise (labeled r in Figure 3.2 A,B), lasting a couple of days, unrelated to seismicity, and that is not recorded in the other, deeper wells. Finally a second peak, equally sharp but of lower magnitude, corresponds to the second mainshock, on May 29, and is again followed by a slow decay. Greater changes are observed in the deepest well (MO80-00, 300 m), where the May 20 earthquake caused an instantaneous water level rise of 1.6 m, followed by a slow, partial recovery (Figure 3.2 C). A similar behavior is observed after the May 29 event, when the peak is followed by a slightly slower decline. More than three months were necessary in this case to restore the original water level. A response to the seismic activity can be identified also at wells MO43-01 and BOF9-00 (Figure 3.2 D,E). However, both these wells undergo heavy withdrawal associated with nearby industrial activities that were disrupted by the earthquake. The level rise observed after the earthquake is delayed more than one day and its amplitude is small compared to the extraction-related fluctuations and much larger than expected coseismic effects. As precise information on water withdrawal is not available, data from these wells are not considered hereafter. In the following, I focus on some specific features of the observed water level evolution :

1. the differences in water level changes between the shallow and deep wells;

2. the change in the decay rate during the post-seismic stage;

3. the residual level rise that characterizes the shallow wells after the May 20 earthquake;

4. the minor water level change observed in the shallow wells two days after the earthquake.

At this time, I limit my study to the effects associated with the mainshock of May 20, 2012.

3.4   Modeling the water response

3.4.1   The earthquake

In this work, I assume that the water level change is triggered by stress transfer from the rock to the pore fluid caused by the deformation of the matrix skeleton (Ge and Stover, 2000; Jónsson et al., 2003). Such stress transfer translates into a pressure change that can drive fluid motion. To describe this effect for the May 20 mainshock, I consider the fault model (in terms of coseismic slip distibution and fault geometry) described by Pezzo et al. (2013) and calculate the volumetric strain change induced by the seismic event in a homogeneous, elastic half-space (Okada, 1992; Nostro et al., 1998). The volumetric strain change is computed at different locations (every 2 km) within a radius of 110 km from the epicentral area and from the ground surface to a maximum depth of 10 km (Figure 3.3C). At the well location, the distribution of volumetric strain was computed along intersecting vertical planes, to gain a detailed picture of the spatial distribution of the deformation. Figure 3.3 shows that positive volumetric strain is induced at hypocentral depth while above a depth of about 2 km negative strain is induced, driving the observed pore pressure increase. I choose an average Poisson ratio ν=0.3, typical of sandstone in undrained conditions (Rice and Cleary, 1976), to represent the rock properties of the shallow crust. The resulting volumetric strain change ($\Delta\epsilon_{kk}$) at the surface is shown in Figure 3.3B and ranges from $-6 \cdot 10^6$ (contraction, in blue) to $24 \cdot 10^6$ (expansion, in red). The largest changes occur within a few km from the epicenter. All the wells are located in an area of contraction, with the exception of well BOF9-00, located where strain is positive (expansion). This volumetric strain change is considered as approximately constant within the fluid flow domain (Figure 3.3C). The computed volumetric strain was used to calculate the corresponding isotropic stress change, in the undrained limit, as equation 3.1.

$$\Delta\sigma_{kk} = 3K_u \cdot \Delta\epsilon_{kk} \tag{3.1}$$

$\Delta\sigma_{kk}$ is the trace of the stress tensor change and K_u is the undrained bulk modulus. Seismic tomography and stratigraphic data (Cocco et al., 2001, and references therein) for this region show an important structural discontinuity at a depth of 130 m, where shear wave velocity changes by a factor of 5

(from 400 to 2000 m/s). Based on this evidence, I considered different elastic properties above and below this depth, computing the rigidity as equation 3.2 where V_s is the shear wave velocity and ρ is the rock density (see Table 3.1).

$$G = V_s^2 \rho \tag{3.2}$$

From the expression (3.3), where G is the rigidity and ν_u is the undrained Poisson modulus (Table 3.1), I obtained different values of K_u above and below 130 m depth.

$$K_u = \frac{2}{3} G \frac{1 + \nu_u}{1 - 2\nu_u} \tag{3.3}$$

Table 3.1: Elastic parameters used to calculate the two stress maps, above and below the depth of 130 m. G = rock rigidity; V_s = shear wave velocity; ν_u = undrained Poisson modulus; ρ = rock density. Poisson ratios are taken from Mavko et al. (1998)

Parameter	Shallow layers	Deep layers
G(GPa)	0.4	9.6
$V_s(m/s)$	400	2000
ν_u	0.4	0.37
$\rho(kg/m^3)$	2300	2400

Accordingly isotropic stress changes, unlike volumetric strain changes, can be considered as depth dependent, basically due to rigidity variations with depth. Then, two maps of isotropic stress change were considered above and below the depth of 130 m. To evaluate the groundwater response, these stress changes are translated into pore pressure variations. The linear theory of poroelasticity describes how the stress change is transferred from the solid skeleton to the pore fluid, according to a simple relation (3.4) (Skempton, 1954; Grecksch et al., 1999; Roeloffs, 1996; Roeloffs and Quilty, 1996; Ge and Stover, 2000):

$$\Delta p = -B \frac{\Delta \sigma_{kk}}{3} \tag{3.4}$$

where p is the pore pressure and B is the Skempton's coefficient (I assumed

$B = 1$ to represent sediments of the Po Plain). Equation (3.4) is valid in undrained conditions. In our case, the pressure change caused by the earthquake can be considered instantaneous compared to the time required by the water to flow through the porous rocks, hence the assumption of undrained conditions is justified. Equation (3.4) was applied to compute the perturbation caused by the May 20 earthquake in all the grid blocks of the computational domain below the water table (i.e., water saturated). Figure 3.5 shows the resulting pressure changes that I applied to all the computational grid blocks above -130 m (a), and below such depth (b). The resulting pressure distributions were applied as initial conditions in the porous media flow model described below. The locations of the shallow and deep well considered in the transient evolution are also indicated in Figure 3.5 (black squares).
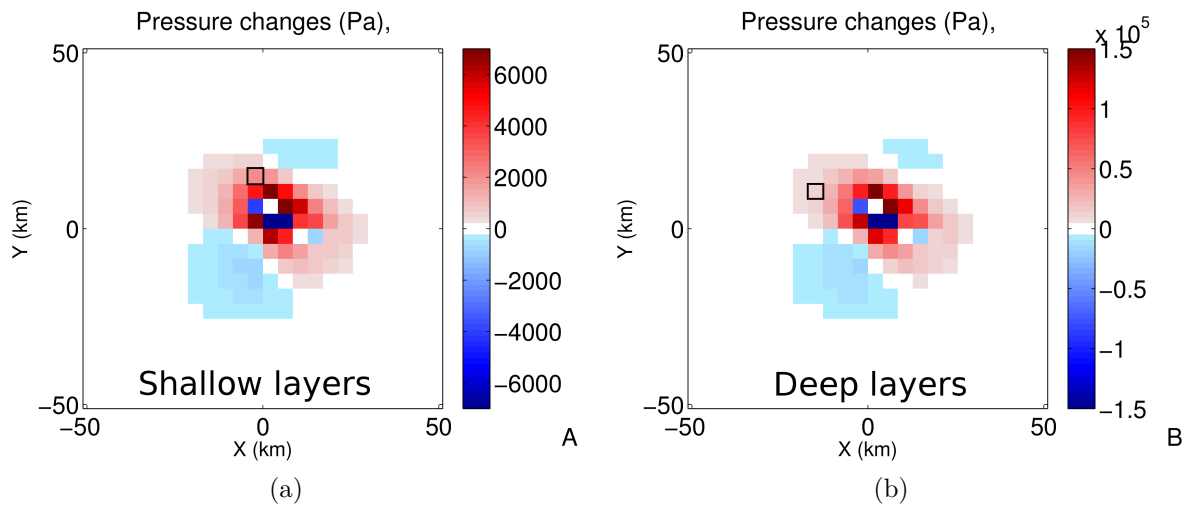

Figure 3.5: Distribution of pore pressure change (Pa) due to the May 20 earthquake along a horizontal section of the computational domain (100x100 km). (a) Values assigned at depth less than 130 m. The same pressure change is applied along the vertical direction for grid blocks of layers 1 and 2. (b) Values assigned at depths greater than 130 m. The same pressure change is applied along the vertical direction for all the grid block of layers 3 and 4. Squares represent the computational grid block elements. Black squares highlight the grid block corresponding to the shallow (a) and deep wells (b). Note the change in color scale.

3.4.2   The aquifer response

The aquifer response to the computed pressure perturbation is studied with the TOUGH2 simulator, which can describe flow of water through saturated and unsaturated porous media (Pruess et al., 2012). The model is based on an integrated finite difference approach with a first-order, fully implicit time discretization. Our application describes the coupled flow of heat, water, and air through a heterogeneous porous matrix, accounting for the interference between gas and liquid phases (through appropriate relative permeabilities and capillary pressure functions). In our application, the flow model does not account for chemical reactions or for deformation of the porous medium. Our study area is represented with a three dimensional computational domain discretized with 41600 elements (20x20x104) for a total length and width of 100 km, and 0.5 km depth. The computational mesh is particularly fine in the vertical dimension, to capture small changes in water level: element thickness ranges from 1 to 80 m, with greater resolution near the surface. To keep the number of grid blocks to a manageable level, the mesh is coarser in the horizontal dimensions, where elements size ranges from 4x4 km, near the fault location, to a maximum area of 12 x 12 km. I performed several grid tests (Appendix B) to ensure that the extreme aspect ratio of the elements does not introduce a significant bias in the estimate of water level change. The stratigraphy of the region is well constrained because of the availability of a large number of data derived from deep and shallow drilling and from geophysical prospecting (Cocco et al., 2001). The shallower portion of the Po Plain is characterized by several superimposed aquifers that are interspersed with impervious units, resulting from the alternating sedimentation of clay and sand (Regione-Emilia-Romagna and ENI-AGIP, 1998; Marcaccio and Martinelli, 2012). To represent this general setting, I implement a general shallow stratigraphy where two aquifers are separated by less permeable layers, that I will consider here as confining units (Figure 3.6). In this stratigraphy, an upper aquifer (1) overlies a low-permeability layer (2). The deep aquifer (3) is confined by two confining units (2 and 4). To represent the hydraulic properties of such a stratigraphic setting I choose reasonable parameter ranges that represent the average response of laterally extensive aquifers and impervious layers. I tested several combinations of porosity and permeability in the four layers I present here a set of results (Table 3.2). All the considered values are within the characteristic range of fine sands and

layered clays that compose the shallow sequence of the Po plain (Priolo et al., 2012; Bordoni et al., 2012). The unsaturated layer is 5 m thick, while below this depth the porous medium is fully water saturated. I apply a geothermal gradient of 40 °C/km and let the model compute the hydrostatic pressure distribution at steady state. The upper and lateral boundaries are open to heat and fluid flow. This condition is implemented in TOUGH2 by imposing fixed conditions to all the elements along the boundaries. The upper boundary is therefore at atmospheric condition (air saturated, 0.1 MPa and 20 °C) and the elements along vertical boundaries are set at the temperature, pressure and water saturation corresponding to their depth in hydrostatic conditions.

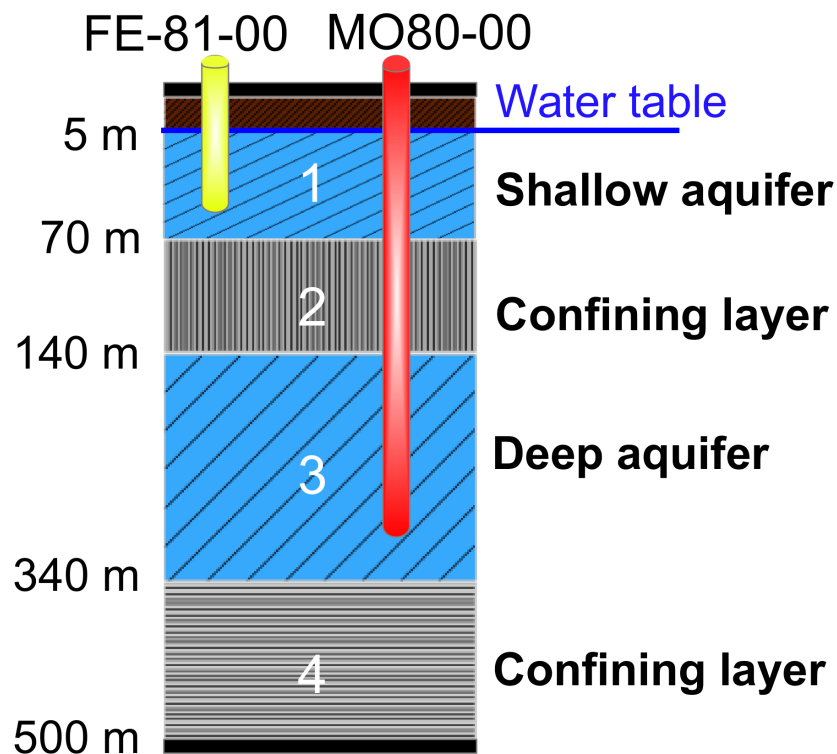Figure 3.6: Layering assigned to the porous media flow model. Layers 1 and 3 represent two aquifers, layers 2 and 4 are two confining layers. The domain is entirely water saturated from the bottom to the elevation of the water table (5 m below the surface). The shallow and deep wells, representing FE-81-00 and MO80-00 water wells, respectively, are shown.

The bottom boundary is closed to heat and fluid flow. This condition cor-

responds to a shallow system that is effectively insulated by the presence of an impervious layer. The presence of such a layer is consistent with the geological setting of the area, characterized by multiple superimposed aquifers associated with alternating layers of sand and clay (Ori, 1993; Amorosi et al., 1996; Regione-Emilia-Romagna and ENI-AGIP, 1998). The observed lack of temperature and/or salinity changes in monitored wells, also confirms the relative insulation of the shallow aquifer with respect to warm saline fluids from greater depths (Marcaccio and Martinelli, 2012). Due to the lack of observational constraints at great depths, the imposition of a very shallow impervious bottom boundary stems from the plausible assumption that permeability steadily decreases with depth; this imposition allows us to use a reasonable number of elements in the computational domain, while keeping high resolution. Furthermore the use of a shallow computational domain is appropriate in our case, as I am interested in the short-term evolution (weeks) of shallow wells. Taking into account the diffusion equation governing pore pressure, the time scales needed to detect effects related to pore pressure changes near the hypocenter (6 km depth) are expected to be much longer than weeks, due to the long distance L ($>$ 6km) and the lower hydraulic diffusivity D expected at increasing depths (the diffusion time scales as L^2/D). To make sure that the imposition of such a shallow boundary does not significantly affect the results, I performed a test with a deeper domain (700 m) that shows no significant differences in the pressure evolution. The seismically-induced pressure changes (Figure 3.5) are then applied at the beginning of each simulation, and the model is run to describe the system evolution during the following 20 days.

3.5 Simulation results

Four permeability structures are considered in detail (Table 3.2). Case 1 assumes a large permeability contrast between the aquifers and the confining layers and a relatively high permeability for the aquifers. Figure 3.7 shows the pressure distribution at different depths (-40 and -300 m, corresponding to the depths of the wells) and at different times (initially and after 1 day). The shallow aquifer is characterized by lower pore pressure perturbations and by a faster evolution than the deep aquifer: after one day of simulation, pore pressure has almost returned to its initial unperturbed value, whereas
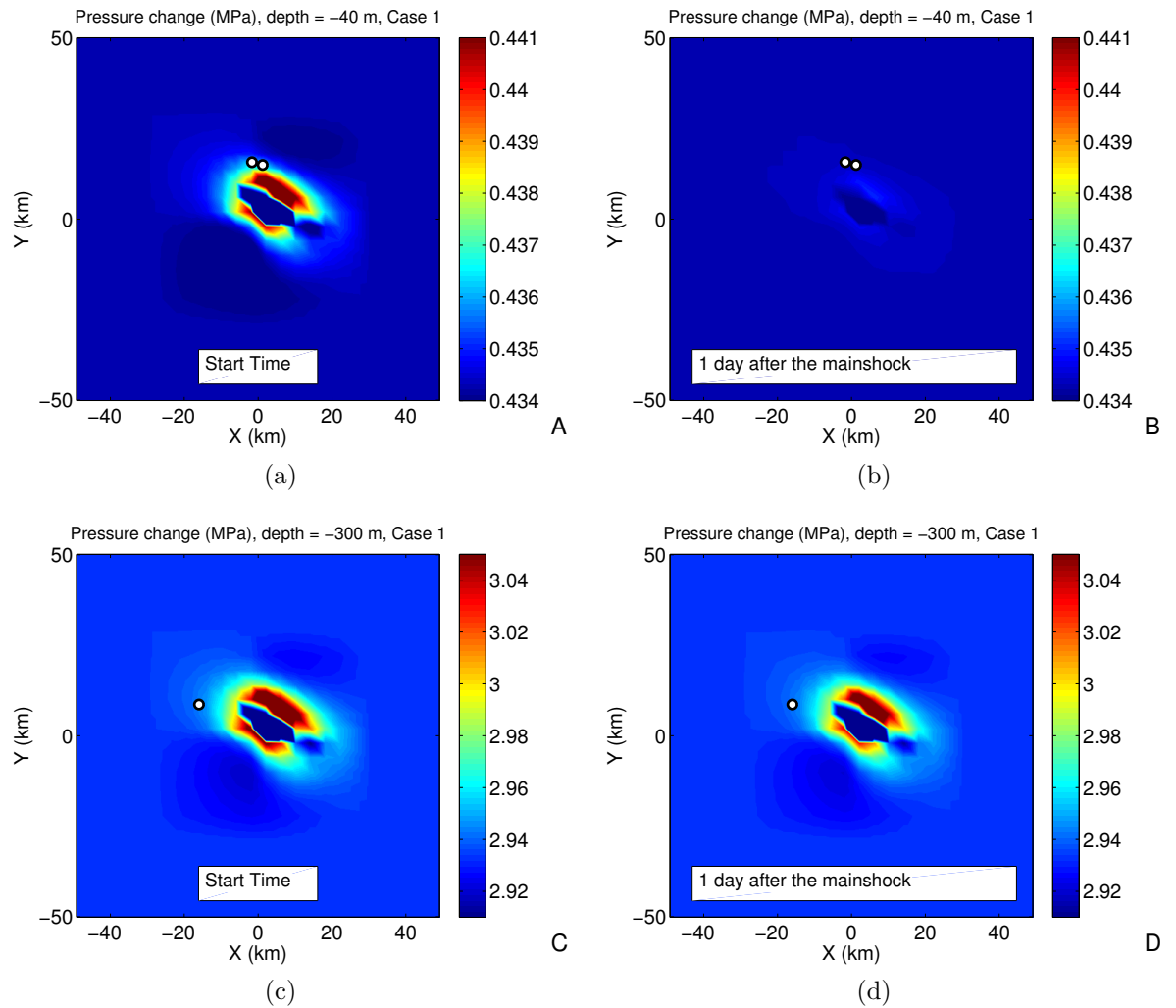
45

(a)

(b)

(c)

(d)

Figure 3.7: Case 1. Simulated pressure distribution (MPa) on a horizontal section, at different depths and times: shallow wells depth (-40 m), at the beginning of the simulation (a) and after 1 day (b). Deep well depth (-400 m), at the beginning of the simulation (c) and after 1 day (d). White dots represent the water wells. Note the change in color scale.

Table 3.2: Rock porosity and permeability values assigned to the layers in the four cases. Permeability is isotropic.

Layer	Porosity	Permeability (m^2)			
	All cases	Case 1	Case 2	Case 3	Case 4
1	0.4	$1.5 \cdot 10^{-13}$	$1.5 \cdot 10^{-13}$	$1.5 \cdot 10^{-14}$	$3.0 \cdot 10^{-14}$
2	0.4	$1.5 \cdot 10^{-15}$	$1.5 \cdot 10^{-14}$	$1.5 \cdot 10^{-16}$	$3.0 \cdot 10^{-15}$
3	0.3	$1.5 \cdot 10^{-13}$	$1.5 \cdot 10^{-13}$	$1.5 \cdot 10^{-14}$	$3.0 \cdot 10^{-13}$
4	0.4	$1.5 \cdot 10^{-15}$	$1.5 \cdot 10^{-14}$	$1.5 \cdot 10^{-16}$	$3.0 \cdot 10^{-15}$

the deep aquifer is still perturbed. The temporal evolution of pore pressure in the deep and shallow wells is shown Figure 3.8, which compares results obtained with different permeability distributions (Table 3.2). In the shallow wells (Figure 3.8A), when the earthquake strikes, the pressure undergoes an instantaneous increase of about 3 kPa from the initial, unperturbed value. The corresponding piezometric head variation (equation 3.5) is of the order of 30 cm, in good agreement with the observations.

$$\Delta h = \Delta p / \rho g \tag{3.5}$$

Subsequent evolution is characterized by a quick pressure drop, followed by a second and lower pressure increment. This second pressure fluctuation reflects the arrival of fluids from the deeper region of the domain that were set into motion by the earthquake, at the beginning of the simulation. The rate and amplitude of this second pressure fluctuation depends on the permeability assigned to both the aquifers and the confining layers. In Case 1 and 3 this pressure rise occurs after about 1 day of simulation, while the strongest and fastest response is obtained in Case 2, where all layers are rather permeable and the second pressure pulse occurs right after the co-seismic one. This is the only simulation where pressure fully recovers its initial, unperturbed value in the simulated 20 days. In all other cases, the pressure in the shallow aquifer remains above its initial value. In Case 3 the water level drop that occurs soon after the earthquake is slower than in Case 1 and Case 2, mainly due to the lower permeability of the shallow aquifer. In this case, the arrival of fluids from the deep aquifer has little influence on the well pressure and occurs after 5 days. The pressure evolutions obtained in Case 4 better resembles the
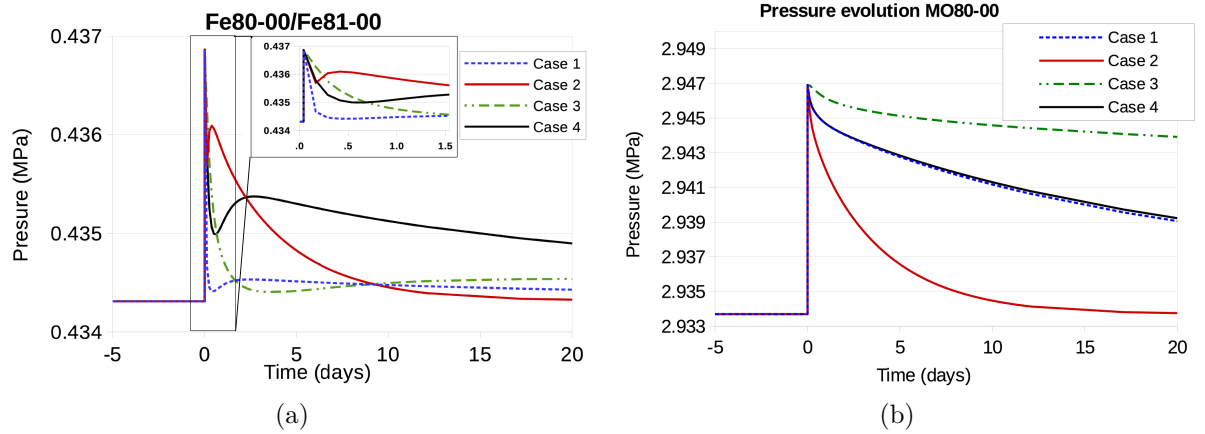
Figure 3.8: Bottom hole pore pressure transient evolution (MPa) for (a) the shallow wells (FE80-00 and FE81-00), and (b) the deep well MO80-00, for the four different permeability distributions given in Table 3.2.

observed well behavior, with a second, minor level rise after the co-seismic peak, followed by a very slow recovery to pre-earthquake values. Pressure evolution in the deep, confined well is characterized by greater changes and by a slower post-seismic evolution (Figure 3.8B). In our calculation, the earthquake causes a pore pressure increase of about 14 kPa. This corresponds to a water level change of 1.4 m, similar to the actual observation (1.6 m). In this case, the impervious bottom boundary prevents outflow of fluids towards deeper layers, and post-seismic pressure evolution is characterized by a monotonic decay, whose rate depends on the permeability structure. As with the shallow wells, the more permeable system (Case 2) is the only one where pressure returns to its initial value within the 20 days of our simulation. In this case, the pressure evolution obtained in Cases 1 and 4 better reflect the rate of water level decay observed in the deep wells. Notwithstanding the applied geothermal gradient (40°C/km), and even though the two aquifers are separated by a rather permeable confining layer, the upward component of fluid flow does not provide a measurable increase of water temperature, as observed.

3.6 Compaction and meteoric recharge

Numerical simulations provide information on pressure evolution that can be easily converted into water level changes, allowing for comparison with observations from deep and shallow wells (Figure 3.9). The observed water level changes are compared with Case 4, which provides the best match with the data. Figure 3.9 also shows results obtained accounting for two different effects that may have affected the observed water level: meteoric recharge and compaction. The May 20 event was followed by two rainy days. The weather monitoring stations in the area measured 30 to 45 mm of rain accumulated from May 20 to May 22 (Table 3.3. Informations avaiable from: http://www.arpa.emr.it/). The effects of rain may appear with a large time delay in deep aquifers (Roeloffs, 1998), but groundwater bodies at shallow depths are quickly influenced by meteoric recharge (Marcaccio and Martinelli, 2012). The effect of rain was incorporated into our simulations by placing

Table 3.3: Cumulative rainfall over three days, measured by weather stations in the area.

Station	mm
Opera Po	30.4
Malborghetto di Boara	41.2
Finale Emilia	45.0

water sources along the top of the domain. The water sources inject water at ambient temperature (20 °C) and at constant rate of $2.6 \cdot 10^{-4} \ kg/m^2 s$, from May 20 (12:00 a.m.) to May 22 (12:00 a.m.), corresponding to about 45 mm of cumulative rainfall. Meteoric recharge makes the second peak sharper and higher, but does not affect the rate of water level decline in the long term (Figure 3.9A). The second effect I introduced is related to co-seismic changes of hydraulic properties. Seismic shaking can affect the size, distribution and connectivity of pores and thus change both porosity and permeability (Wang et al., 2001; Manga and Wang, 2007; Convertito et al., 2013). In an alluvial plain, like the Po Plain, ground shaking may cause the re-arrangement of solid grains (especially where unconsolidated sediments are present under low confining pressures), favoring compaction and associated porosity and permeability decreases. In our case, the shallow layer is made of alternating

49

silt and clay, and is expected to be highly susceptible to compaction. I assume that earthquake shaking instantaneously caused a permanent reduction of the porosity in the shallow aquifer only, from the initial, unperturbed value ϕ_0, to a new, lower value ϕ_1 (Equation 3.6).

$$\phi_1 = \phi_0 - \Delta\phi \tag{3.6}$$

I tested different values of $\Delta\Phi$ and here present results obtained with $\Delta\phi = 2 \cdot 10^{-3}$. The porosity loss causes an increase (Δh_1) of the initial water level h_0 corresponding to:

$$\Delta h_1 = h_0 \frac{\Delta\phi}{\phi_1} \tag{3.7}$$

A corresponding pressure change $\Delta p = \rho g \Delta h_1$ is assigned to all computational cells in the shallow aquifer. For a porosity loss of $2 \cdot 10^{-3}$, the resulting water level change is of the order of 30 cm and corresponds to a pore pressure increment of about 3 kPa. Compaction also affects permeability and the expected change is computed as a function of the porosity changes, according to the equation 3.8 (David et al., 1994; Chin et al., 2001; Rinaldi et al., 2014), where k_1 is the new permeability after compaction, k_0 is the initial permeability (Table 3.2, Case 4), and α is the so-called "*porosity sensitivity*", whose value ranges from 1.86 to 25.4 in sandstones (David et al., 1994; Yale, 1984).

$$k_1 = k_0 \left(\frac{\phi_1}{\phi_0} \right)^\alpha \tag{3.8}$$

Again I performed several tests and the best results were achieved using $\alpha = 15$. The simulations that include meteoric recharge and compaction better capture some details of the shallow wells evolution: accounting for compaction doubles the initial water level rise, leading to a maximum value of 0.59 m. Once the pressure drops, both simulations, with and without compaction, exhibit similar behavior in the long-term (Figure 3.9A). Introduction of meteoric recharge results in a second pressure peak that nicely matches the water level rise observed 2 days after the seismic events. Long term evolution is not affected by the rainy days. Rain and compaction do not affect the water level in the deep well (Figure 3.9B). The simulated rain event is too small to affect the deep aquifer, which is effectively confined by layer 2. This
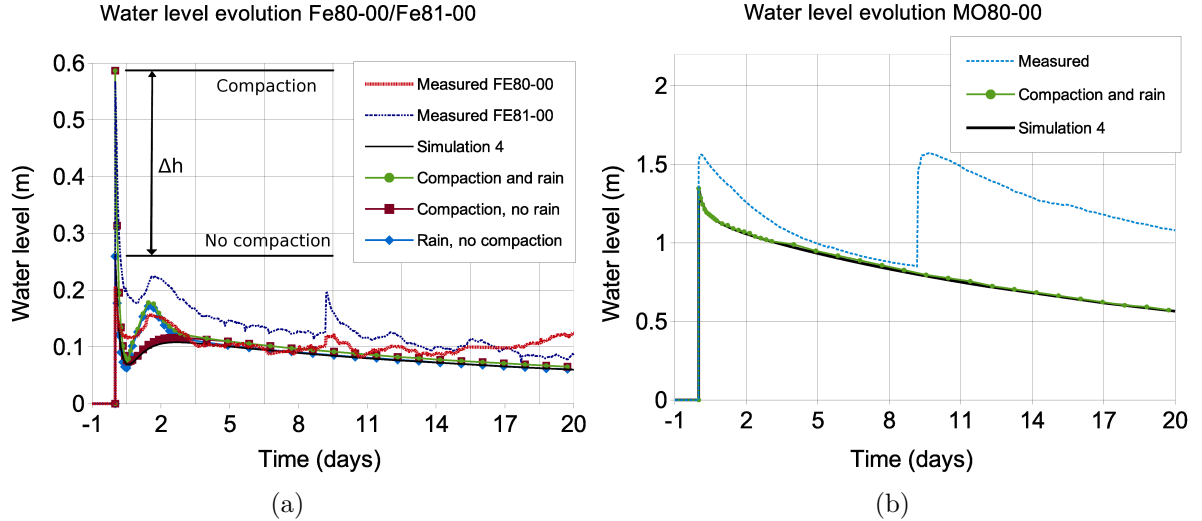
Figure 3.9: Water level changes (m) for (a) the shallow wells (FE80-00 and FE81-00), and (b) the deep well (MO80-00) for case 4. Simulations results obtained with and without compaction and rain are compared with observed evolution.

is consistent with available data, suggesting that the recharge area of the deep aquifer is located more than 30 km south of the study area, on the edge of the Apennines chain (Regione-Emilia-Romagna and ENI-AGIP, 1998).

3.7 Discussion and conclusions

The May 20, 2012 Emilia earthquake caused an increase in water level recorded both in deep and shallow water wells. The deep and shallow wells display remarkable differences both in the magnitude of the observed changes and in the rate of recovery. Our approach combines a description of the seismic source, in terms of fault geometry and coseismic slip distribution, based on the inversion of GPS and InSAR co-seismic displacements, with a specific porous-media flow model that enables us to account for the complexities of a heterogeneous stratigraphy. Our results show that the effects of the earthquake can be suitably represented in the fluid flow model as an instantaneous variation of pore pressure, whose magnitude and location depend on the slip distribution along the fault. The pore pressure change experienced in each

51

well depends on well depth and position with respect to the epicenter. The properties of the hydrogeologic units control the post-seismic dissipation of this pressure pulse: the shallow, unconfined aquifer is characterized by a very fast evolution that dissipates most of the co-seismic pressure pulse within a few days, while the deep, confined aquifer requires a longer recovery time. Our simulations capture the different orders of magnitude that characterizes the response of deep and shallow wells to the same seismic event. The results presented above suggest that the observed water level changes depend not only on the magnitude and location of the seismic event, but also on the presence and properties of heterogeneous materials. The observed evolution is well represented assuming a very permeable $(1.5 \cdot 10^{-13} m^2)$ aquifer at depth, well-confined by two low-permeability $(1.5 \cdot 10^{-15} m^2)$ layers. At the top of the sequence I simulate the presence of a less permeable $(3 \cdot 10^{-14} m^2)$ unsaturated layer. The absence of full recovery of previous water levels in the shallow wells (FE80-00 and FE81-00) is well explained by pressure evolution in a groundwater system with a deep aquifer confined between low permeability layers. Co-seismic compaction and two rainy days explain the details of the water level changes. Different degrees of compaction could explain the different water levels recorded by the two wells that are very close in space. Episodes of liquefaction and spontaneous fluid emissions have been reported in the aftermath of the earthquake, and suggest that significant changes in the rock properties (including compaction) occurred at very shallow depth (Emergeo-Working-Group, 2012, http://emergeo.ingv.it). The occurrence of shallow compaction is also consistent with the observed response of these wells to the second earthquake, on May 29 (Figure 3.2A,B). Although I did not simulate this second event, I highlight the smaller water-level changes associated with this event and the slower (and complete) recovery to pre-earthquake levels. If the lower amplitude of the water level rise is due to a greater distance from the epicenter, the slower recovery suggests a lower aquifer permeability, consistent with compaction. The deep well (MO80-00) is characterized by simpler evolution that is not affected by rain or shallow compaction. Its response to the May 29 event equals the water level rise observed on May 20 (although the epicenter of the second event is closer), and is followed by a slightly slower recovery. Numerical simulations provide a good description of the overall behavior, but fail to reproduce details of the co-seismic water level change. This lack of correspondence may be due to a poor choice of local rock properties (both elastic and hydraulic), in a geological

setting characterized by strong lateral heterogeneites. Short-term pressure changes inside the well are very sensitive to the local ground properties. On the contrary, the long-term evolution depends on larger spatial scales, and a general description with average material properties is better suited to obtain a good match with data. Future development should extend the study to hypocentral depths to account for the fluid migration within seismogenic areas and investigate the role of fluid flow in the evolution of the seismic sequence.

GROUND HEATING IN TERRE CALDE DI MEDOLLA (ITALY)

Contents

The results shown in this chapter are published in Nespoli et al. (2015c).

The area known as Terre Calde (literally "hot lands") in the plain of the Po River (Italy) is well known for unusual ground temperatures, and up to now, the cause of the heating was never fully investigated. These higher-than-average temperatures are commonly associated with diffuse methane seepage. A detailed study of shallow stratigraphy, temperature profile, and associated gas concentrations and flow rates recently suggested that the observed anomaly could be related to the exothermic oxidation of biogenic methane, possibly
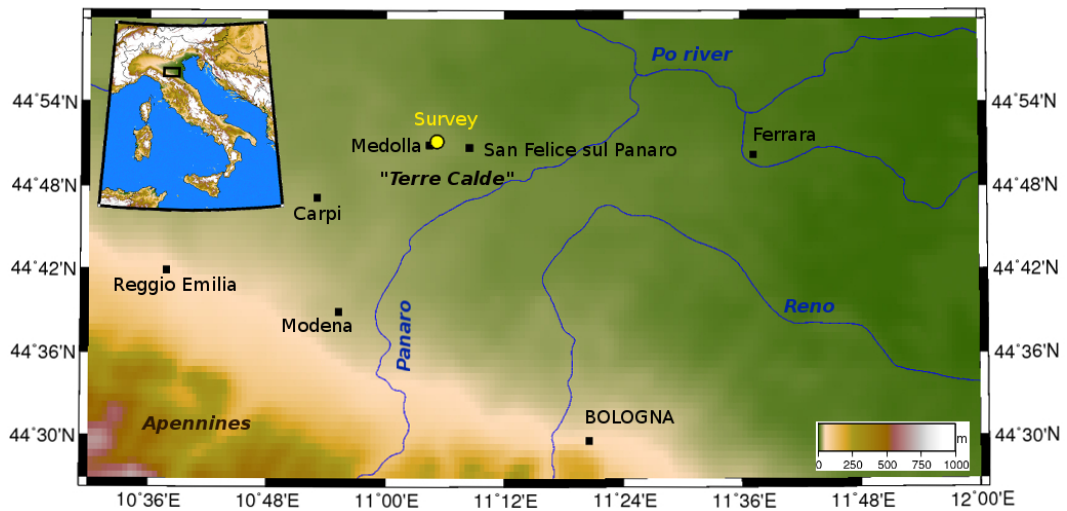
Figure 4.1: Map of the area around the "Terre Calde-hot lands." Field survey (yellow circle) was performed near Medolla (Modena). The figure is created with GMT software (Wessel and Smith, 1998).

rising from a shallow peat layer. In this work, the porous media flow simulator, TOUGH2, was applied to verify a conceptual model of this phenomenon devised on the base of available data. The model describes a layered system, with a shallow unsaturated zone, where methane is continuously supplied along the base and heat is generated as a result of its oxidation above the water table. To mimic the oxidation process, heat sources are placed within the layer where oxidation takes place, and the heat generation is computed as a function of methane flux entering the layer. Numerical simulations were carried out imposing different methane flow rates along the base of the model. The simulations also explored the efficiency of methane oxidation, considering different heat generation rates and accounting for seasonal effects. The good match between observed and simulated temperature profiles suggests that the main features of the process are captured by the model and that the conceptual model is plausible from a physical point of view.

4.1   The Terre Calde area

The name Terre Calde (literally "hot lands") indicates an area in the plain of the Po River (near the town of Modena, Italy; Figure 4.1), where the

ground temperature significantly exceeds the local average values, sometimes reaching up to 50 °C. The very existence of the toponym testifies for a long-known feature of these lands, whose most evident manifestation is the lack of snow accumulation on the ground during winter (Floodgate and Judd, 1992). Available measurements suggest that these temperature anomalies are often accompanied by a diffuse seepage of methane. Seismic reflection profiles in this area highlight the widespread presence of rising gas, which is commonly interpreted as biogenic methane generated by bacterial degradation of organic matter at depth (Bonori et al., 2000; Cremonini, 2010). The presence of water wells may act as a drainage system for the rising gas, which eventually produces a visible bubbling of well water. The occurrence of such a phenomenon is commonly reported in the aftermath of earthquakes, possibly because of the greater public awareness that follows seismic events. In 1996, several cases of bubbling wells were reported near the town of San Felice sul Panaro, after the Reggio Emilia earthquake (M 5.4) (Bonori et al., 2000). More recently, interest in these phenomena was renewed after the seismic sequence that struck the region in 2012, when the largest event reached magnitude 5.9. While no temperature changes were detected by the regional network that probes well waters every hour (Marcaccio and Martinelli, 2012), several cases of heated and bubbling waters were reported during and after the sequence. Although many cases remained anecdotal, the anomalous temperatures reported near Medolla were verified by a survey of the Camposanto well, where temperature up to 50 °C were measured shortly after the 2012 earthquakes. The observation of anomalous water temperatures within the same time window of seismic activity seems to reinforce a common assumption that the two phenomena are somehow related. Seismicity may facilitate the migration of warm gases toward the surface by increasing the pore pressure and/or by enhancing permeability, and this, in theory, could explain the anomalous heating. Unfortunately, a comprehensive account of all temperature anomalies, with their exact timing and location, is not available, and the existence of a causal link between seismicity, gas ascent, and anomalous ground heating was never proven. Capaccioni et al. (2015) propose an alternative mechanism to explain the hot lands near Medolla. On the basis of geochemical data, the authors suggest that the observed surface thermal anomalies are not linked with local ascents of hot fluids from depth, but could rather be the result of heat production at very shallow depths, thanks to oxidative conditions and bacterial activity, promoting the

exothermic oxidation of methane. The methane loss within the soil due to oxidation is a well established phenomenon (Romanak et al., 2012), but it is not clear whether the heat generated in this way is enough to produce the observed temperature anomalies. To test this hypothesis, I simulate the generation and propagation of heat within a shallow porous medium. The simulations describe a layered system, with a 2 m thick unsaturated zone at the top and water saturated at depth. The system is fed by a constant flux of methane along the base, to mimic the natural gas ascent. Heat generation takes place within a thin layer (the oxidation zone) in the unsaturated region. Although I do not simulate the actual oxidation process, the heat generation rate is computed as a function of methane flux entering the oxidation zone. Numerical simulations were carried out to explore the effects of different methane fluxes at the bottom boundary, the role of the efficiency of methane oxidation and of seasonal fluctuation of atmospheric temperature. A comparison between simulated and observed temperature distribution suggests that the model captures the main features of the process and that shallow methane oxidation is a viable mechanism to explain the origin of the hot lands near Medolla.

4.2   Field data and conceptual model

The data used in this work were collected during the field survey described in (Capaccioni et al., 2015).

Data on temperature, gas composition,and flow rate were obtained during manual drilling down to a depth of 4.5 m. To perform the measurements, a plastic pipe (4.2 cm in diameter) was introduced into the drill hole to perform measurements as drilling reached different sampling depths. The temperature map at 0.3 m is shown in Figure 4.2. The measurements were all carried out at the surface (upper end of the pipe) after adequate purging of the sampling device. Data were collected during drilling every 0.1 m, from the surface to a depth of 1 m, then every 0.5 m in the interval of 1–2.5 m. Further details on the sampling procedure are provided in Capaccioni et al. (2015). Drilling also allowed to reconstruct the shallow stratigraphy (Figure 4.3), which consists of alternating clay, silt, and fine sand. The distribution of temperature and gas composition with depth are described in Figure 4.4.
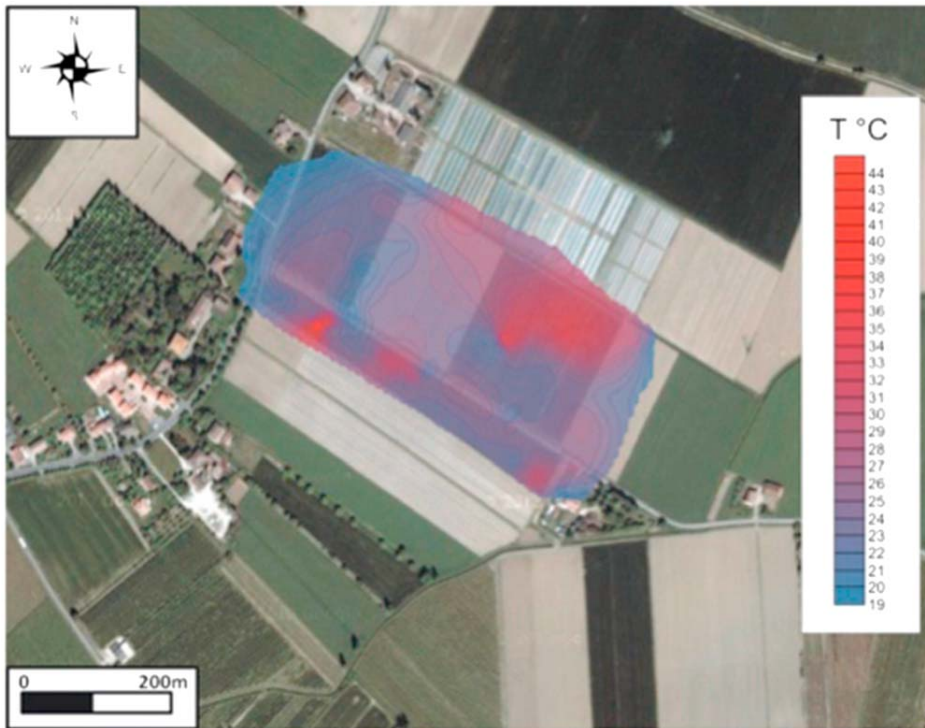
Figure 4.2: Map of the temperatures measured in the area at 0.3 m of depth. The figure is taken from (Capaccioni et al., 2015).
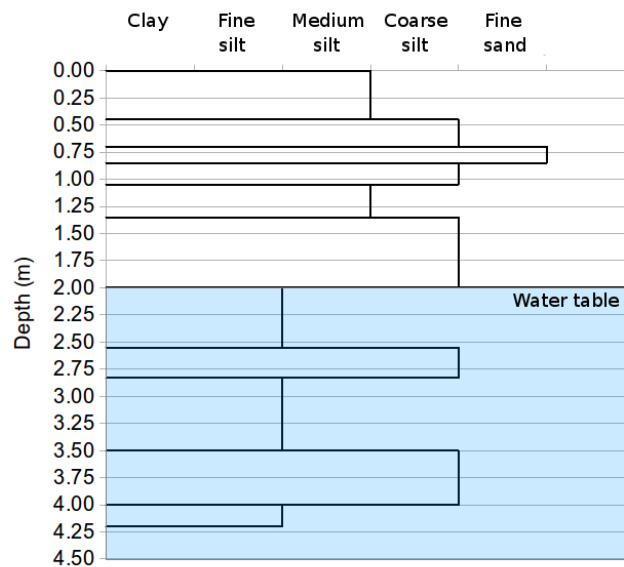

Figure 4.3: Stratigraphy obtained by visual inspection of granulometry. The water table was at a depth of about 2 m.
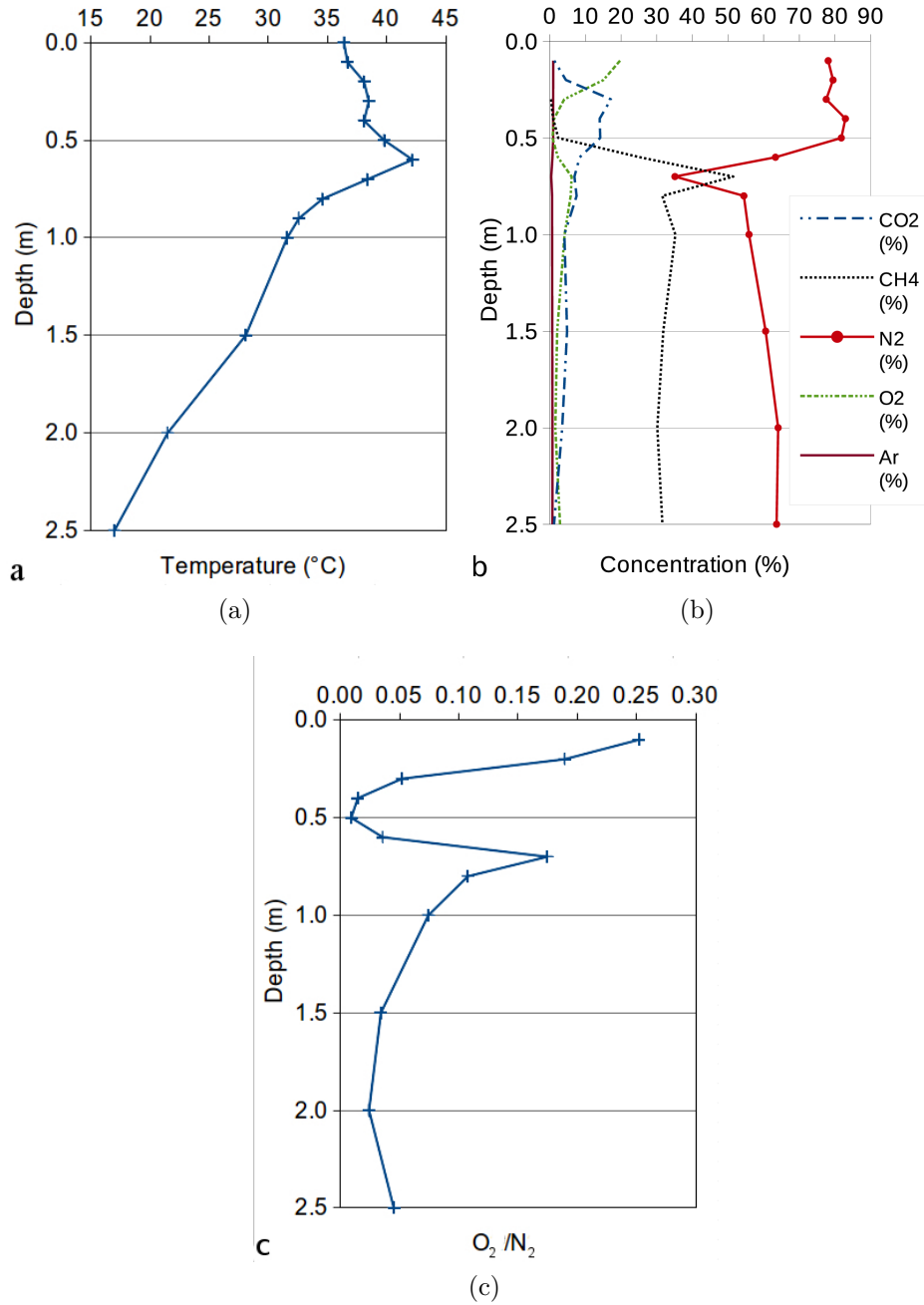
59

(a)

(b)

(c)

Figure 4.4: (a) Temperature profile. (b) Concentration (vol %) of five different gas species along profile (shallowest 2.5 m) obtained with thermal conductivity detector. (c) O_2/N_2 ratio along profile..

These data show shallow temperatures well above a normal geothermal gradient, with a maximum value of 42.2°C at 0.6 m depth, and the soil temperature at the surface (36.4°C) that exceeds the atmospheric value (32°C). The warmest zone (T>40°C) corresponds to the coarse, permeable silt layer (0.5–0.75 m; Figure 4.3) and has a peculiar gas composition (Figures 4.4b and 4.4c), characterized by the minimum concentration of O_2 and CH_4 (0.75 and 0.33 vol %, respectively) and the maximum of CO_2 content (14%). The O_2/N_2 ratio reaches here a minimum value (0.01), well below the typical value of lower atmosphere (0.264) (Rannaud et al., 2008), suggesting oxygen consumption. The methane flux was measured at the top of the sampling device. The maximum recorded value during the survey is $2 \cdot 10^{-6} kg/(m^2 s)$, while the measured CH_4 fluxes in the whole Terre Calde di Medolla (TCM) area ($\approx 2.6 \cdot 10^5 m^2$) on 2013 (see (Capaccioni et al., 2015)) range from 0 to $2.8 \cdot 10^{-5} kg/(m^2 s)$, with a mean measured CH_4 flux of $4.3 \cdot 10^{-7} kg/(m^2 s)$. According to Capaccioni et al. (2015), this combination of chemical parameters together with the measured carbon isotopic compositions of CO_2 and CH_4 are reasonably related to the bacterial oxidation of methane, in which O_2 and CH_4 are converted into CO_2 and H_2O. The presence of methanotrophic bacteria was detected by Fedi (personal communication). A similar conclusion was drawn by Dunfield et al. (2007), who report a survey carried out in Tikitere (New Zealand), a geothermal area where diffuse gas emissions are rich in CH_4. They found that methane concentration reaches a minimum near the surface (10–20cm depth) and ascribed the loss of CH_4 to oxidative consumption due to methanotrophic bacteria. Figure 4.5 shows the resulting conceptual model that I have assumed to describe Terre Calde. The generation of methane can occur mainly in two different ways: thermogenic and biogenic (Floodgate and Judd, 1992). The thermogenic production of methane consists of a thermal decomposition of organic matter in sediments, or thermal-induced reduction of larger organic molecule into lighter hydrocarbons and therefore requires relatively high temperatures, commonly found in geothermal areas or at depths largely greater than 5000 m. The biogenic production of methane can occur in a few meters of sediment by bacterial degradation of organic matter. Unlike thermogenesis, this process is characterized by heat production and not consumption. I can trace the origin of methane by measuring the ratio (R) between the two stable carbon isotopes ^{12}C (most abundant) and ^{13}C, in relation to the international standard ratio (Rs) of Vienna Peedee belemnite (VPDB), which defines $\delta^{13}C = (R/Rs - 1)1000$. Isotopic composition between

-110 ‰ and -50 ‰ are closely related to methane of biogenic origin, while thermogenic methane is generally richer in ^{13}C and the PDB ranges from -50 ‰ to -20 ‰ (Whiticar, 1999; Paull et al., 2000). According to Capaccioni et al. (2015), the measured values range between -62.5 ‰ and -72.3 ‰ VPDB, indicating that methane is probably due to bacterial activity. In this context, the diffuse CO_2 seep is mainly the product of CH_4 oxidation at very shallow levels. Significant levels of peat are present in the Po Valley at shallow depths (50 m) (Bonori et al., 2000); therefore, methane production could occur at these depths. Pressure gradients then drive the gas toward the surface, through aerated layers where oxidation can take place according to the reaction:

$$CH_4 + 2O_2 = CO_2 + 2H_2O \tag{4.1}$$
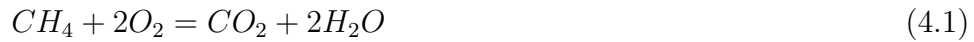
Oxidation takes place preferably in an aerobic environment (Mer and Pierre, 2001), and it is highly exothermic, producing about 800 kJ/mol(CH_4) (Ioannides and Verykios, 1997). The biomass of methanotrophic bacteria depends on the availability of both CH_4 and O_2 and controls the amount of gas that is oxidized (Sundh et al., 1995; Hanson and Hanson, 1996). According to the prevailing local conditions, some fraction of methane may escape oxidation and eventually reach the surface (Figure 4.5). The strong depletion of ^{13}C in CO_2 (δ ^{13}C down to -65 ‰) is consistent with a $^{13}C/^{12}C$ kinetic fractionation due to a partial CH_4 conversion. According to this conceptual model, the shallow, unsaturated layer where the oxidation takes place is the source of the observed ground heating.

4.3 Numerical Modeling

To verify whether the proposed heating mechanism is consistent with the observed temperature profile, we performed some numerical simulations based on this conceptual model. I used the TOUGH2 geothermal simulator (Pruess et al., 1999), which describes the coupled flow of heat and fluids through heterogeneous porous media and is based on a multiphase version of Darcy's law. Heat is transferred by both convection and conduction through the porous matrix. Given the moderate temperatures involved (<50 °C), I neglect the effects of evaporation. The code can handle the simultaneous presence
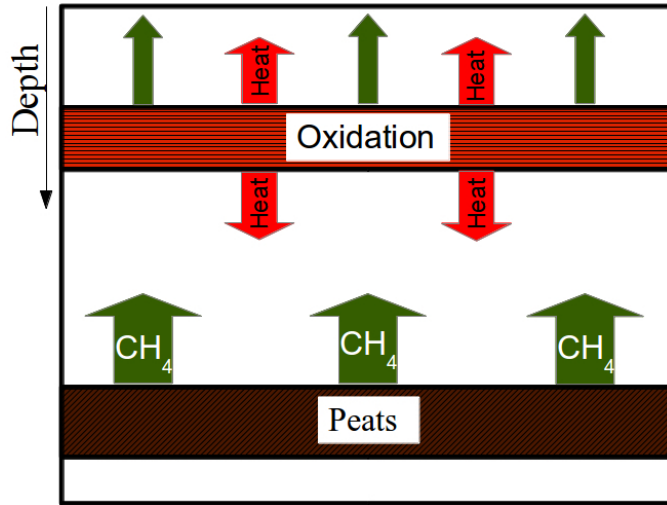
Figure 4.5: Conceptual model (not to scale) illustrating the production and oxidation of CH_4. The arrows represent methane (green) and heat (red).

of different fluid components (water and incondensable gases), in different phases (gas and liquid), with explicit description of gas dissolution in the liquid phase. Phase interference is accounted for by specific relative permeability and capillary pressure functions. Our simulations were performed with the EOS7C module that features the presence of water, with CH_4 and N_2 as gas components and include binary diffusion in the gas phase (Oldenburg et al., 2004). Although we cannot represent all the gaseous species that are present in the soil (CO_2, Ar, and O_2 are not simulated), our purpose is to check our conceptual model from a physical point of view, neglecting those gases whose presence does not affect the energy balance of the model, while representing the thermal and hydraulic discontinuities. I generated a radial 2-D axisymmetric mesh 25 m wide and 20 m deep subdivided into 1520 elements with radial size ranging from 0.1 m to 5 m. The element thickness varies from 0.01 m to 0.4 m for a total of 80 layers. The simulated porous medium is heterogeneous, with the shallow stratigraphy (down to a depth of 4.5 m) that corresponds to the layering retrieved during drilling (Figure 4.3). At greater depths, I considered a single rock type (fine silt) that extends to the bottom of the domain (Figure 4.6).

The thermal and hydraulic properties assigned to the different soil types are reported in Table 4.1. The domain is initially set at ambient temperature
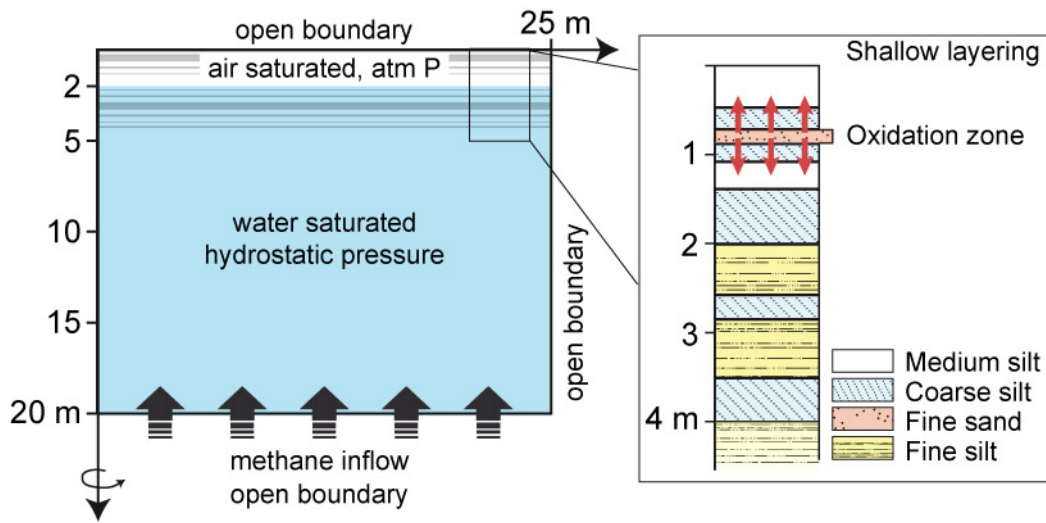
Figure 4.6: The 2-D axisymmetric computational domain. The left boundary is a symmetry axis. The domain is water saturated (blue shade) from the bottom to a depth of 2 m. The observed stratigraphy was included to a depth of 4.2 m (inset). At greater depths, I have assumed uniform properties corresponding to the fine silt.

(13°C). The upper portion of the domain, down to a depth of 2 m, is saturated by nitrogen at atmospheric pressure. In this zone, liquid saturation (i.e., the volumetric fraction of pore space occupied by liquid) is below 0.2 (residual saturation). At greater depths, the pores are water saturated and at hydrostatic pressure (Figure 4.7a). Unless otherwise specified, these conditions are held constant along the boundaries, which are open to heat and fluid flow. To simulate the ascent of methane, generated at greater depths, methane sources are placed along the bottom boundary (Figure 4.7b), discharging methane at the constant flow rate of $1 \cdot 10^{-7} \ kg/(m^2 s)$.

This arbitrary value is 1 order of magnitude lower than the maximum observed methane flux and was chosen to obtain a steady initial condition for our simulation, while ensuring numerical stability. The rising methane dissolves into the aquifer: the mass fraction of methane in the liquid phase is maximum near the lower boundary ($8 \cdot 10^{-5}$) and progressively declines toward the surface, where it reaches the minimum value of $3 \cdot 10^{-5}$ (Figure 4.7b). Some fraction of methane exsolves in the upper portion of the aquifer, where the maximum liquid saturation is approximately 0.9, and tends to concentrate in the low-permeability layers of fine silt, where the liquid saturation drops to
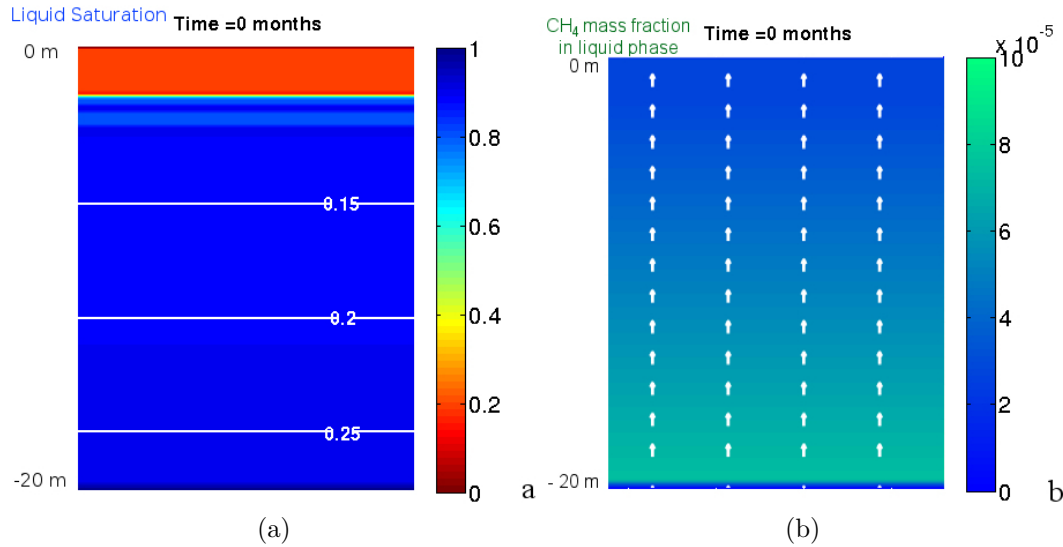
Figure 4.7: Initial conditions for numerical simulations. (a) Liquid saturation (color) and pressure (MPa, contours). (b) Dissolved methane (CH_4 mass fraction in liquid phase, color) and methane flow (arrows), ranging from 0 to $0.1 \cdot 10^{-6}$ $kg/(m^2 s)$.

0.8 (Figure 4.7a). At steady state, the rising methane displaces almost all of the nitrogen from the unsaturated layer, even if gas diffusion is included in the simulation (not shown). This does not occur in the real system, where significant fractions of air are always present in the shallow soil. This implies that I am not capturing all the complexities of gas flow in the unsaturated zone and of the interaction with the residual water. I am focusing on a heat generation process that is driven by methane flow rate, and the values that I obtain along the surface are generally lower than the observed maximum flux and always within the range of observed values. Our results should therefore provide a reasonable estimate of the heat flow that results from the oxidation reaction, even if the unsaturated zone is fully saturated by methane. The conditions shown in Figure 4.7 are taken as initial conditions for the following simulations.

4.4   The Simulated Methane Cycle

Starting from the steady state described above, I performed four simulations lasting 2 years with output every month. Heat sources representing the effect of methane oxidation are placed in the computational cells within the fine sand layer, at depths between 0.6 and 0.7 m, where the highest temperature was measured (Figure 4.6). The bacterial activity could spread over a wider depth range, and the thickness and depth of the oxidation zone could change through time. In our case, however, the temperature profile indicates that most of the heat is produced in a well-confined area, as in other cases reported in the literature (Whiticar and Faber, 1986; Whiticar, 1999; Dunfield et al., 2007).

Table 4.1: Rock Properties for the Four Materials Considered in Our Simulations. Heat generation takes place within the fine sand layer. All layers have the same porosity (0.1) and specific heat (1000 J/(kg K)).

Material	Density	Permeability ()	Wet Heat Conductivity
/	$(kg/m^3$)	m^2	$(W/(mK))$
Medium silt	2300	$5 \cdot 10^{-15}$	2
Coarse silt	2300	$1 \cdot 10^{-14}$	1
Fine sand	2200	$5 \cdot 10^{-14}$	0.5
Fine silt	2300	$5 \cdot 10^{-15}$	0.5

For each source, the heat generation rate is computed dynamically every month (simulation time t_n) as a function of the methane flux that enters the cell in the previous month, according to the relation

$$H(t_n) = \Phi CH_4(t_n - 1) \cdot Ox \cdot S(t_n) \tag{4.2}$$

where H is the heat generation rate $(J/(m^2 s))$, ΦCH_4 is the methane flux in $kg/(s \cdot m^2)$, and Ox (J/kg) is the heat generated by the oxidation of 1 kg of methane (corresponding to $5 \cdot 10^7$ J/kg or 800 kJ/mol); the coefficient $S(t_n)$ reflects the efficiency of the oxidation process and it ranges from 0 (no

oxidation) to 1, when all the methane is completely oxidized. According to (Whalen et al., 1990) and references therein, the optimum temperature for methanotrophic bacteria in different regions worldwide ranges from 30 to 37°C. In our study area, atmospheric temperatures exceed 30°C in summer and easily drop below zero during the winter, so the bacterial activity is expected to be enhanced during the summer times with respect to the colder periods of the year. To explore seasonal effects that may arise as the methane oxidation rate changes with temperature, the value of $S(t_n)$ may follow a periodic behavior (period = 1 year), with a minimum in winter and a maximum in summer, according to the following relationship:

$$S(t_n) = R_s + \frac{R_s - R_w}{2} \left[cos \left(2\pi \frac{n-1}{12} \right) - 1 \right]_{n=1,2,..,24} \tag{4.3}$$

Rs and Rw represent the ratios of oxidized methane with respect to total methane coming into the cell during the hottest month in summer and the coldest one in winter and vary from 0 to 1. Because of the small size of the system, atmospheric temperature fluctuations can affect the heat balance of the model. To account for seasonal effects, I imposed a transient temperature along the upper boundary of the domain. The temperature is updated every month according to the following expression:

$$T_{atm}(t_n) = T_s + \frac{T_s - T_w}{2} \left[cos \left(2\pi \frac{n-1}{12} \right) - 1 \right]_{n=1,2,..,24} \tag{4.4}$$

where Ts is the maximum temperature reached during summer time (36 °C) while Tw is the maximum temperature reached during winter (13 °C).

Four simulations were performed considering different values of methane basal inflow along the bottom and different efficiencies of methane oxidation during summer and winter times (Table 4.2). Simulations 1 and 2 are run with a constant bacterial activity and explore the role of basal methane flux. In simulation 1, the methane flux coming from the lower boundary is $0.4 \cdot 10^{-6}$ $kg/(m^2 s)$, i.e., 20 % of the maximum flux measured at the surface (compatible

Table 4.2: Simulation Parameters. ΦCH_4 = Methane flux at the base of the domain; S(tn) = Oxidation efficiency; Rw and Rs = Fraction of oxidized methane during winter and summer, respectively; and CH_4 Sink Refers to the Placement of a Methane Sinks in the Oxidation Level

Simulation	ΦCH_4 $(kg/(m^2 s))$	S(tn)	Rw	Rs	CH_4 Sink
1	$4 \cdot 10^{-7}$	1	1	1	no
2	$8 \cdot 10^{-7}$	1	1	1	no
3	$4 \cdot 10^{-7}$	Periodic	0	1	no
4	$4 \cdot 10^{-7}$	Periodic	0	1	yes

with the average measured CH_4 flow in the TCM area, $0.43 \cdot 10^{-6}$ $kg/(m^2 s)$), while in simulation 2, the basal methane flux ($0.8 \cdot 10^{-6}$ $kg/(m^2 s)$) corresponds to 40 % of the observed maximum.

The effect of the different methane flow rates on heat generation is shown in Figure 4.8a. The generation rate in simulation 2 is almost double than the rate computed for simulation 1. In both cases, the heat generation rate shows seasonal fluctuations, which are more pronounced in simulation 2 that ranges from 39 $J/(m^2 s)$ in the winter period up to 43 $J/(m^2 s)$ in summer. In simulation 1, the seasonal variations are smaller and the heat generation rate ranges from 20 to 21 $J/(m^2 s)$. In these simulations, the oxidation efficiency does not change through time; therefore, these fluctuations are entirely due to seasonal temperature changes (Figure 4.7b), which cause small variation in methane flux near the surface. Simulations 3 and 4 are both run with the same methane basal flux of simulation 1, but bacterial activity in these cases changes through time (Figure 4.8b), influencing the heat generation rate that stops during the winter (no oxidation) and reaches 21 $J/(m^2 s)$ during summer (Figure 4.8a). Simulation 4 also accounts for the removal of methane caused by the oxidation reaction, allowing for a comparison between simulated and observed methane fluxes. Simulating this process, I do not claim to accurately represent the stoichiometry of the substances involved in the oxidation, but I want to understand how the partial transformation of CH_4 might affect the model and whether it has detectable effects on the surface. The methane loss is simulated by placing methane sinks right above the heat sources. Gas removal rate ΨCH_4 $(kg/m^2 s)$ at a given month (t_n) is proportional to the
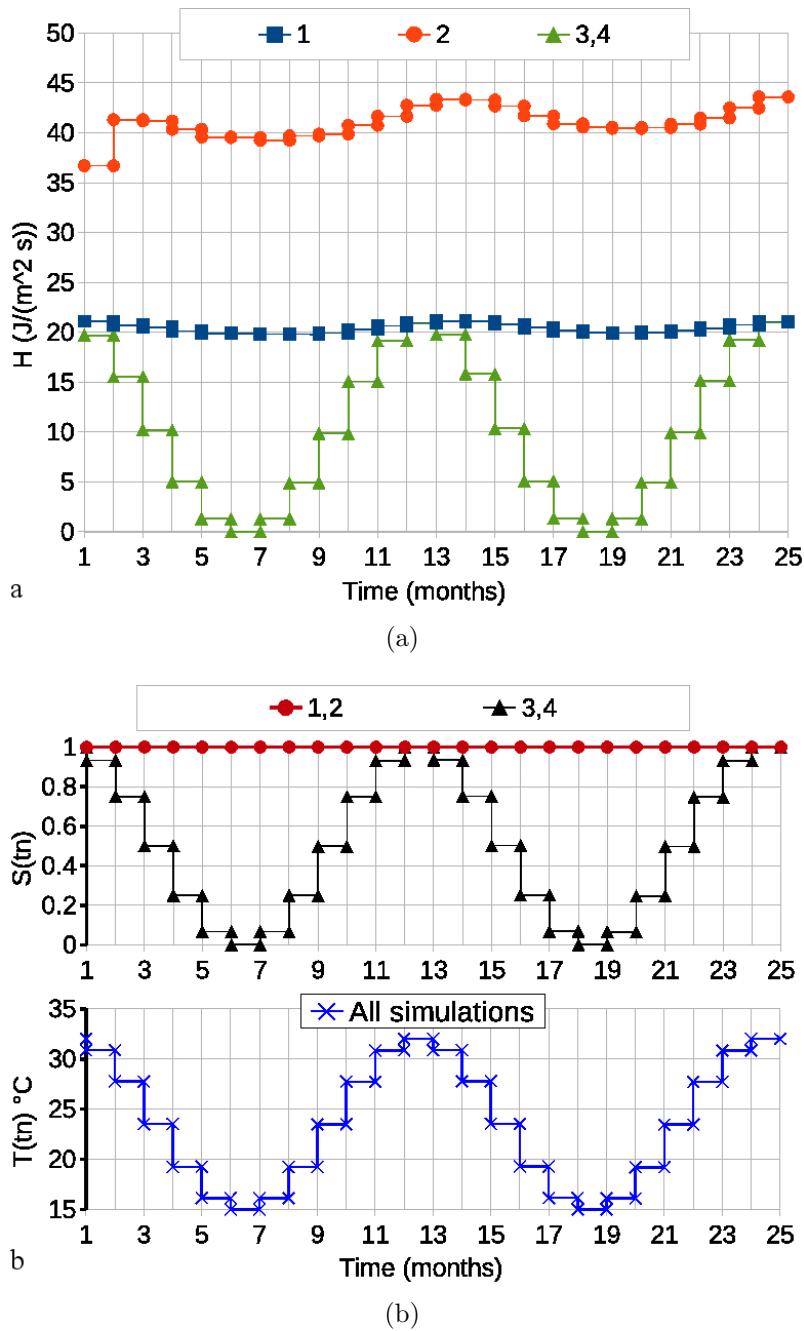
(a)

(b)

Figure 4.8: (a) Heat generation rate H (J/(m2 s)) through time near the axis of symmetry. (b) Efficiency of oxidation $S(t_n)$ and the temperature (°C) imposed along the upper boundary for the four simulations. All simulations start in summer.

69

efficiency of the oxidation process S(t_n), and to the methane flow rate ΦCH_4, according to the relation

$$\Psi CH_4(t_n) = \Phi CH_4(t_{n-1}) \cdot S(t_n) \tag{4.5}$$

The oxidation reaction implies the transformation of methane and oxygen into water and carbon dioxide. As I cannot simulate the production of carbon dioxide, I substitute methane with a corresponding quantity of nitrogen to avoid an unreal pressure drop associated with the methane removal. This little trick affects the gas density in the shallowest portion of the domain but is expected to have only a minor effect on the overall methane mass balance.

4.5   Simulation Results

All simulations start from the initial conditions illustrated in Figure 4.7, obtained with a methane flow along the boundary of $1 \cdot 10^{-7}$ $kg/(m^2s)$. At the beginning of the simulation, heat generation starts in the oxidation zone, based on the amount of gas that enters the zone. Figure 4.9 shows the distribution of liquid saturation and temperature for simulation 1, after 7 and 13 months, which are, respectively, the coldest months of the first winter and the hottest of the second summer. The basal methane flux is higher here than in the simulation run to achieve the initial steady condition. As a result, the liquid saturation in the aquifer decreases from the initial 0.9 (Figure 4.7 a) to 0.85 (Figure 4.9 a) in 7 months.

Similarly, the methane flow increases uniformly throughout the domain reaching $0.40 \cdot 10^{-6}$ $kg/(m^2s)$. The new value of liquid saturation is rather stable, and there are no significant changes after 13 months, while methane flow has a small increment during the summer period, when it reaches $0.42 \cdot 10^{-6}$ $kg/(m^2s)$. (Figure 4.9 b). The temperature, on the contrary, undergoes significant changes over a larger time frame. During the first winter, at 7 months, the upper portion of the domain is slightly warmer than initially (13°C), and the maximum temperature, at the depth of the heat sources, is 21°C (Figure 4.9c). This value reflects the heating history of this layer, with
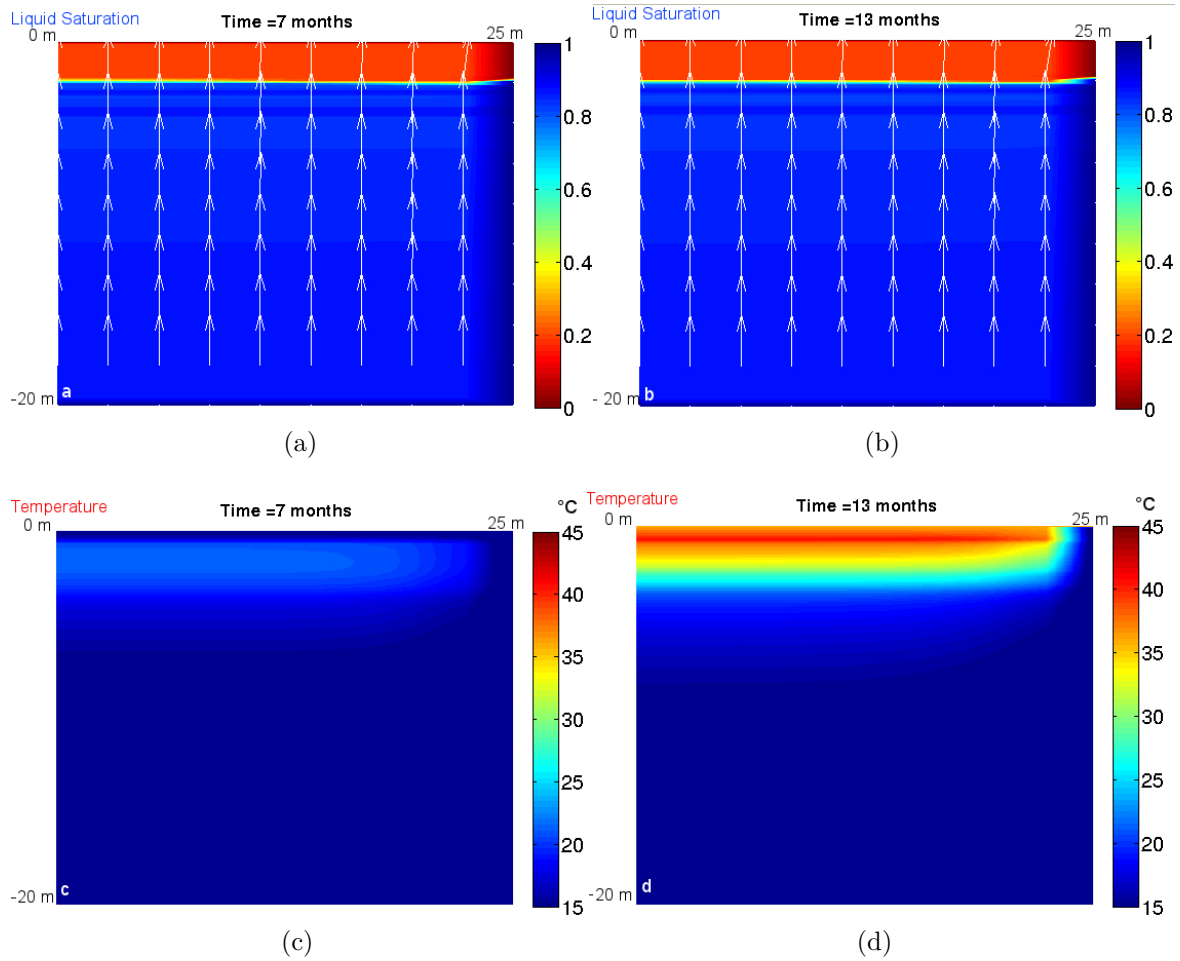
Figure 4.9: (a) Simulation 1. (a and b) Liquid saturation (color) and methane flux (white arrows) after 7 and 13 months, respectively. Methane fluxes range from 0 to $0.6 \cdot 10^{-6} kg/(m^2 s)$. (c and d) Temperature (°C) distribution after 7 and 13 months, respectively.

a larger contribution during the summer and a minor effect during the winter. After 13 months (Figure 4.9d), the summer heating raises the temperature to a maximum of 41°C, where the oxidation takes place, while at 10 m depth, the temperature is 15°C (2°C higher than at the initial steady state). Figure 4.10 shows the simulated and measured temperature profiles along the axis of symmetry from 0 to 10 m depth. The profiles are obtained for all the simulations after 2 months of simulation and then at 2 times during winter (7 and 19 months), 2 times during summer (13 and 25 months). The summer and winter profiles represent the upper and lower limits for the temperature distribution obtained in the intermediate periods (not shown). In all simulations, the surface temperature ranges from 13°C in winter to 36°C in summer, following the periodic trend imposed along the upper boundary of the model. The maximum temperature is always reached within the oxidation zone during the summer, while at 10 m depth, the temperature never exceeds 19°C in all simulations. In simulation 1 (Figure 4.10a), after 2 months, the temperature profile has a good fit with the observations, while after 7 months (first winter), the maximum temperature is 21°C at 1.6 m depth, while the peak where oxidation takes place is smoother. After 13 months, during the following summer, the temperature profile reaches the maximum value of 41°C at 0.6 m, then the temperature declines gradually to a minimum of 15°C at 10 m depth. The temperature profiles of the following winter (19 months) and summer (25 months) are very similar to the previous ones, although in both cases, the temperatures are slightly warmer: the second winter reaches a maximum of 23°C, while the second summer is 3°C warmer than the previous one at depths greater than 4 m. In simulation 2 (Figure 4.10b), the basal methane flux is higher and the heat generation is larger (Figure 4.7b). As a result, the temperatures are always 2 to 7°C higher than those obtained in simulation 1. The peak temperatures reached during the two summers is about 47°C, while in winter (19 months), the highest temperature is 29°C (at a depth of 1.5 m). In the simulation 3 (Figure 4.10c), where the bacterial activity is periodic, the temperature profiles in summer are similar to those of simulation 1 (maximum temperature is 41°C at 13 months). The major difference occurs during winter times when the bacterial activity is very low (zero during the twelfth and eighteenth month): the temperatures tend to return to the initial value of 13°C, and the maximum value is only 20°C at 19 months (-3.0 m). The temperature profiles of simulation 4 are the same as obtained with simulation 3, showing that the applied methane sinks do
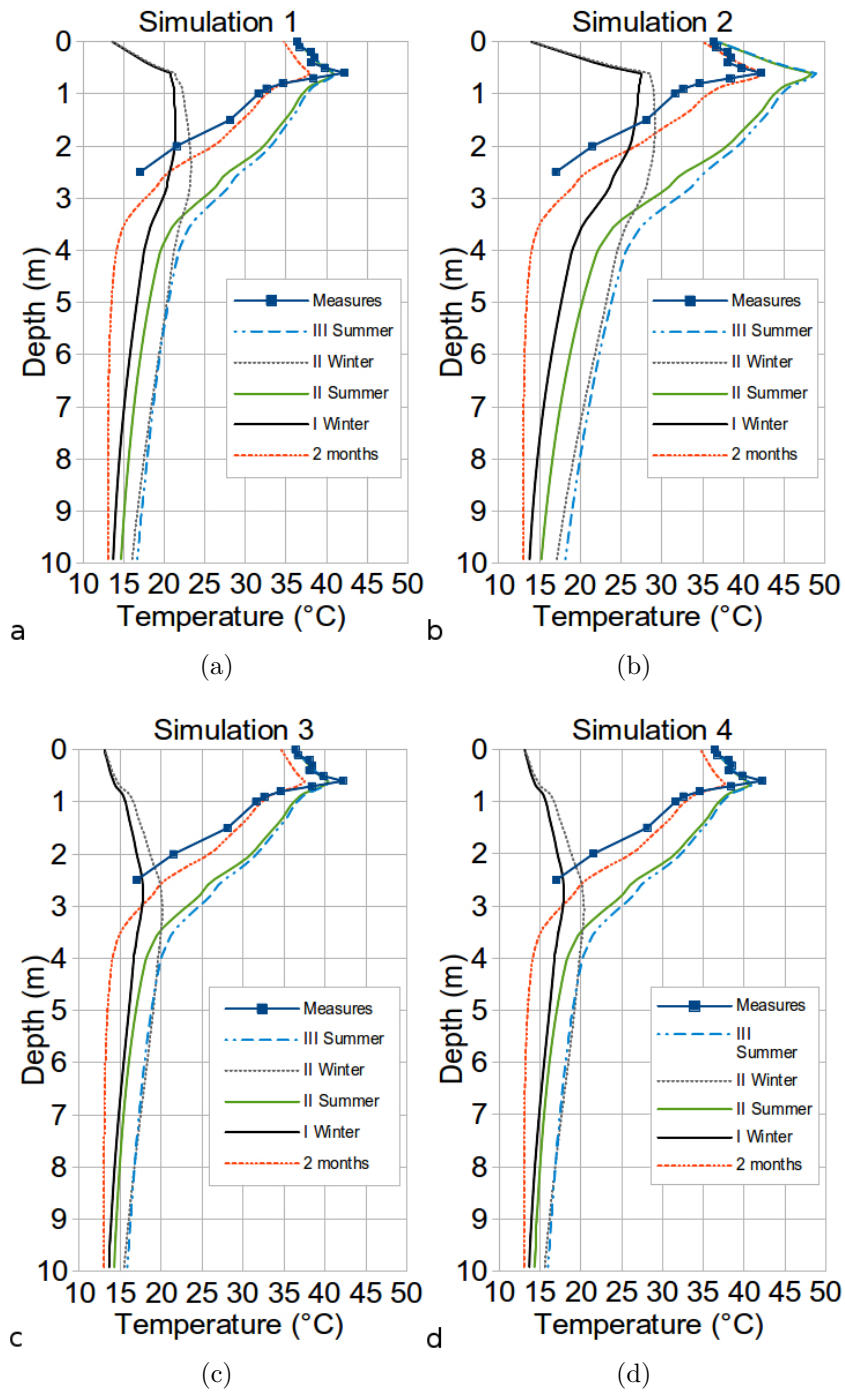
(a)

(b)

(c)

(d)

Figure 4.10: Temperature profiles in the four simulations at different times (shallowest 10 m). The I and II winter correspond to 7 and 19 months, respectively, while the II and III summer correspond to 13 and 25 months. The blue squares represent the temperatures measured in the survey.
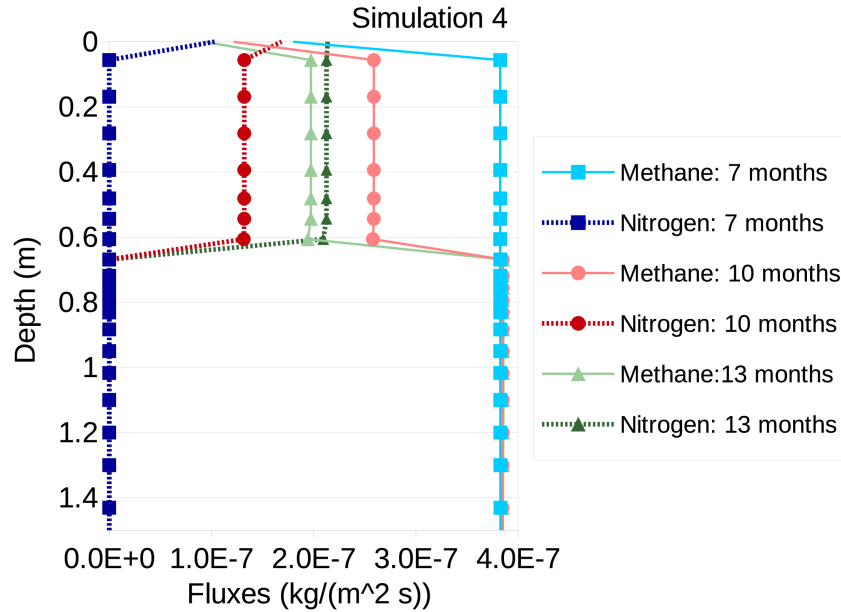
Figure 4.11: Simulation 4. Profile of CH_4 and N_2 vertical fluxes near the axis of symmetry.

not affect the temperature distribution. The methane flow in simulations 1 (Figures 4.9a and 4.9b), 2, and 3 (not shown) is almost constant throughout the profile and in time, while in simulation 4, it changes seasonally in the shallowest layers due to the periodicity that affects the oxidation process and hence the removal of methane (equation (4)). Figure 4.11 shows the vertical flow rate of methane and nitrogen obtained in simulation 4 as a function of depth for the first 1.5 m along the axis of symmetry and at three different times.

At depths greater than 0.7 m, the methane flow is constant throughout the year and corresponds to the basal flux assigned along the bottom ($0.40 \cdot 10^{-6}$ $kg/(m^{-6}s)$). The nitrogen flow at these depths is zero. During the first winter (7 months), these flux values characterize the entire domain and only change near the upper boundary, where fixed atmospheric conditions are assigned. After 10 months, between winter and summer, the oxidation reaction becomes more efficient and methane flow in the upper portion of the domain decreases to $0.26 \cdot 10^{-6}$ $kg/(m^2 s)$, while nitrogen generated as a dummy product of the oxidation reaction and its flow reaches a value of $0.13 \cdot 10^{-6}$ $kg/(m^2 s)$. After 13 months (summer), the efficiency of oxidation reaches a maximum: the

methane flow drops to $0.20 \cdot 10^{-6}\ kg/(m^2 s)$, while the nitrogen flow reaches $0.21 \cdot 10^{-6}\ kg/(m^2 s)$. Following the hypothesis that the microseepage of CO_2 is mostly produced by the oxidative conversion of CH_4, the corresponding CH_4 fluxes removed by oxidation vary from 0 to $5.0 \cdot 10^{-6}\ kg/(m^2 s)$, with a mean value of $0.26 \cdot 10^{-6}\ kg/(m^2 s)$, (Capaccioni et al., 2015), that is well comparable with the simulation 4 results.

4.6   Earthquake and methane seepage

The question that I can ask now is: "May the earthquake have increased the methane seepage?". The interaction between seismicity and hydrocarbon seepage has been studied in several works (Dando et al., 1994; Fischer et al., 2013) that suggest that the shaking and the stress variations induced by the earthquake can favor the migration of gases trapped in deep structures. In our assumption the methane is produced from the degradation of organic matter at tens or hundreds of meters of depth. In the previous chapter I showed that the earthquake of the 20 May 2012 led to a static stress change in the near field and probably a similar effect there was also during the 29 May 2012 earthquake. We have seen that the water wells levels variations can be explained assuming that the static stress change was sufficient to deform the terrain even at small depth. Figure 4.12 shows the dilation map computed in the previous chapter and the position of the survey used in this chapter. The survey is located between the MO80-00 and the MO43-01 wells and it is placed in the edge of the compression zone. It is reasonable to assume that the soil compression and therefore the pore pressure increase might have favored the rise of natural gas from the production area. However, the rock pores compression is not sufficient to justify the methane rise, which can only occurs in presence of a pressure gradient with the appropriate direction and magnitude. We don't have any data of the methane flow before the earthquake so we can't assume with certainty that the methane seepage has increased after the earthquake, but the fact that the Terre Calde area is in a compressive stress zone, does not allow us to exclude this effect a priori.
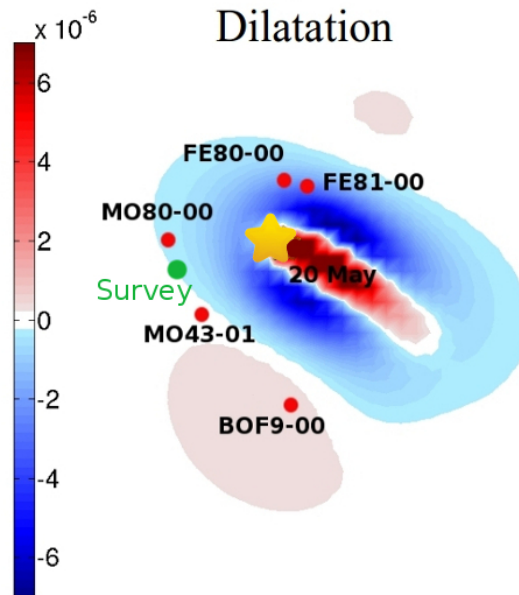
Figure 4.12: Dilation map computed for the 20 May 2012 earthquake. The green dot represent the survey position

4.7   Discussion and Conclusions

The measurements of temperature and concentration of the gaseous species observed at Terre Calde (Figure 4.4) show a clear anomaly at depths ranging from 0.5 m to 0.7 m. At this depth, we measured the maximum temperature, while the concentrations of the gases have a sharp variation. These findings suggest that methane, generated by anaerobic degradation of organic matter, undergoes exothermic oxidation by methanotrophic bacteria near the surface. To verify whether this process could be the actual cause of the observed heat anomaly, I performed some numerical simulations constrained by the local stratigraphy and by the measurements of methane flux carried out in the survey. In our simulation, heat sources are placed within the shallow oxidation zone, and heat generation is computed every month as a function of the methane flux entering the layer. Our results show that the temperature distribution obtained by this mechanism is consistent with observations. Our hypothesis is that the methane oxidation is facilitated by the presence of the fine sand layer found between 0.7 and 0.85 m and that due to its high permeability, there is a fast oxygen and methane recharge to feed the aerobic

bacterial activity. In all simulations, I have assumed a periodic temperature condition on the upper boundary, because at shallow depth, the seasonal temperature variations are not negligible and are expected to affect both the heat flow and the bacterial activity. Due to this simulated periodicity, the winter temperatures drops along the entire profile, and even after 2 years, the temperature profiles in summer are not linear, as would be expected in a system with constant temperature gradient. Our simulations show that temperature fluctuations affect the methane flux that enters the oxidation zone, and hence, the heat generated during the different periods of the year. Fluctuations in barometric pressure are also expected to cause even bigger changes in the flow rate of rising gases (Rinaldi et al., 2012) and should be addressed in further studies. Our simulations also account for the seasonal variation in bacterial activity, as observed by Chanton and Liptay (2000) in some methanotrophic bacteria populations that live in the subsurface of a landfill in Country Leon (Florida). Our results suggest that a winter drop in bacterial activity hinders the shallow heating during the cold months but does not affect the temperature distribution and the peak value reached during the summer (Figure 4.10). The lack of snow accumulation in the area of Terre Calde suggests that a small quantity of methane is also oxidized during winter times. Near-surface temperatures range between 8 and 16°C in simulations, where bacterial activity does not change through time, but are as high as 7°C when seasonal variations are accounted for. Simulation 4 also represents the consumption of CH_4 due to oxidation by replacing methane with an equal amount of gas. The greater oxidation that takes place during the summer involves a greater consumption of CH_4, which results in a decrease of the CH_4 flux at the surface. In contrast, the flow is maximum during the winter, as measured also by (Chanton and Liptay, 2000), and this periodicity can be useful to monitor the bacteria oxidation. In conclusion, our model confirms that the temperatures measured at Terre Calde may be entirely due to the oxidation of CH_4 produced within a peat layer at greater depths. The extremely localized depth at which oxidation takes place makes it very plausible that the production of heat is carried out by bacterial populations in aerobic conditions. Unfortunately, we do not have campaign measures before July 2012, and we cannot verify if the methane fluxes have undergone changes due to the main shock of 20 May 2012. Despite the fact that the earthquake may have affected the fluid flow and possibly the overall heat distribution, the process that heats the Terre Calde always occurs, regardless of the seismic

activity in the area. The progress of the study in Terre Calde, through the acquisition of other data with greater spatial and temporal distribution, will improve our understanding of the process that could have interesting applications in the energy field.

CHAPTER 5

COUPLED FLUID FLOW
MECHANICAL-STATISTICAL MODEL FOR THE
STUDY OF INJECTION-INDUCED SEISMICITY

Contents

The results shown in this chapter are published in Nespoli et al. (2015a).

Understanding the triggering mechanism is a fundamental step towards controlling the seismicity generated by deep underground exploitation. Here I

propose a modeling approach based on coupling the TOUGH2/EOS3 simulator with a geomehcanical-statistical model. The THM-statistical model provides a good representation of several mechanisms influencing each other during and after the injection phase. Each mechanism affects the induced seismicity in a different way and at different times during the reservoir stimulation, confirming that more sophisticated models are required to explain such a complex interaction.

5.1 State of art

Deep underground exploitation sometimes leads to an increase of the local seismicity, posing potential hazard for the local community (Ellsworth, 2013). Thus, understanding how to avoid large earthquakes plays a crucial role in the success of deep geo-energy exploitation. The correlation between underground fluid injection and seismicity is an issue that has been extensively studied (e.g. Shapiro and Dinske, 2009; Ellsworth, 2013). During fluid injection, although seismicity is generally controlled by fluid overpressure (e.g. Rinaldi et al., 2014), it is not possible to rule out some other mechanisms such as stress transfers between neighboring asperities, or temperature effects (Catalli et al., 2013; Dublanchet et al., 2013). In these conditions, the relationship between fluid pressure and induced seismicity is much more complex. Moreover, while current modeling approaches focus mostly on the active injection phase, the static stress transfer may become important at later stage during the post-injection phase (Catalli et al., 2013). Many efforts have been focused in the last years aiming at understanding the coupling between fluid flow and geomechanics processes, as well as induced seismicity. Studies have been performed accounting for lab experiments (e.g. Samuelson and Spiers, 2012; Guglielmi et al., 2015) as well as numerical modeling. These latter include: (a) fully coupled thermo-hydro-mechanical 3D numerical models (e.g. Rutqvist et al., 2002; Rutqvist, 2011; Rutqvist et al., 2015), (b) purely statistical models (Bachmann et al., 2011; Shapiro et al., 2010), and (c) hybrid models combining statistical and physical considerations (e.g. Bachmann et al., 2012; Goertz-Allmann and Wiemer, 2013; Gischig and Wiemer, 2013; Gischig et al., 2014).
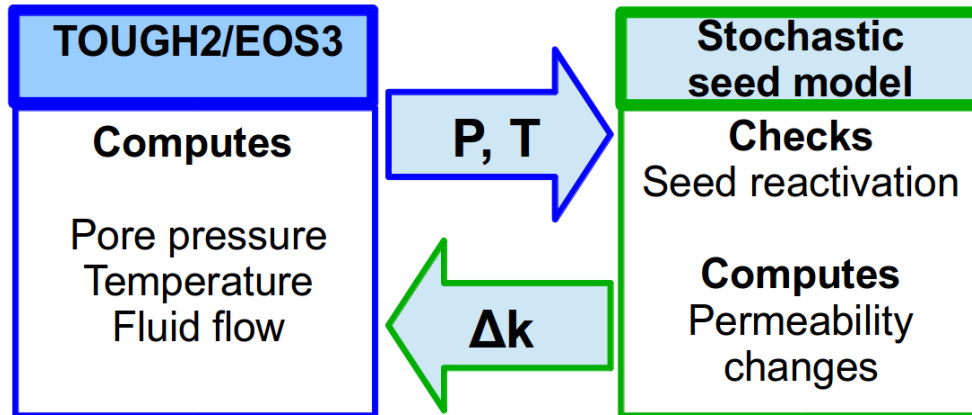
Figure 5.1: Coupling scheme between TOUGH2 and the stochastic seed model.

5.2 Numerical modeling approach

Following the so-called "seed model" proposed by Gischig and Wiemer (2013), I present an improved version of the modeling approach, in which the transient pressure and temperature from TOUGH2 are used to calculate the stress changes on distributed "seed points", representing potential earthquake hypocenters. Assuming a Mohr–Coulomb failure criterion, I evaluate at each time step if a seed point has the critical condition for reactivation given the pressure and temperature change at the seed location. The previous models (Gischig and Wiemer, 2013) were improved by using TOUGH2 (Pruess et al., 2012) as fluid flow simulator, which allows a full 3D formulation. I also account for transient, implicit permeability changes, which depend on pressure variation. If a seed is reactivated, I calculate a further permeability enhancement (either slip- or plastic strain-dependent) that is then fed back to TOUGH2. The geomechanical-statistical model was also improved by accounting a 3D stress field including the orientation (dip and strike) for each possible earthquake location (seed). Furthermore, the TOUGH2-SEED model can also account for static stress transfer, allowing the reactivation of cascade events at the same time step. The working scheme of our model is represented in Figure 5.1. I follow an explicit coupling scheme: at each time step the TOUGH2 simulator computes the fluid flow through a porous medium, and both temperature (T) and pore pressure (p) are interpolated to a random uniform distribution of seeds (i.e. potential earthquake hypocenters).

Chapter 5.   Coupled fluid flow mechanical-statistical model for the study of injection-induced seismicity

Such a scheme has been proven to be successful for coupled simulator (e.g. TOUGH-FLAC – Rutqvist (2011)). The diagonal terms of the effective stress tensor of each seed are updated according to (5.1).

$$\sigma'_{kk} = \sigma_{kk} - p + \beta K \Delta T \tag{5.1}$$

where σ'_{kk} is the kk component of the effective stress, accounting for both pore pressure and thermal effects. To note that in this chapter we use positive stress for compression. K is the bulk modulus and β is the volumetric thermal expansion coefficient. While in Gischig and Wiemer (2013) the stress regime is defined by the two principal stresses components, in our improved version I can define a more general 3D stress field, accounting for both strike-slip and dip-slip stress regime. In our model the initial three principal stress components of each seed are proportional to the lithostatic, depth-dependent pressure (p_{lit}), plus a random variation to mimic heterogeneities in the stress field. Assuming a fault orientation for each possible hypocenter (seeds), the shear τ and normal stress σ_n component variations are computed at each seed location. The stress tensor is projected to an arbitrary oriented fault plane, defined by a strike (Φ) and dip angle (θ), and shear and normal effective stresses are computed following Zoback (2010). Finally, reactivation of a seed occurs following a Mohr-Coulomb criterion. Friction angle (μ_f) and cohesion (C) are assigned a priori with random deviation around an average value. After activation, that occur for $\tau \geq \tau_c$, with τ_c expressed as

$$\tau_c = C + \mu_f \sigma_n \tag{5.2}$$

the seed model calculates a stress drop. The stress drop, according to Gischig et al. (2014) is linearly related to the shear stress (5.3):

$$\Delta \tau = \Delta \tau_{coeff} \cdot (\tau - C)/\mu_f \tag{5.3}$$

$\Delta \tau_{coeff}$ is an arbitrary numerical coefficient and the shear stress is updated accordingly to (5.4).

$$\tau_{new} = \tau - \Delta \tau \tag{5.4}$$

The activation of a seed point is then associated with a seismic event, whose magnitude is randomly assigned from a power-law distribution with a b-value

corresponding to the seed differential stress (Gischig et al., 2014). I also account for permeability changes due to (i) pressure and/or (ii) slip on a given seed. The first permeability dependence is a reversible pressure-dependent permeability change (updated after Rinaldi et al., 2014) as expressed by

$$k_{hm} = k_0 e^{C_1 \left(\frac{\phi_{hm}}{\phi_0} - 1 \right)} \tag{5.5}$$

$$\Phi_{hm} = (\phi_0 - \phi_r) e^{\alpha \Delta p} + \phi_r \tag{5.6}$$

where C_1 and α are two empirical coefficients to obtain a 2-fold increase in permeability over a 10 MPa pressure increase. ϕ_0 and ϕ_r are initial stress-free porosity and the residual porosity, respectively. k_0 is the initial permeability. The second mechanism accounts for permeability variations due to the earthquakes, and it is based on a slip-dependent equation (5.7) (Gischig et al., 2014)

$$k_{hm} = k_0 \left[1 + C_2 \left(1 - exp \left\{ \frac{\Delta d}{d^*} \right\} \right) \right]^n \tag{5.7}$$

$$\Delta d = \frac{M_0}{G\pi} \left(\frac{16\Delta\tau}{7M_0} \right)^{\frac{2}{3}} \tag{5.8}$$

C_2 is a constant coefficient, d^* represents the slip scale, M_0 is the seismic moment and G is the shear modulus. This mechanism represents a very localized permeability variations, close to the triggered seeds (e.g. fracture opening, or slip on a fault zone), but in our model the permeability change is assigned to the gridblock containing the reactivated seed. It is worth of note that this permeability depends on the seismic moment, hence on the magnitude, which is randomly assigned.

5.3 Modeling results

The model domain is 4x4 km wide and 4 km deep (from -2 to -6 km of depth), with a total of 20412 elements. The mesh is finer in the central area of the domain, where I simulated an incremental injection of cold water up to 30 days, followed by 60 days of constant injection (up to 90 days). The flow rate increases up to 30 kg/s at a depth of 4000 m at the center of the numerical domain. All the boundaries are open with fixed hydrostatic and geothermal conditions. The initial permeability is uniform over the entire domain corresponding to 10^{-16} m^2, while the porosity is 0.01. Both hydraulic and geomechanic initial conditions were chosen to achieve a steady-state condition. 50000 seeds are uniformly distributed all over the domain. This assumption does not necessarily represent a real case, in which I could assume different densities of seeds in different zones of the domain, according to the measured seismicity of the area. Table 5.1 reports the values of the parameters that I used in the simulations.

Table 5.1: List of constant parameters used in the simulation.

Parameter	Value	Unit of measure
Thermal expansion (β)	$3 \cdot 10^{-5}$	$°C^{-1}$
Shear modulus (G)	5	GPa
Bulk modulus (K)	8.3	GPa
Stress drop coeff. ($\Delta\tau$ coeff)	0.09	/
Initial porosity (ϕ_0)	0.01	/
Residual porosity (ϕ_r)	0.005	/
Initial permeability (k_0)	10^{-16}	m^2
C_1	15	/
C_2	2	/
α	10^{-8}	Pa^{-1}
Critical slip (d^*)	$2 \cdot 10^{-3}$	m
Min-Max magnitude	0.85-9	/
Min-max differential stress for b-value	0-136	MPa

5.3.1 Base case results

The base case simulations are aimed to present the TOUGH2-SEED model, and as a comparison with the previous seed model (Gischig and Wiemer, 2013; Gischig et al., 2014). For these base case simulations, I assume a local stress field (strike-slip regime) with σ_{max}, σ_{min} and σ_{med} respectively oriented along x-, y-, and z-axis (Equation 5.9).

$$\sigma_{max} \approx 1.55 p_{lit} \qquad \sigma_{min} \approx 0.7 p_{lit} \qquad \sigma_{med} \approx p_{lit} \tag{5.9}$$

Each seed represents a strike slip fault with a strike angle $\Phi = 60°$ and a dip angle $\theta = 90°$. Simulation 1 only accounts for reversible pressure-dependent permeability changes (Equation (5.5)) while Simulation 2 accounts also for slip-dependent permeability (Equation (5.7)). In both simulations, I do not account for the stress transfer at this stage. Figure 5.2 shows the horizontal and vertical distribution of pore pressure changes for the two base case simulations at shut-in (90 days).

The pressure variation in Simulation 1 reaches a maximum around injection zone of about 30 MPa (Figure 5.2a), while in Simulation 2 the pore pressure variations are lower given a larger permeability changes: at 90 days do not exceed 10 MPa (Figure 5.2b). Figures 5.3 and 5.4 shows the horizontal and vertical sections of permeability in the two simulations at the end of the injection period, respectively. Simulation 1 shows permeability changes up to a maximum increase of about one order of magnitude (up to $10^{-15} m^2$) nearby the injection zone (Figure 5.3a). Given Equation (5.5), the permeability evolution strictly follows the pore pressure distribution. In Simulation 2 the effects of the two mechanisms of permeability enhancement are overlap (Figure 5.3b). Indeed, given Equation (5.7), a triggered seed produces a localized permeability increase, whose magnitude depends on the stress drop and seismic moment, that is randomly assign for each events. In Simulation 2 this relation between permeability and slip leads to scattered permeability changes up to $10^{-14} m^2$ (i.e. 2 order of magnitude increase). Worth of note is that the chosen permeability dependency leads to a different shape of overpressure in the domain: while in Simulation 1 the injection-induced overpressure evolves along an almost spherical front, in Simulation 2 the evolution is slightly anisotropic. My 3D model allows us also to capture the

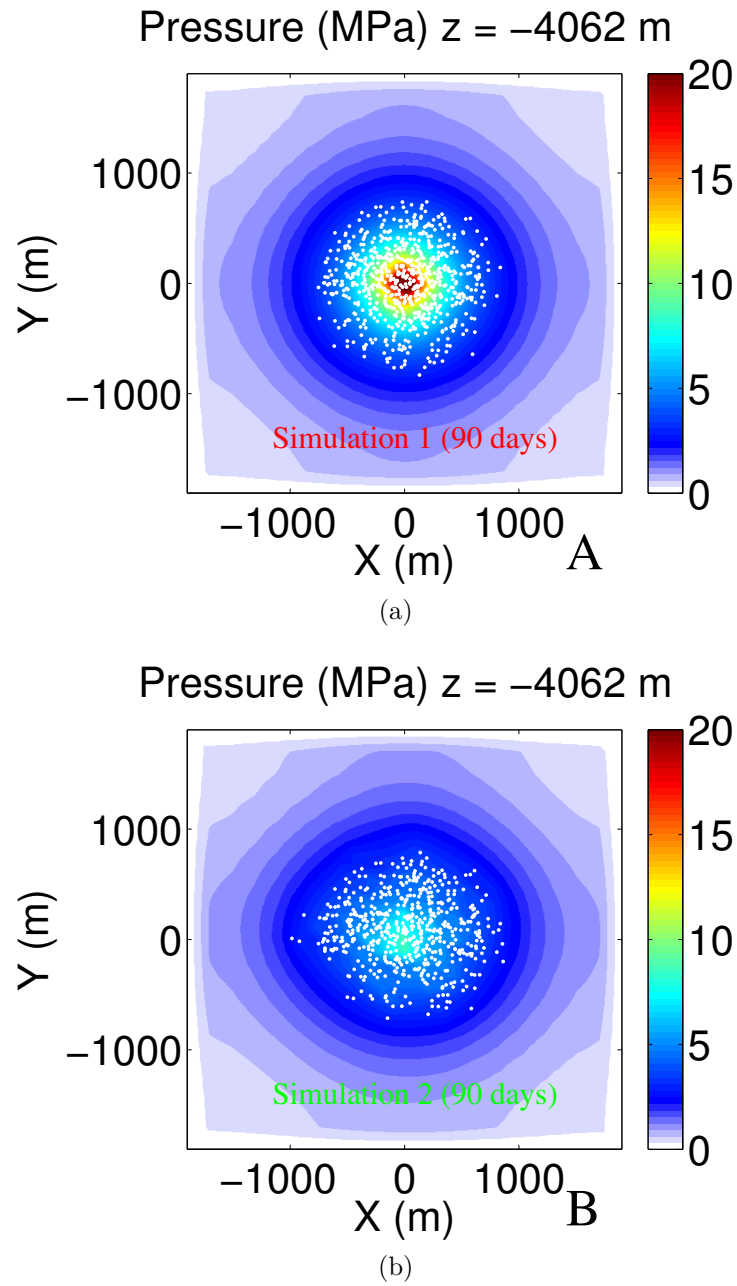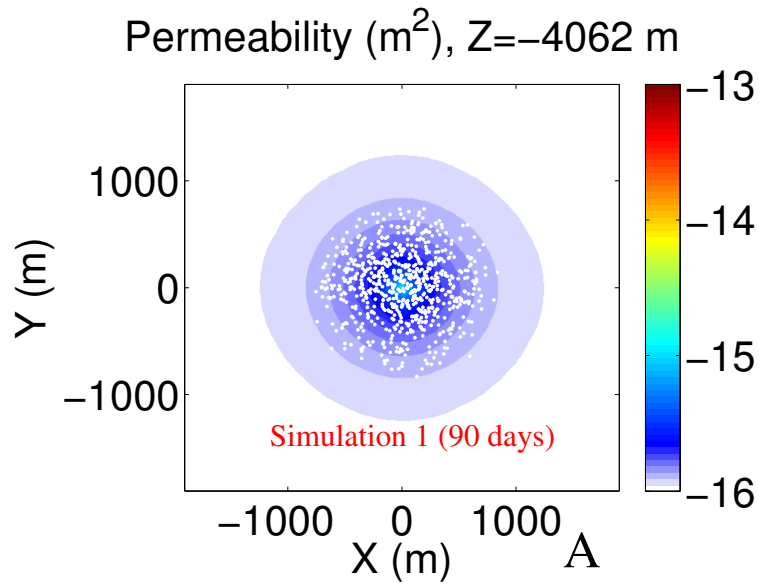## Pressure (MPa) z = −4062 m
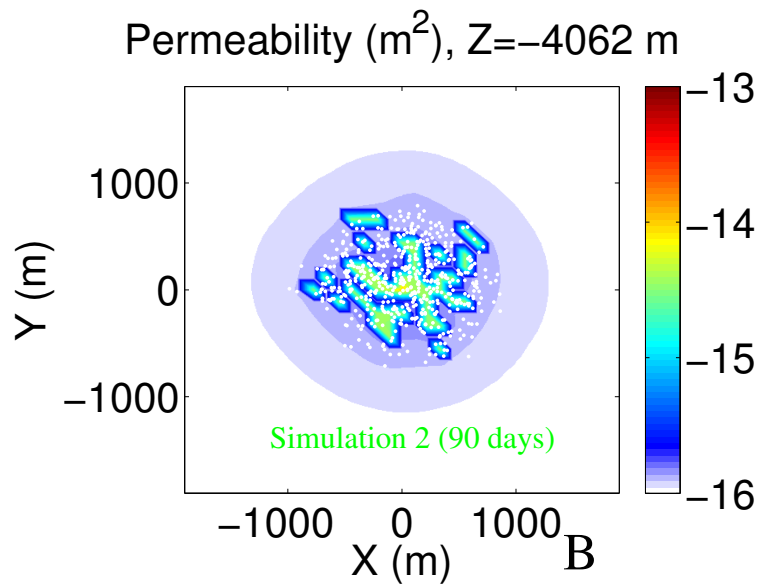
(a)

Pressure (MPa) z = −4062 m

(b)

Figure 5.2: Pressure. Horizontal sections at 90 days in (a) Simulations 1 (pressure-dependent permeability) and (b) Simulation 2 (pressure and slip-dependent permeability). The dots represent the triggered seeds after 90 days of injection.
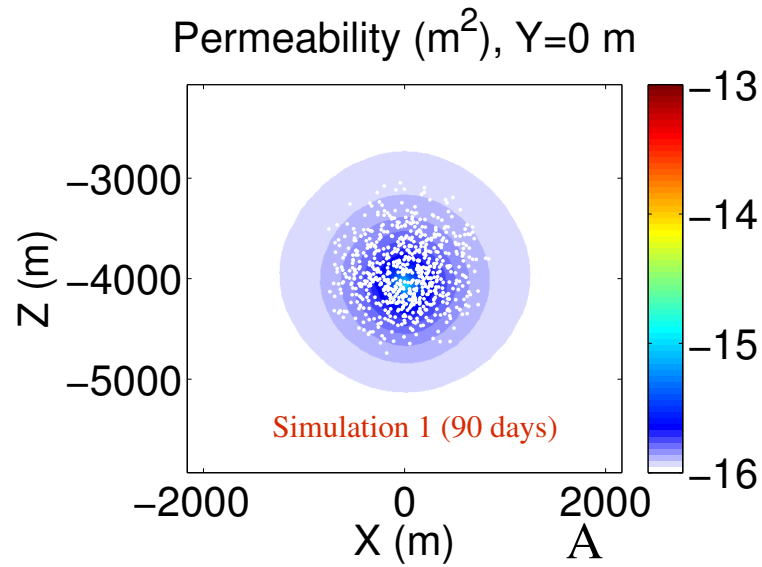
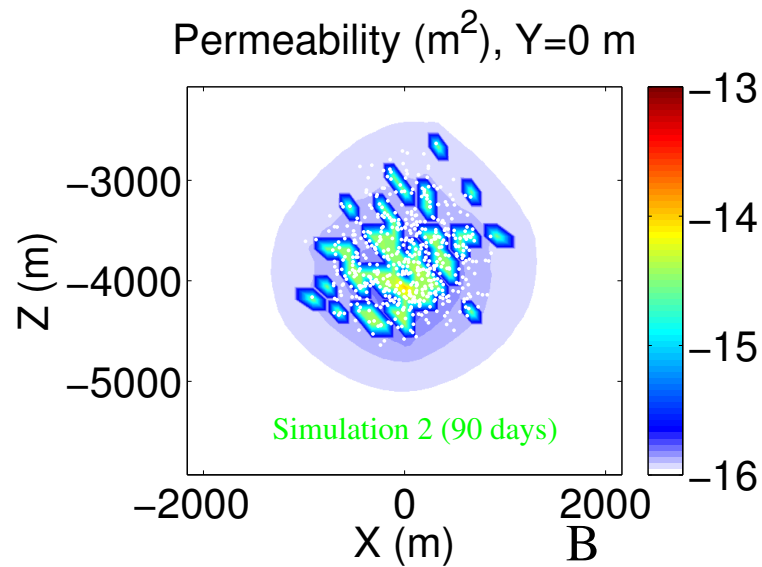Figure 5.3: Permeability. Horizontal sections at 90 days in (a) Simulations 1 (pressure-dependent permeability) and (b) Simulation 2 (pressure and slip-dependent permeability). Color= Permeability (m^2), dots=triggered seeds.

(a)

(b)

Figure 5.4: Permeability. Vertical sections at 90 days in (a) Simulations 1 (pressure-dependent permeability) and (b) Simulation 2 (pressure and slip-dependent permeability). Color= Permeability (m^2), dots=triggered seeds.

simulation behavior along the z-axis that should be quite different from the horizontal one. Figure 5.4 shows the vertical sections of permeability at 90 days for the two base cases simulations. The vertical distribution of the cloud of events in both simulations has not a spherical shape but rather a drop shape: the model favors the seismicity at greater depth. This behavior is due to the combination of depth-dependent stress field and the 3D fluid flow computed by TOUGH2.

5.3.1.1 Well pressure and number of events

In the Simulation 1 I obtained a total of 757 events over the entire simulated period, and 572 in the Simulation 2. Figure 5.5 shows the well overpressure and the number of events per 12 hours for the two base cases simulations. The well pressure in Simulation 1 increases by about 27 MPa during the step-injection (up to 30 days). During the constant injection period (30 to 90 days) the pressure shows a slower increase, reaching about 28 MPa at shut-in. In Simulation 2 after an initial pressure increase, a fast drop of about 3 MPa occurs, following then an irregular pattern during the entire step-injection phase (30 days) due to reactivation of seeds near the injection zone. The maximum pressure reached during the stimulation never exceeds 11 MPa. Generally, accounting for slip-dependent permeability means that when a large number of events occurs, the simulations will feature a larger and faster variation, like the initial spiked-like pressure change of Simulation 2 (Figure 5.5b). In both simulations, the number of events increases during the first 30 days and remains roughly constant during the late stage of injection. In both simulations few events occur during the post-injection phase (i.e. t>90 days).

5.3.1.2 Sensitivity analysis

To study the effects of some model parameters on the number of triggered events I performed a sensitivity analyses. In the first set of simulations I performed several simulations changing the initial values of σ_x from $\approx 1.6 p_{lit}$ to $\approx 1.4 p_{lit}$ and the stress drop coefficient $\Delta\tau_{coeff}$ from 0.01 to 0.09. The results only accounting for Equation 5.5 (Analysis1) are reported in Figure 5.6a, while the results obtained accounting also for Equation 5.7 (Analysis2) are shown in Figure 5.6b.
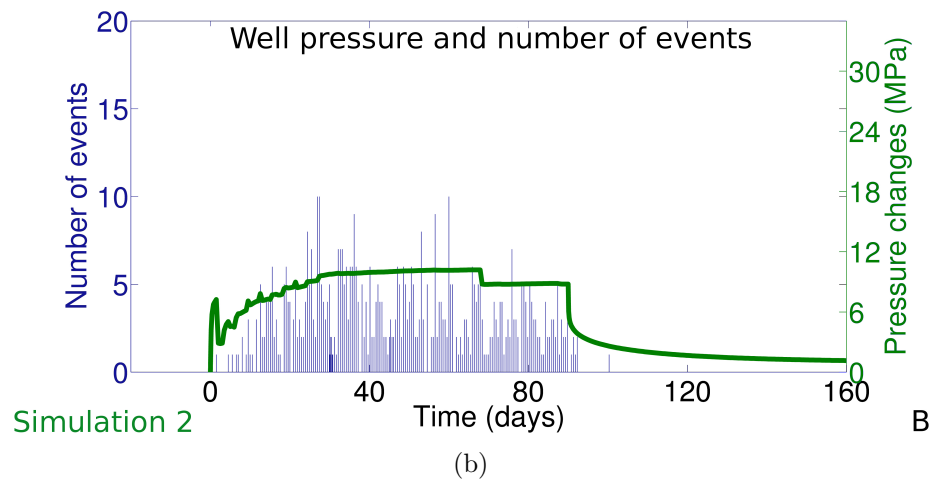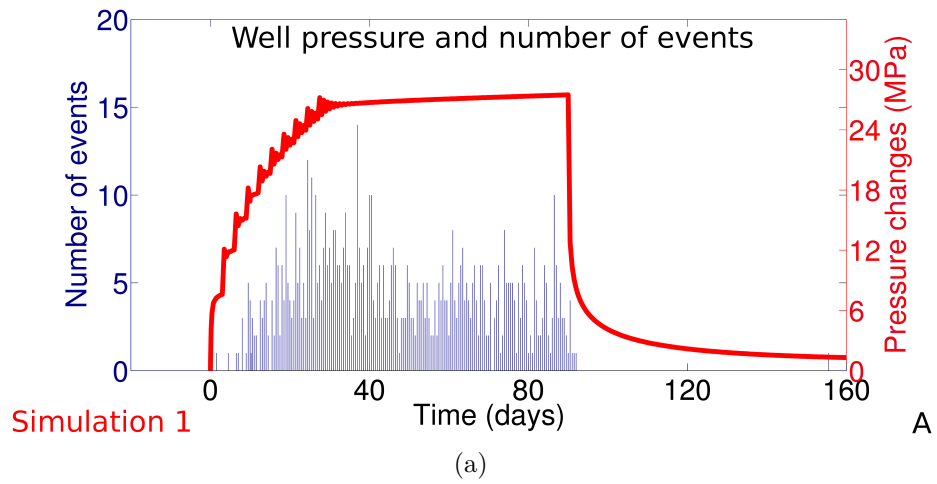
(a)

(b)

Figure 5.5: Well overpressure (lines) and number of events per 12 hours (histograms) for Simulation 1 (pressure-dependent permeability) (a) and Simulation 2 (pressure and slip-dependent permeability) (b).
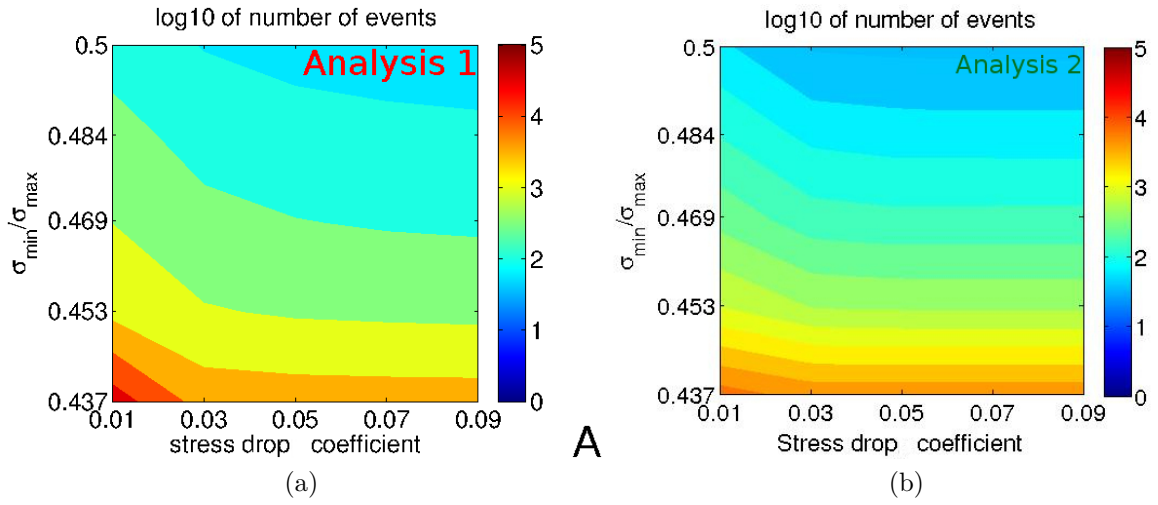
Figure 5.6: Number of events with different σ_y/σ_x ratio and $\Delta\tau_{coeff}$ using Equation 5.5 (Analysis 1) (a) and using Equation 5.5 + 5.7 (Analysis 2) (b). Colour is log10 of number of events.
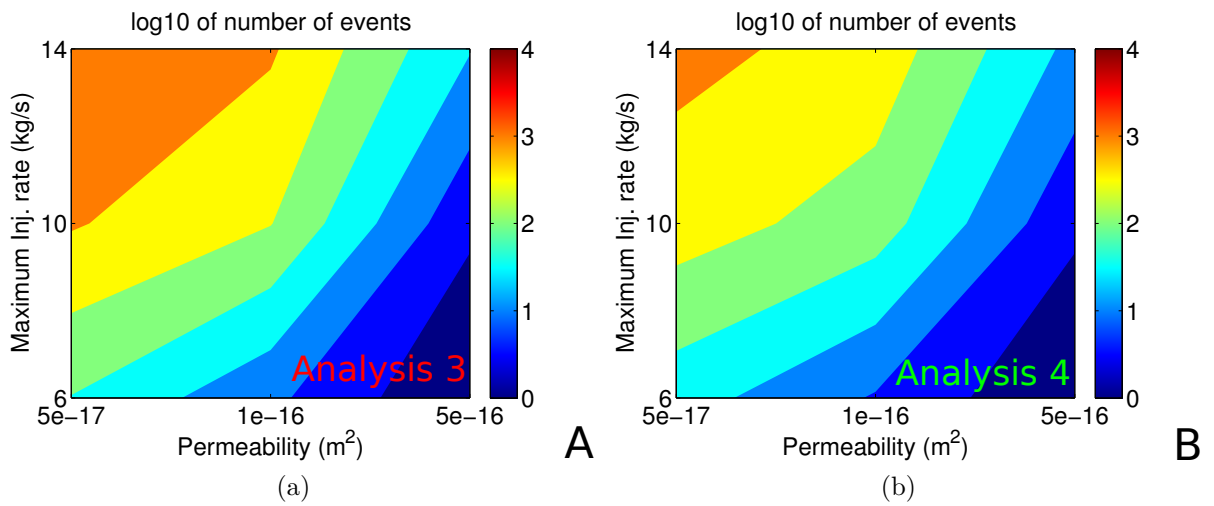

Figure 5.7: Number of events with different permeabilities and injection rates using Equation 5.5 (Analysis 3) (a) and using Equation 5.5 + 5.7 (Analysis 4) (b). Colour is log10 of number of events. The stress drop and the stress ratio are the same of the base case.

Both sensitivity analysis show a strong dependence on initial principal stress ratio and a weaker dependence on the stress drop coefficient. The case with a greater number of events in both set of simulations has the lowest stress ratio, 0.437 ($\sigma_x \approx 1.6 p_{lit}$) and the lowest stress drop coefficient, 0.01 and leads to 58888 events in Analysis 1 and 7911 events in Analysis 2. The best case scenario, obtained with a stress ratio of 0.5 ($\sigma_x \approx 1.4 p_{lit}$) and a stress drop coefficient of 0.09, generated 56 and 36 events in the Anlalysis 1 and in Analysis 2, respectively. To study the performance of the model, I performed other simulations using different initial permeability values (from $5 \cdot 10^{-17} m^2$ to $5 \cdot 10^{-16} m^2$) and injection rates (from 10 to 30 kg/s) The numbers of events triggered using 5.5 (Analysis 3) and 5.7 (Analysis 4) are shown in Figure 5.7. In these last sets of simulations the worst cases have the highest injection rate (30 kg/s) and the lowest initial permeability ($5 \cdot 10^{-17} m^2$) and produce respectively 3089 and 1395 events in Analysis 3 and Analysis 4. In all the sensitivity analysis the larger permeability changes (Equation 5.7), lead to the lower number of events.

5.3.2   Stress transfer

In the base case simulations I neglected the effect of static stress transfer among seeds. To account for such an effect on seed reactivation, and hence permeability and pressure distribution, I used a model first proposed by Baisch et al. (2010), which has been generalized for a full 3D formulation. This is an extremely simplified model which does not take into account the appropriate dislocation solution that is implemented in the next chapter. In brief, when a given seed is reactivated, the shear stresses of the eight neighbouring seeds on the fault plane are increased, considering a greater stress transfer along slip direction (Figure 5.8a). Therefore the stress transfer brings nearby seeds closer to the failure condition and may also involve a triggering or a re-triggering of several seeds within the same time step. Figure 5.8b shows an example of application of the stress transfer in TOUGH2-SEED. Assuming that the central blue dots is a triggered seed, the stress transfer function identifies the eight nearest seeds lying near the oriented fault plane (red dots) and it increases their tangent stress component τ according to the scheme shown in Figure 5.8a. In the next subsections I will show the results of two simulations: (i) Simulation 3 that is based on Simulation 2 but also
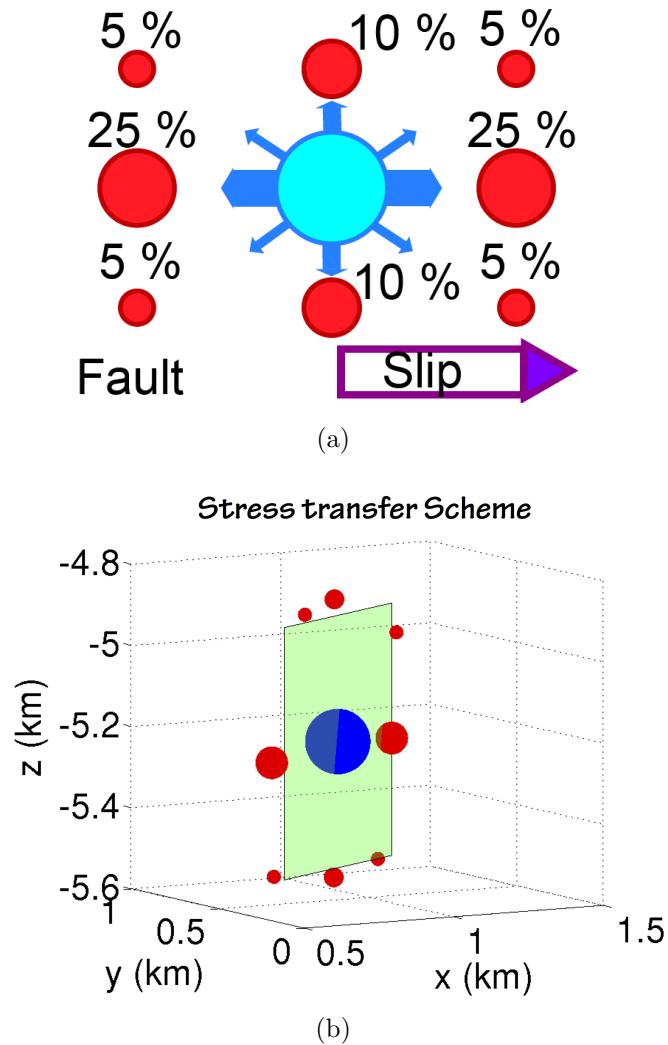
(a)

(b)

Figure 5.8: (a) Scheme of stress transfer, modified from Baish et al. (2010). (b) Example of the extremely simplified stress transfer model for the strike slip fault (green) used in the simulations. Blue dot is the triggered seed. Red dots are the 8 closest seeds lying in the fault plane. The dimensions are proportional to the magnitude of stress transfer.

accounting for the stress transfer (strike slip seeds); (ii) Simulation 4, aimed to study a case of dip slip regime.

5.3.2.1 Strike slip regime

The horizontal sections of permeability changes for Simulation 3 are shown in Figure 5.9a-c, at 30, 90, and 160 days, respectively, at a depth of 4000 m. The red line in figures represents the seeds' strike orientation (60°). Generally the stress transfer provides a greater number of events during the first stage of simulation, and its effects on the seed distribution are even more emphasized in the medium-later stage of injection. At 30 days the stress transfer produces a visible alignment of events (Figure 5.9a). After 90 days it is difficult to distinguish the effect of the stress transfer in the injection zone, due to the large number of triggered seeds. The effects of the stress transfer are mainly visible at the edges of the seismic cloud, where several fringes oriented along the direction of strike develop (Figure 5.9b). At 160 days new fringes are produced and the cascades of events induced by stress transfer increase the dimension of pre-existing fringes (Figure 5.9c). Unlike the previous base cases, in Simulation 3 I obtained a large number of seismic events even after shut-in. The well overpressure presents a temporal evolution similar to the one observed for the base case 2 (Figure 5.10, orange line), although reaching a lower maximum value (about 7 MPa), because of the larger number of events, hence a larger increase in permeability. The temporal evolution of the seismic events also distributes differently when compared to the base cases. The number of events progressively increases during the first 40 days of injection, remaining almost constant at the middle of the injection phase (40 to 60 days). The occurrence of events increases at later stage of injection because of the stress transfer (60 to 90 days), and finally after shut-in the occurrence of events largely decreases, but 273 events are still triggered during the post-injection phase. The total number of events increased from 572 in the base case to more than 2000 if the stress transfer is taken into account.
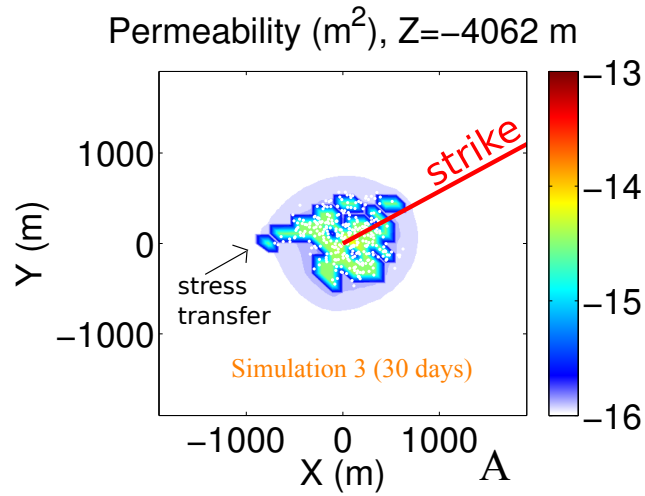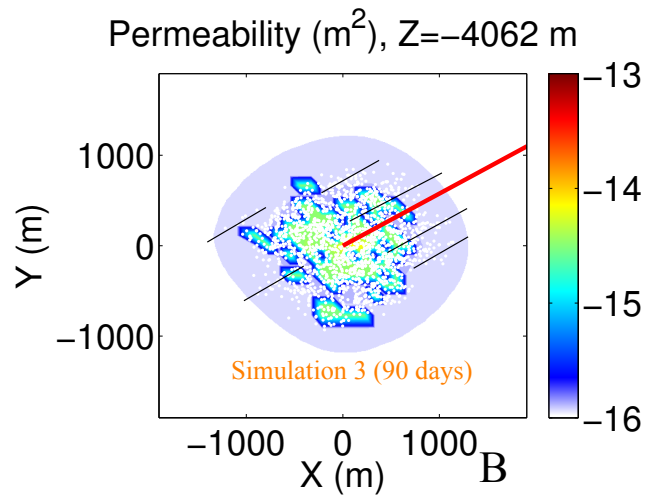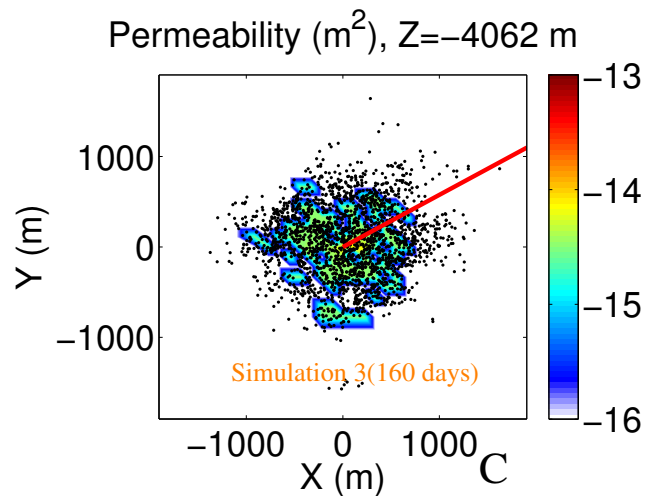
Figure 5.9: Permeability. Horizontal sections of Simulation 3 (All permeability changes and stress transfer for strike-slip faults) at (a) 30, (b) 90 and (c) 160 days. Color is permeability. The red line is the strike direction and the black lines highlight the stress transfer interaction.
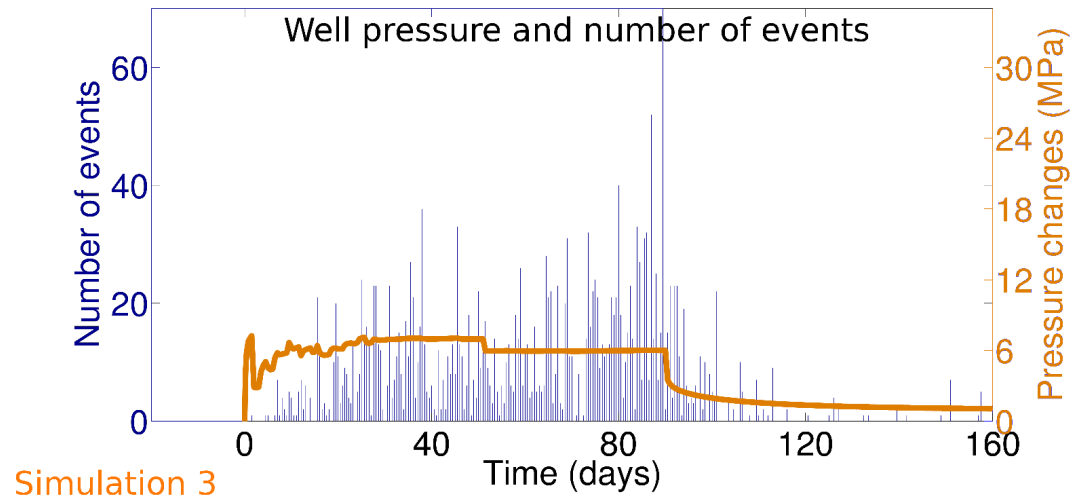
Figure 5.10: Well overpressure (line) and number of events per 12 hours (histograms) of simulation 3 (All permeability changes and stress transfer for strike-slip faults).

5.3.2.2   Dip slip regime

The TOUGH2-SEED model is also capable of represent an arbitrary 3D domain, with faults (seeds) oriented in any direction. The fault type, as well as the stress field regime, can be assigned as initial input by the user. In order to investigate this capability, I performed a further simulation (Simulation 4), assigning a different regional stress field (with the minimum principal stress component oriented along the z axis: $\sigma_{max} \approx 1.3 p_{lit}$ (x-axis), $\sigma_{min} \approx 0.6 p_{lit}$ (z-axis), $\sigma_{max} \approx p_{lit}$ (y-axis) to mimic a dip-slip regime. All seeds represent faults with the same strike angle $\phi = 0°$ and dip angle $\theta = 30°$. Figure 5.11 shows the vertical sections of permeability of Simulation 4 at 30 and 90 days. At 30 days the seismicity is mostly localized in a central area of 0.5x0.5 km and there the permeability increased of about one order of magnitude around the injection-zone (Figure 5.11a). After 90 days the seismicity extends to a greater area and seems, with a preferential path oriented along the dip direction and propagating toward shallower depths. The stress transfer, actually, makes it easier to trigger events along the dip direction, consequently leading to dip-oriented permeability changes.
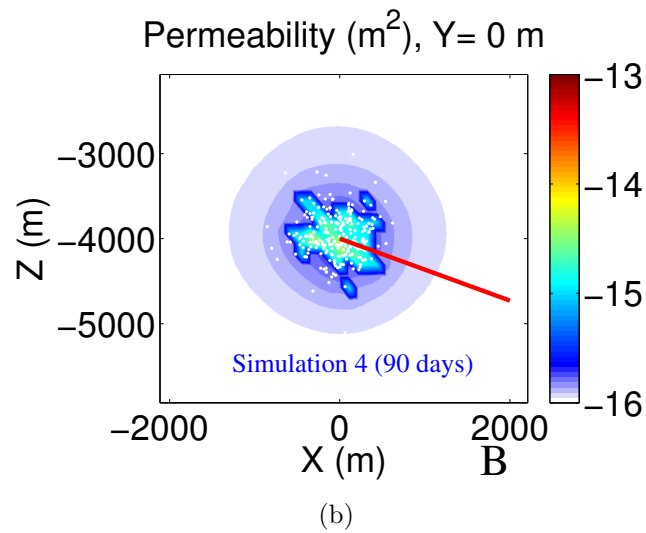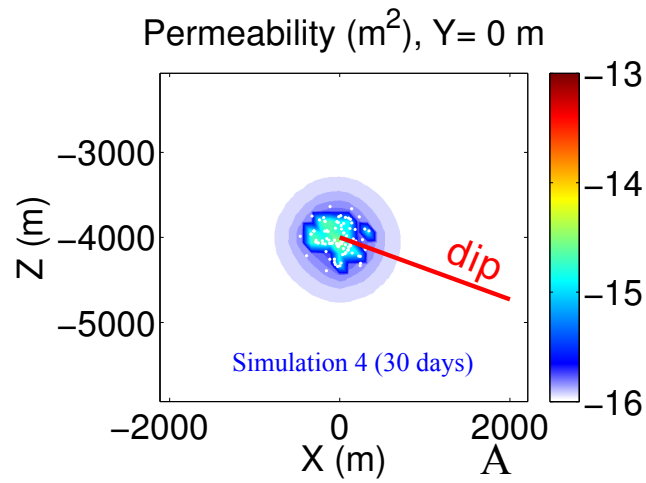
(a)

(b)

Figure 5.11: Permeability. Vertical sections of Simulation 4 (All permeability changes and stress transfer for dip-slip faults) at (a) 30, (b) 90 days. Color is permeability. The red line is the dip direction.

5.4 Discussion and conclusion

In this chapter I presented some features of the code TOUGH2-SEED. Such a simulator couples the capabilities of TOUGH2 as fluid flow simulator to a geomechanical-statistical code for the study of injection-induced seismicity during deep underground exploitation. I presented four different simulations. Simulation 1 and Simulation 2 show the effects of two different permeability enhancement processes. Assuming a reversible pressure-dependent permeability I obtained a regular and well-defined seismicity zone around the injection well. Considering irreversible slip-dependent permeability changes I obtained a more scattered permeability evolution that can consequently influence the pore pressure evolutions and then the whole seismicity. In both simulations the vertical sections show that the seismicity cloud is anisotropic and assumes a drop shape. Simulation 3 show the stress transfer effects. The most trivial consequence of the stress transfer is that it brings the seed closer to failure, and it may lead to cascade events. The stress transfer, however, not only influences the number of events, but also their spatial and temporal distribution. In the strike-slip case the stress transfer produces several strike-oriented fringes in the seismicity clouds, triggering events at greater distance than the base case simulation. In the dip slip case (Simulation 4) the stress transfer leads to larger permeability changes along the dip direction. Finally the stress transfer can also massively influence the temporal distribution of the events: indeed a large number of events are observed at a later stage of injection and even after shut-in. This behavior is somewhat in agreement with real observation. For example at EGS project in Basel (to be discussed in the next chapter), the major events only occurred after shutin, and the temporal distribution of the seismicity showed that the rate of events increased at the later stage of injection (Catalli et al., 2013). With the TOUGH2-SEED model I can simulate up to a certain, limited extent the complex joint interaction between fluid flow and geomechanics. Compared to the pre-existing model, I account for a more sophisticated fluid flow simulator, such as TOUGH2. Moreover, our improvements to the geomechanical-statistical seed model allow capturing effects that are impossible to represent on a simpler 2D model. Although several effects are not considered (e.g. poroelasticity, fracture creation/propagation), the TOUGH2-SEED model represents an initial step to the representation of physics-based processes into statistical model. The mechanical coupling can influence the seismicity at very different spatial and

temporal scales, leaving open the way for the creation of more complex and realistic models.

CHAPTER 6

A MODEL APPLICATION: THE BASEL STIMULATION
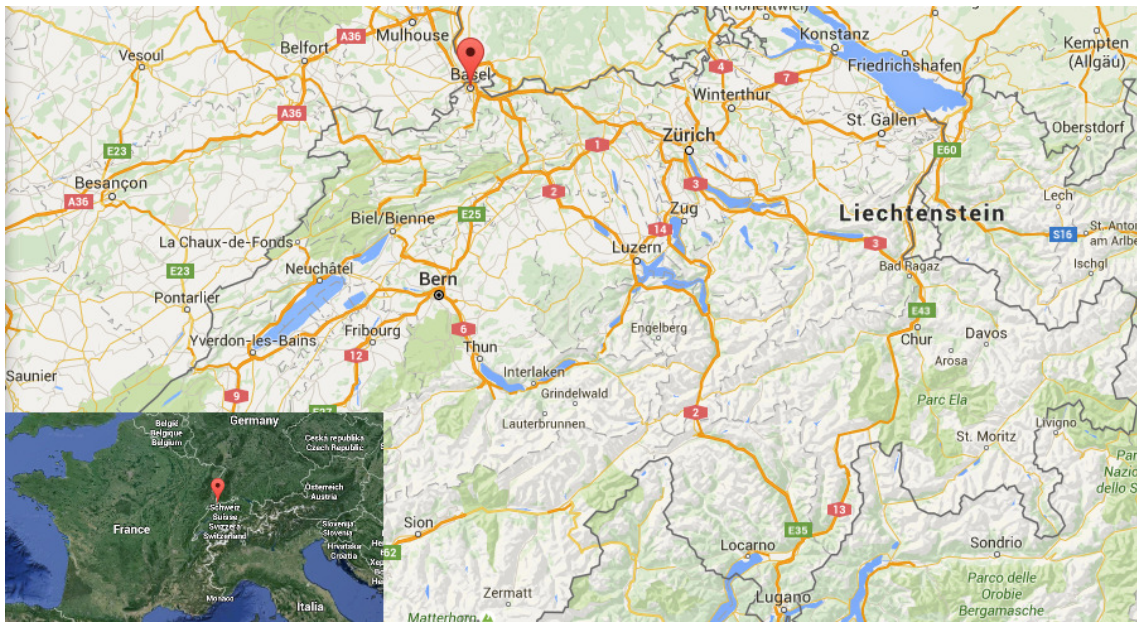
Figure 6.1: Map of Switzerland. The red pointer indicates the Basel position. Map is taken from google maps.

The geothermal system of Basel (Switzerland), Figure 6.1, is widely studied because of the large number of data and measurements made during and after partial stimulation of an Enhanced Geothermal System (EGS). The case is very useful to study the relationship between deep fluids injection and induced seismicity, and it can be suitably used as a benchmark to test the capabilities of TOUGH2-seed.

At Basel EGS, the stimulation started on December 2, 2006 and lasted 6 days until the $M_L = 2.6$ earthquake that happened on December 8 (Häring et al., 2008). Originally the injection phase was to last 21 days, but due to the high seismicity rate, the injection was initially reduced and finally stopped (Figure 6.2).
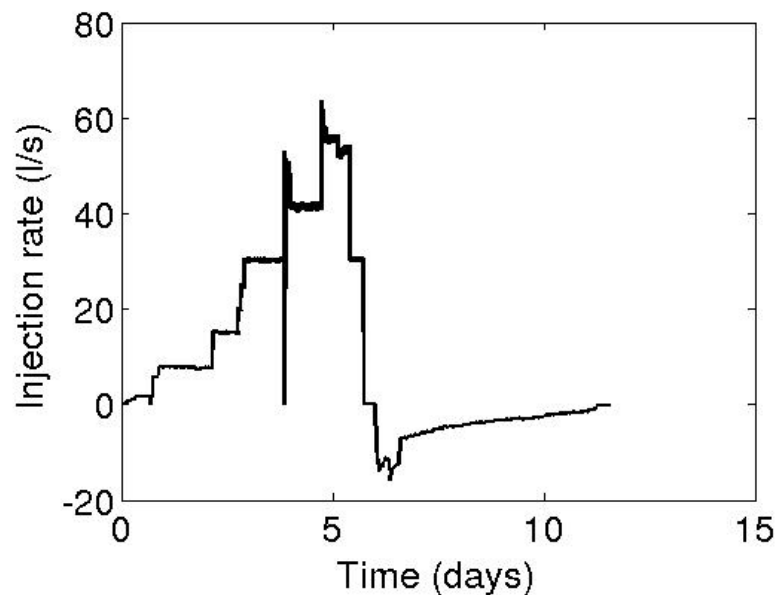
Figure 6.2: Injection rate of water during the Basel's stimulation

During this period about 11,570 m^3 of water were injected and more than 10,500 earthquakes were induced around the injection well at about 5 km depth (the open hole section was open from 4632 to 5009 m of depth) (Häring et al., 2008; Catalli et al., 2013). The injection rate increased in steps up to a maximum of 63 l/s and also the wellhead pressure evolution generally follows the injection rate trend reaching its maximum (29.6 MPa) at the end of the stimulation (Figure 6.3). The two spikes of the wellhead pressure are

related to mechanical repairs of the well. Also the seismicity blandly followed the injection rate evolution (Figure 6.3): the number of events increased progressively during the injection phase and then rapidly decreased after the shut in and other 3 events of magnitude greater than $M_L = 3$ occurred within the following 2 months (Bachmann et al., 2011).
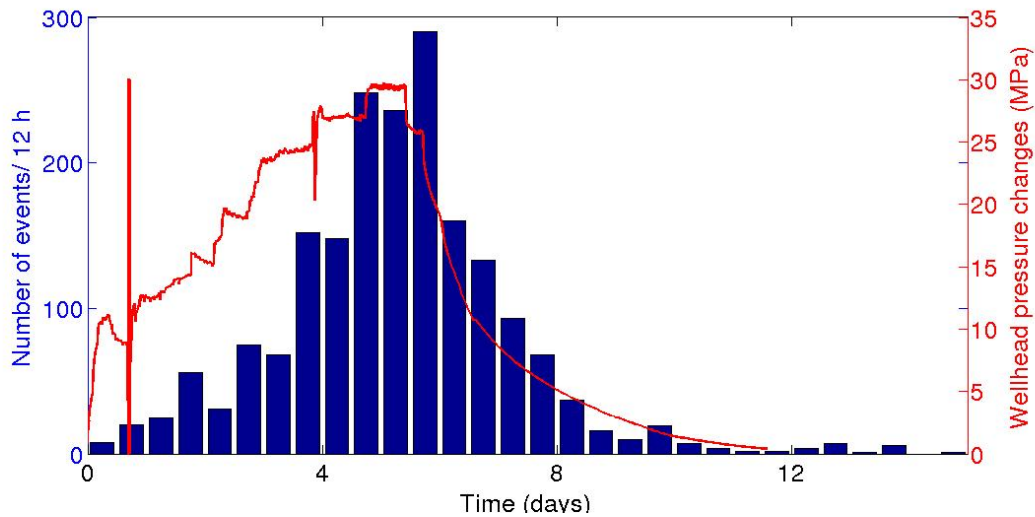
Figure 6.3: Wellhead pressure and number of events of the Basel stimulation.

The seismicity is mainly distributed in a nearly vertical plane centered at 4.5 km depth with an azimuth of 155° (Figure 6.8) in accordance with the regional stress field that is mainly characterized by strike-slip regime with the maximum horizontal stress oriented NW (Häring et al., 2008, and references therein). A precise computation of the orientation of the principal stress components was performed by Valley and Evans (2009) which found a mean orientation of maximum horizontal stress of 144±14° and a minimum horizontal stress of 54±14°

(a)

(b)
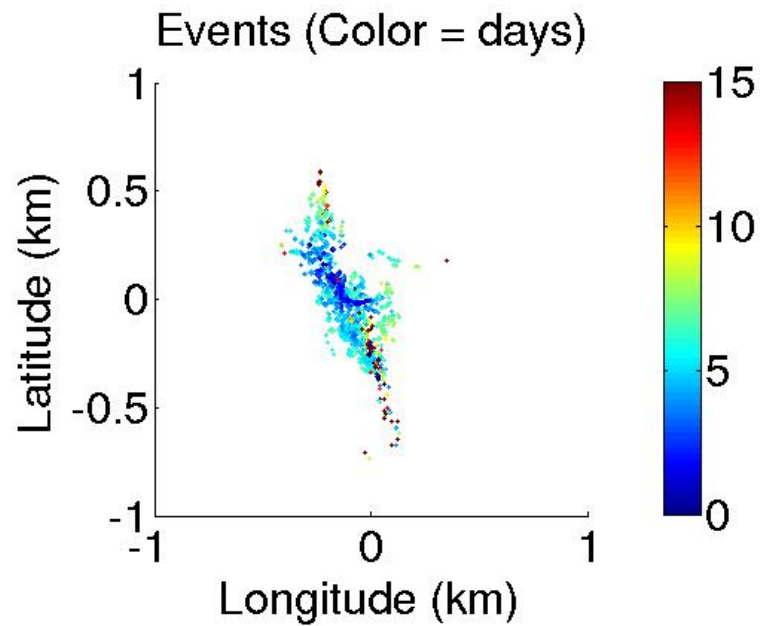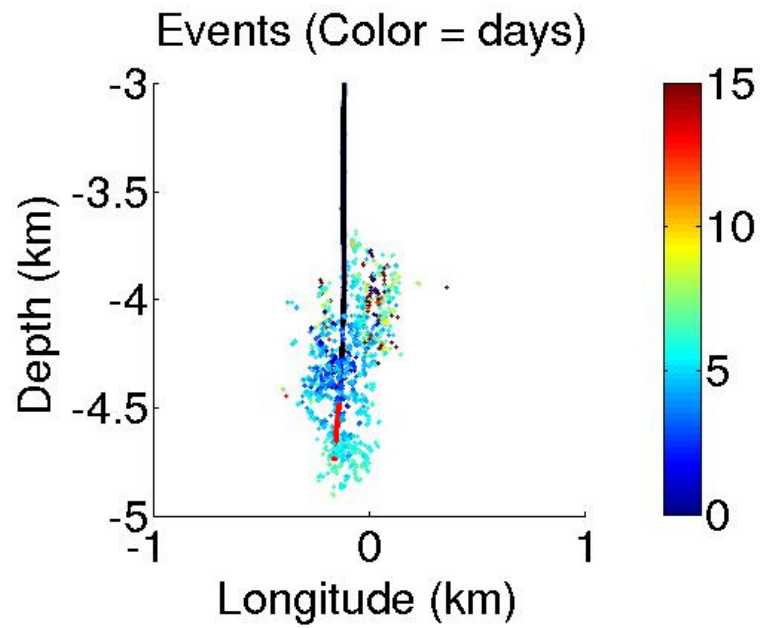
Figure 6.4: Vertical (a) and horizontal (b) view of the induced seismicity during and after the Basel stimulation. Color represent the time of the events. The black line represents the closed section of the well, the red line is the open section of the well.

6.1 An improved stress transfer mechanism

The static stress transfer mechanism due to earthquake interaction is well known to influence the seismicity in tectonic regime (Steacy et al., 2005, and references therein) and its effects on the induced seismicity should be considered together with pore pressure effects (Catalli et al., 2013). Although the TOUGH2-Seed model (Nespoli et al., 2015a) accounts for a static stress transfer mechanisms, as proposed by Baisch et al. (2010), the model is here improved. In this new version I included a more sophisticated formulation of the stress transfer, based on a 3D calculation of the Coulomb stress changes. After an event, a subroutine computes the effective radius of rupture for a circular fault:

$$R = \left(\frac{7M_0}{16\Delta\tau} \right)^{1/3} \tag{6.1}$$

and for all seeds located at a distance r>R from the triggered seed, the program computes the shear τ and the normal stress σ_n changes using the Okada's equations (Okada, 1992). This method allows to consider both positive and negative stress changes depending on the relative position of receiving and source seeds according to the Coulomb stress change theory and also considers far field interactions between seeds.

6.2 Representing the Basel injection

The model domain is a cube with 4 km edge, representing a system that extends from 2000 to 6000 m depth. The domain is initially water saturated and all boundaries have fixed hydrostatic and geothermal conditions. The 3D mesh has a total of 20425 elements and it is finer in the center of the domain. The material is homogeneous over the entire domain with an initial permeability $1 \cdot 10^{-17} m^2$, in accordance with Häring et al. (2008). We simulated the injection well as composed by a cased and an open section, which is open to the horizontal fluid flow and can communicate with the other cells of the computational domain (Figure 6.5).
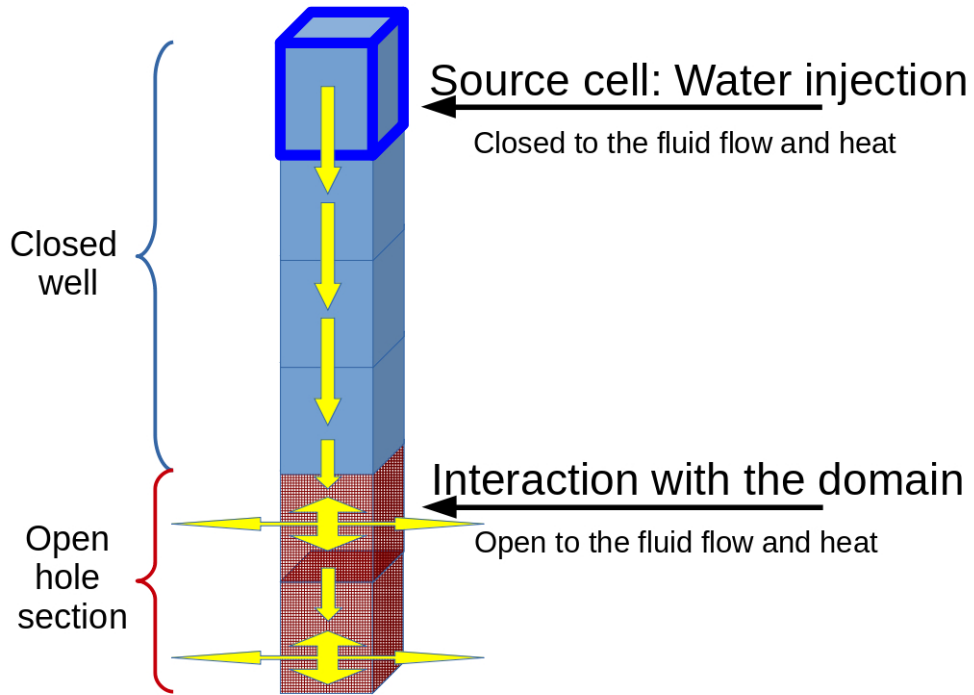
Figure 6.5: Scheme of the simulated well.

A water source is placed at the top cell of the well and its injection rate evolution closely follows the Basel stimulation. Seeds are distributed randomly over the entire domains, with a larger density in a vertical square box of 3 km x 3 km with a width of 100 m. Such a box is oriented with the same azimuth (155 °) of the seismicity cloud observed at Basel. This distribution allows taking into account the anisotropy of the geological setting due to presence of natural fractures mainly oriented NW-SE and NNW-SSE of the Basel subsoil (Häring et al., 2008) which can foster the propagation of the seismic activity along a preferential direction. The parameters of the seed model are listed in Table 1 and reflect the best choice for fitting the data. Thanks to the capability of our model we can represent a realistic oriented 3D regional stress field. In our simulation the orientation of the maximum and minimum stress components of the stress field is given according to Valley and Evans (2009) while the medium magnitude of the three principal stress components is assigned as $\sigma_{Max} \approx 1.6P_{lit}$ (compressive), $\sigma_{med} = \sigma_z \approx P_{lit}$, $\sigma_{min} \approx 0.61P_{lit}$ (see Table 6.1). Each seed represents a fault with strike

Table 6.1: List of constant parameters used in the simulation.

Parameter	Value
Thermal expansion (β)	$3 \cdot 10^{-5} \; °C^{-1}$
Shear modulus (G)	5 GPa
Bulk modulus (K)	8.3 GPa
Stress drop coeff. ($\Delta\tau$ coeff)	0.06
Initial porosity (ϕ_0)	0.005
Residual porosity (ϕ_r)	0.001
Initial permeability (k_0)	$10^{-17} \; m^2$
C_1	15
C_2	1.42
α	$10^{-8} \; Pa^{-1}$
Critical slip (d^*)	$2 \cdot 10^{-3} \; m$
Min-Max magnitude	0.85-9
Min-max differential stress for b-value	0-136 MPa
$\sigma_{Max}(-5km)$	Magnitude $\approx$ 196 MPa (160-255 MPa, Häring et al. (2008)) Orientation = 144 °(144 $\pm$ 14 °, Valley and Evans (2009))
$\sigma_{med}(-5km)$	Magnitude $\approx$ 123 MPa ($\approx$ 122 MPa, Häring et al. (2008)) Orientation = Vertical
$\sigma_{min}(-5km)$	Magnitude $\approx$ 75 MPa ($\approx$ 84 MPa, Häring et al. (2008)) Orientation = 54 °(54 $\pm$ 14 °, Valley and Evans (2009))

oriented along the high density seed distribution direction ($\theta = 155$ °) and a dip = 90 °. Although Kraft and Deichmann (2014) showed that this is not the preferential orientation, their analysis was not properly constrained to get a reliable orientation, and only gives indication about the reactivation mechanisms. The values chosen here follow the average orientation of the largest event in the cloud, whose fault plane solution was derived by a cluster analysis (Deichmann et al., 2014).

6.3 Simulation result

Figure 6.6 shows the comparison between the simulated and the measured wellhead pressure evolutions.
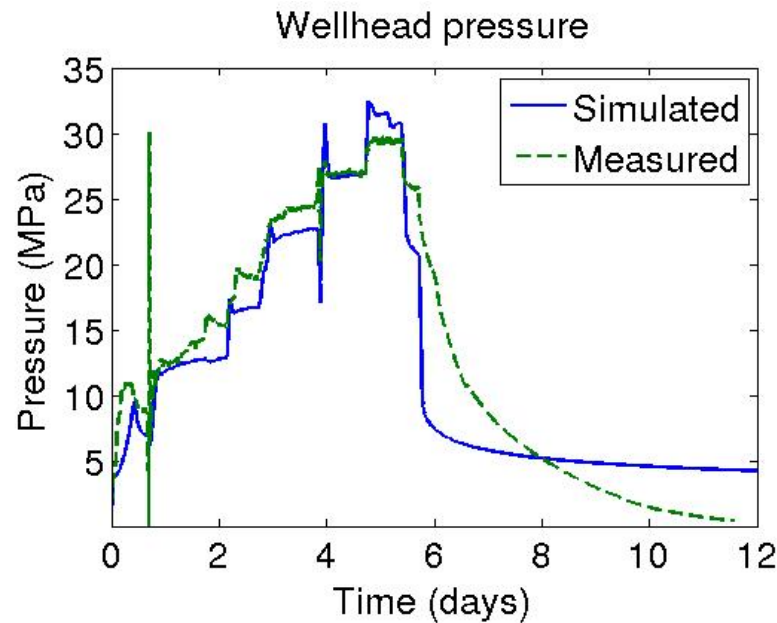
Figure 6.6: Comparison between the measured and the simulated wellhead pressure of the Basel stimulation.

The simulation allows to represent with good approximation the pressure evolution during all the stimulation. The largest differences are found after the shut-in phase (6 days) where the simulated pressure recovery is faster than observed. This effect could be related to the post shutin poro-elastic effects on the rocks that are not simulated in my model. Interestingly, the simulation is able to reproduce the spike that occurred at about 12 hours after the injection. Unlike the subsequent pressure variations this spiked-like change is not due to a change of the injection rate that remained almost constant during the first 12 hours of injection. Performing several tests with different parametrization (not shown) I found that this spike is strongly dependent on the magnitude of the permeability enhancement induced by few events that occur in the first 12 hours, very close to the injection zone. This behavior is a strong evidence that a model of induced seismicity must account for irreversible permeability changes (Gischig and Wiemer, 2013; Goertz-Allmann and Wiemer, 2013).
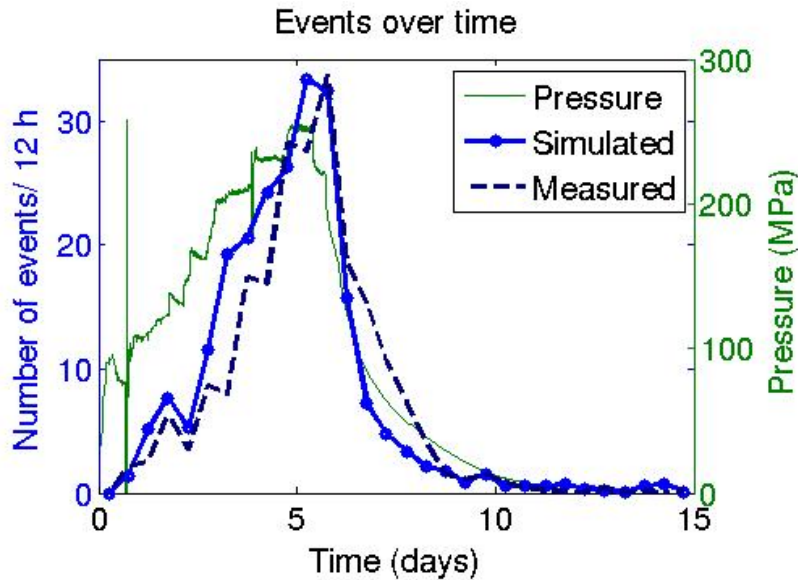
Figure 6.7: Comparison between the measured and the simulated events occurrence over time

Figure 6.7 shows the measured and the simulated temporal distributions of events. Similarly to the real case, the simulation reproduces the increase in seismicity during the whole injection phase reaches a maximum number of events after day 6, just before shut-in when it reaches about 300 events per 12 hours, as in the real case. After the shut-in the number of events rapidly drops following the pressure curve but at the end of the simulations (15 days) few events are still triggered. In the post shut-in phase the pore pressure is lower and the static stress transfer can play a greater role in triggering the induced seismicity after several days or months (Nespoli et al., 2015a). Figure 6.8 plots the magnitude over time for the real (a) and simulated (b) events. The magnitude distribution over time is well represented by our simulation. The events with greater magnitude (M>2) are in both cases focused between 3 and 7 days, with the biggest one at about day 6 (i.e. after shut-in). Both real and simulated catalogues show that few events with magnitude somewhat larger than 2 are still triggered after shut-in (day 6 to 15). The application presented in this chapter shows that a complex model accounting for fluid flow, mechanical effects and changing hydraulic parameters is required to properly reproduce the main characteristic behaviour of induced seismicity in a real case. My model allows to represent a correct initial stress field and allows

to reproduce with sufficient accuracy the temporal events distribution and their magnitude. In all the simulations I showed in chapters 5 and 6 I always used an initial domain with homogeneous hydraulic properties but thanks to the coupling with the TOUGH2 simulator this model can be extended to reproduce hydraulic discontinuities in order to describe also more complex geological settings.
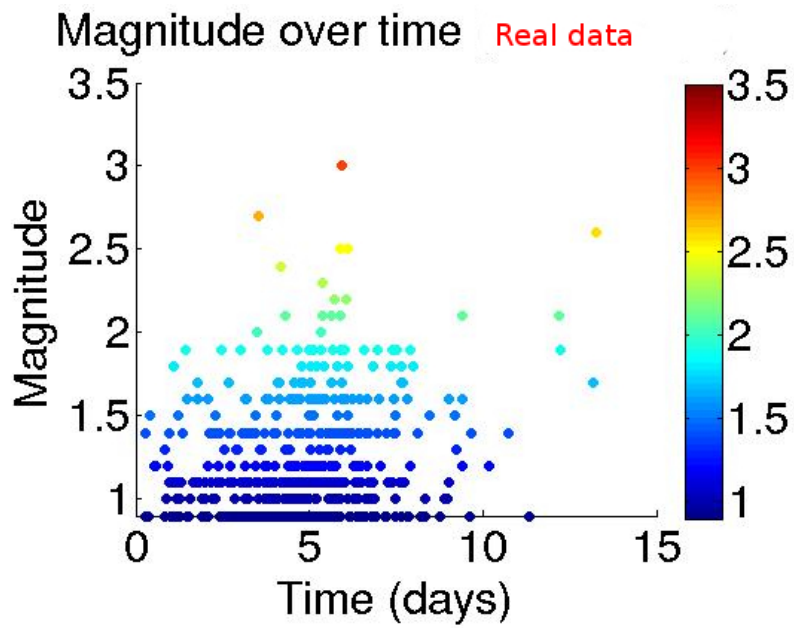
(a)
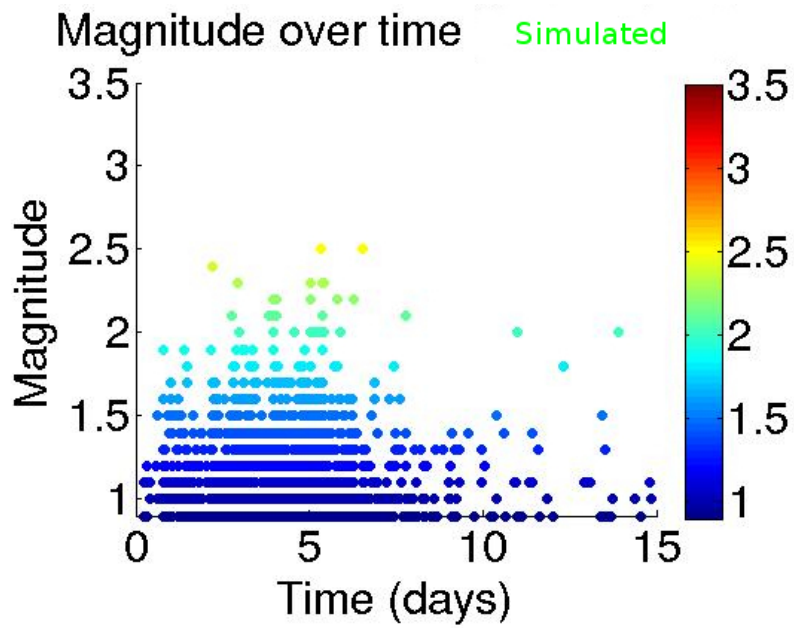
(b)

Figure 6.8: Magnitude of events over time of real data (a) and simulation (b)

CONCLUSIONS

In this thesis I have shown several ways to study and model the earthquake-fluid interaction with the numerical simulator TOUGH2. First, I focused on one of the most evident effects that occurs in porous rocks hit by earthquakes: the water level changes in wells. As discussed in Chapter 2, water level is very sensitive to strain changes and is therefore useful to catch precious information on the subsoil and to study the earthquake effects on fluids. Water level changes can be influenced by both static and dynamic stress changes, mainly depending on the distance from the fault. My study focused on the Emilia Romagna (Italy) seismic sequence and its effects on few wells distributed around the fault of the mainshock, on May 20, 2012. In this case the regional monitoring network measured a clear water level increase in three wells near to the epicenter. To understand this behaviour I modeled the static stress changes induced by the earthquake, starting from the non-uniform fault slip model proposed by Pezzo et al. (2013), which was derived from both InSar and GPS data. The corresponding pore pressure variations were computed following the theory of poroelasticity and accounting for a shallow elastic discontinuity detected from seismic data. All the wells in our case experienced a co-seismic increase of the water level and are located in a compressive zone, according to the computed stress changes. This behaviour suggests that water level changes are driven by static stress change, while the dynamic stress changes seem to have played only a minor role. The static stress change was used to compute the corresponding pore pressure changes, which was applied as a perturbation of the initial hydrostatic state. A porous medium flow model was then used to compute the diffusion of such

pressure perturbation through the shallow stratigraphy. I performed several simulations changing the hydraulic properties (permeability and porosity) of the different layers of the model. I found that the presence of the hydraulic discontinuities is very important for the whole pressure diffusion process and cannot be neglected: the rate of recovery of the water level strongly depends on both the permeability contrast between the layers and the permeability of each aquifer. To improve the fit between the measured and the computed water level evolutions I had to consider also two secondary effects: the meteoric recharge and the soil compaction in the shallowest layer. The soil compaction, in particular, allows to justify the small differences observed in nearby wells, which are difficult to ascribe to different values of stress change. Different degrees of the soil compaction can occur over short distances and the occurrence of this phenomenon is well supported by the evidence of localized soil liquefaction in the area.

In Chapter 4 I focused on an anomalous and localized soil heating observed in the same region. The high temperatures of the soil measured here (up to 50 °C) are always accompanied with small seepage of methane. This behaviour was also present in the past, as confirmed by several historical sources, but the mechanism behind this phenomenon was never clarified. The interest in this phenomenon has grown after the seismic sequence in 2012, but there was no clear evidence of a relationship with the seismicity. The aim of my study was to understand the physical mechanism that cause shallow heating in this area. Based on the results, I also drew some considerations on the possible interactions with seismicity. I started from the data and conceptual model proposed by Capaccioni et al. (2015). These authors measured gas fluxes, concentrations and temperature and suggested that shallow heating is due to an exothermic oxidation of the methane rising from a slightly deeper peat layer. This reaction is performed by metanotrophic bacteria as revealed from biological survey. Based on the reconstructed shallow stratigraphy, I generated a 2D computational domain with the TOUGH2 simulator. I simulated a constant injection of methane from the bottom of the domain that is fully water saturated below 2 m depth. The survey showed that the maximum temperature is achieved at a depth of 0.6 m. Here I placed heat sources that inject heat proportionally to the methane flux entering the cell, and according to the heat production rate associated with the methane oxidation reaction. In this way I was able to simulate the heat produced

by the exothermic methane oxidation reaction. I also considered a periodic temperature boundary condition in the top layer in order to simulate the seasonal effects. The simulations show that the exothermic oxidation of methane is a plausible mechanism to explain the anomalous soil heating. Then I compared the position of the survey area with the stress changes map due to the Emilia earthquake computed in the previous chapter and I found that all the area is in a compressive zone and we cannot exclude that the earthquake could have increased the methane seepage and consequently the soil heating. In any case this phenomenon always occurs regardless from the seismicity.

In Chapter 5 I discussed a model to study the seismicity induced by geothermal activity. This model is obtained by coupling the TOUGH2 simulator with an improved version of the stochastic seed model proposed by Gischig and Wiemer (2013). The coupling was performed linking the two codes of the models so that the thermodynamic variables of the fluid computed by TOUGH2 (Pore pressure, Temperature) are used from the seed model to apply the Mohr-Coulomb failure criterion in each seed. The seed model also computes the reversible permeability changes due to pore pressure variations and the irreversible permeability increase due to seismic shaking. These permeability changes are fed to the TOUGH2 simulator assuring a full coupling of both thermodynamic and hydraulic parameters. The TOUGH2 simulator cannot (well) represent the mechanical effects of fluid dynamic onto the porous matrix, so all the mechanical effects are computed directly by the seed model that upgrades the stress tensor of each seed on the basis of pressures and temperatures computed by TOUGH2. This coupling also considers the stress transfer mechanism between seeds in order to simulate the mechanical deformation of rocks after an event. In the applications shown in Chapter 5, I simulated an injection of water in a deep reservoir with initial homogeneous hydraulic properties. We have seen that considering a 3D system allows us to simulate the anisotropy of the spatial distribution of activated seeds that had a tear drop shape. When I accounted also for irreversible slip-dependent permeability changes, I obtained a lower number of events over the entire stimulation and a lower well pressure. When also the stress transfer was accounted for, I found that seismicity can follow a general slip-oriented distribution and/or produce several fringes of seismicity at the edge of the seismic cloud. The stress transfer was very important also in the temporal

distribution of the events because in this case there were a lot of events even in the later stage of injection and in the post shut-in phase.

Chapter 6 shows an application of the coupled model described in the previous chapter. Here I included a more complex and realistic stress transfer mechanism that follows Okada's dislocation solutions in order to consider large scale seeds interactions. In this chapter I show a data fit with the Basel's geothermal stimulation experiment, focusing on the representation of the wellhead pressure, temporal and magnitude distribution of the seismic events. I found that the coupled model is capable of representing the main characteristics of a real case of injection. The computation of permeability changes is very important in this case, since without considering them I was never able to reproduce the wellhead pressure evolution.

In these 6 chapters I have shown some models that can reproduce the main characteristics of the fluid-earthquakes interaction. The improvements and further applications of these models could lead other information about this complex topic. For example, it might be interesting to improve these models to account for dynamic stress effects or investigate areas with a more complex distribution of fluid phases with higher temperatures, like volcanic areas: here a fluid pressure change could lead to a phase change of the fluid. Also, in the case of the geothermal stimulation, it might be interesting to apply the coupling model to more complex geology or to study hydrofracking problems.

Appendices

LA: TOUGH2 TIME AND SPACE DISCRETIZATION

The equations described in the previous section must be discretized in time and space. The TOUGH2 simulator uses the integral finite difference method (Edwards, 1972; Narasimhan and Witherspoon, 1976), following the geometry shown in Figure 9 . Equation (1.14) must be rewritten as

$$\int_{V_n} MdV = V_n M_n \tag{2}$$

where M_n is the average value of M in the volume V_n. Also the flux equations must be written as discrete sum over surface segments A_{nm}:

$$\int_{\Gamma_n} F^c \cdot \mathbf{n} d\Gamma = \sum_m A_{nm} F_{nm} \tag{3}$$

In this case F_{nm} is the average value the vector F over the area A_{nm} between two cells of volume V_n and V_m. Because of this discretization, the Darcy flux of phase β has to be written as (4).

$$F_{\beta,nm} = -k_{\beta,nm} \left[\frac{k_{r,\beta}\rho_\beta}{\mu_\beta} \right]_{nm} \left[\frac{p_{\beta,n} - p_{\beta,m}}{D_{nm}} - \rho_{\beta,nm} g_{nm} \right] \tag{4}$$

$D_{nm} = D_n + D_m$ is the distance between the nodal points of elements like in Figure 9. The spatial discretized equations become a set of differential equations:

$$\frac{dM_n^c}{dt} = \frac{1}{V_n} \sum_m A_{nm} F_{nm}^c + q_n^c \tag{5}$$
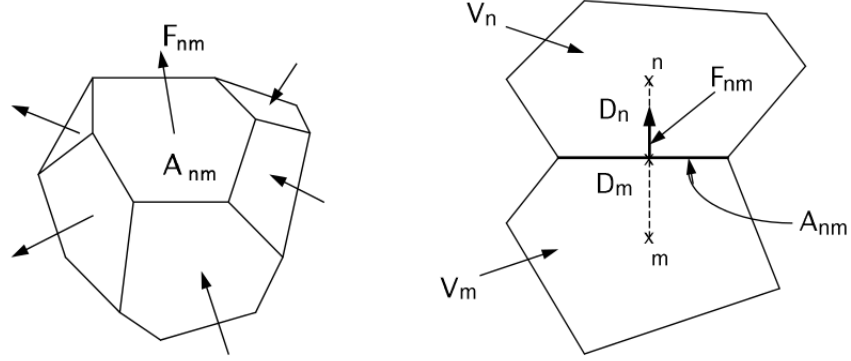
Figure 9: Scheme of TOUGH2 space discretization

The time is discretized with a fully implicit calculation so the variables are updated at time $t^{j+1} = t^j + \Delta t$ and with a first order finite difference method (Peaceman, 1977). The time discretization results in the following equations of residuals $R_n^{c,k+1}$:

$$R_n^{c,k+1} = M_n^{c,k+1} - M_n^{c,k} - \frac{\Delta t}{V_n} \{ \sum_m A_{nm} F_{nm}^{c,k+1} + V_n q_n^{c,k+1} \} = 0 \qquad (6)$$

This means that for a model with a number of cell = NCEL the state of the system is completely defined by NCEL x (NC+1) equations solved with the Newton-Raphson method. Calling d the iteration index that leads to an increment $x_{i,d+1} - x_{i,d}$ we can expand with a Taylor series the equation

$$R_n^{c,k+1}(x_{i,d+1}) = R_n^{c,k+1}(x_{i,d}) + \left(\sum_i \frac{\partial R_n^{c,k+1}}{\partial x_i} \right)_d (x_{i,d+1} - x_{i,d}) + ... = 0 \quad (7)$$

Catching only the first order terms we obtain the new set of shorter equations

$$R_n^{c,k+1}(x_{i,d}) = - \left(\sum_i \frac{\partial R_n^{c,k+1}}{\partial x_i} \right)_d (x_{i,d+1} - x_{i,d}) \qquad (8)$$

Convergence criterion

Equations 8 can be solved using several methods (Moridis and Pruess, 1995, 1998; Duff, 1977) and the iterations continue until the residual is lower than

the tolerance ϵ_r (relative convergence criterion).

$$\left|\frac{R_{n,d+1}^{c,k+1}}{M_{n,d+1}^{c,k+1}}\right| \leq \epsilon \tag{9}$$

If accumulation terms are smaller than ϵ_a also an absolute convergence criterion is imposed.

$$|R_{n,d+1}^{c,k+1}| \leq \epsilon_a \cdot \epsilon_r \tag{10}$$

Normally with the default values of $\epsilon_r = 10^{-5}$ and $\epsilon_a = 1$ the convergence is achieved in few iterations. If the simulation does not reach the convergence after few iterations, the time step is reduced. Obviously the convergence is easier to find in simulations with realistic and well defined initial and boundary conditions.

A: TOUGH2 time and space discretization

Test 1

To study the influence of the large aspect ratio of the cells in the computational mesh used in Chapter 3, I performed several test. In the first group of tests I generated a computational domain 14x14 km wide and 200 m deep and I performed 3 different simulations changing the horizontal dimensions of the cells from 4x4 km to 0.5x0.5 km. All cells are 2 m deep. The domain is initially water saturated and hydrostatic. All boundaries are open. An overpressure was applied in centre of the system (x = y = 0), at all depths.
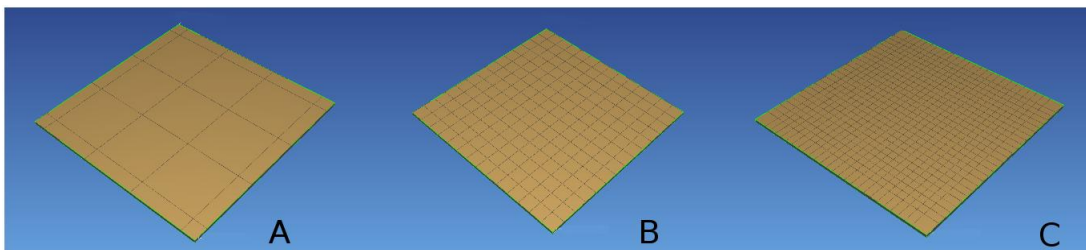
Figure 10: Test on the extreme cells aspect ratio in the computational mesh. I performed 3 different cases with different horizontal dimension of elements (a) 4 x 4 km, (b) 1 x 1 km, (c) 0.5 x 0.5 km.
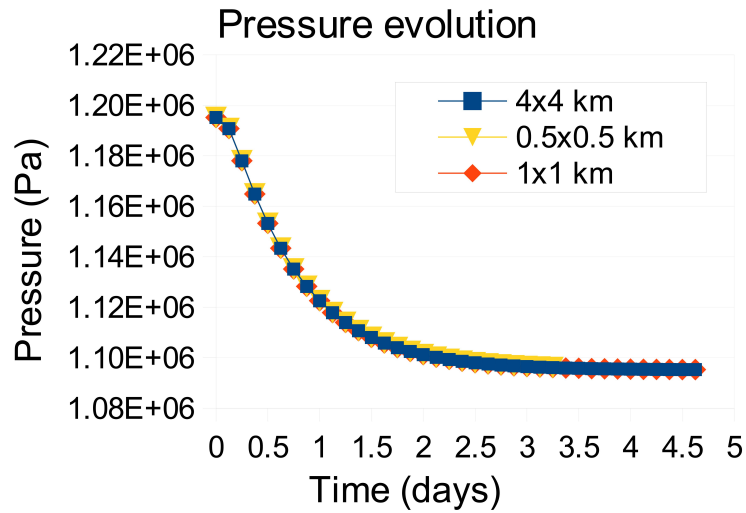
Figure 11: Pressure (Pa) evolution through time (days), x=y=0; z=-101 m
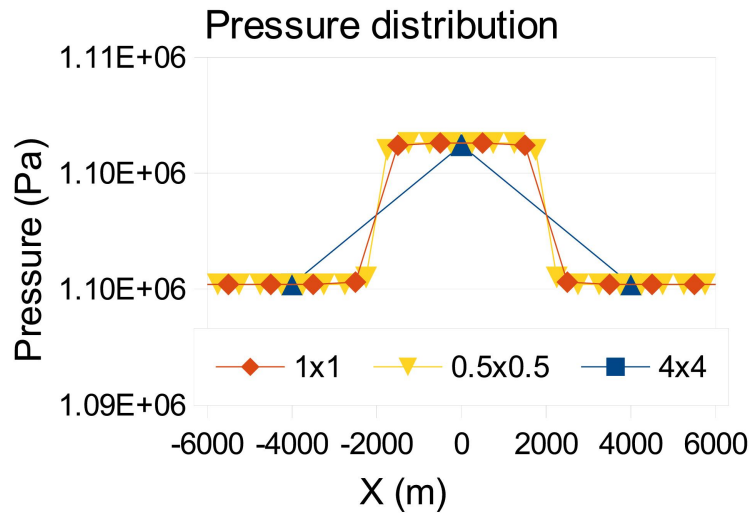
Figure 12: Pressure (Pa) distribution along the X axis (m), z=-110 m, after 2 days of simulation.

Test 2

In the second group of tests I generated a 2x2 km domain 100 m deep. I performed 3 different cases with different horizontal dimension of elements (from 200x200 m to 50x50 m). Also in these cases an overpressure was applied

in centre of the system (x = y = 0), at all depths. All boundaries are open and the domain is initially water saturated and hydrostatic.
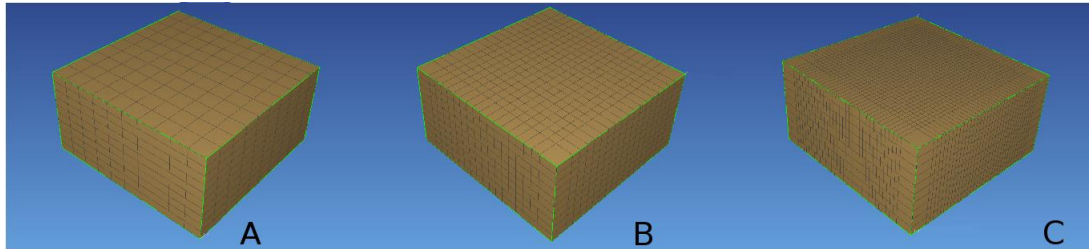
Figure 13: Test on spatial resolution of the computational mesh. I performed 3 different cases with different horizontal dimension of elements. (a) 200 x 200 m, (b) 100 x 100 m, (c) 50 x 50 m.
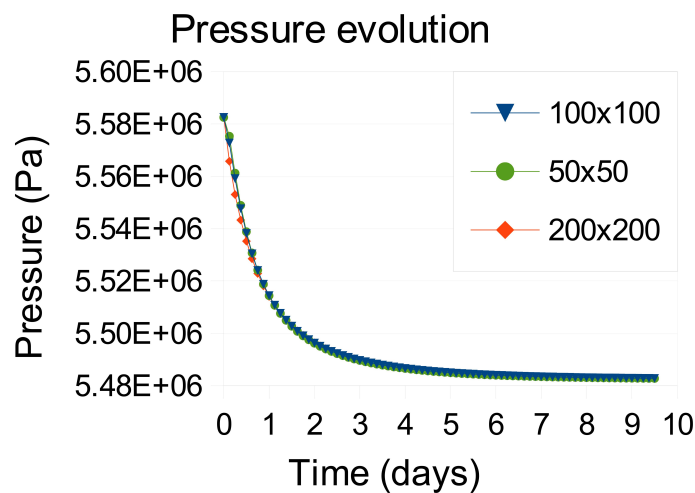
Figure 14: Pressure (Pa) evolution through time (days), x=y=0; z=-550 m.
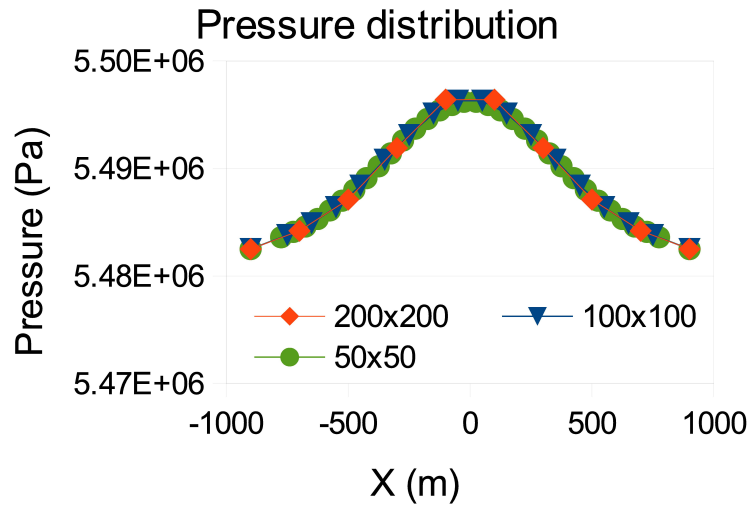
Figure 15: Pressure (Pa) distribution along the X axis (m), z=-550 m, after 2 days of simulation.

Bottom boundary effect

To study the influence of the bottom boundary I performed another simulation with a deeper domain (-700 m), starting from Case 4. Figure 17 shows the two computational domain used for this test.
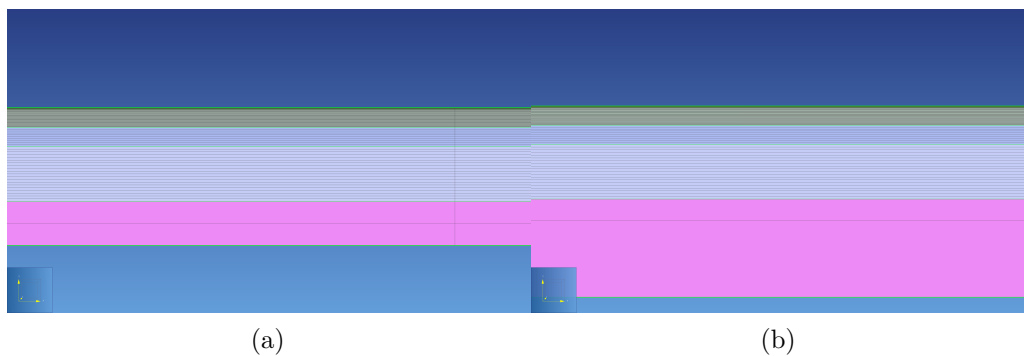
Figure 16: Vertical view of the computational domains used (a) in the base cases simulations (-500 m) and (b) in the test to study the boundary effect (-700 m)
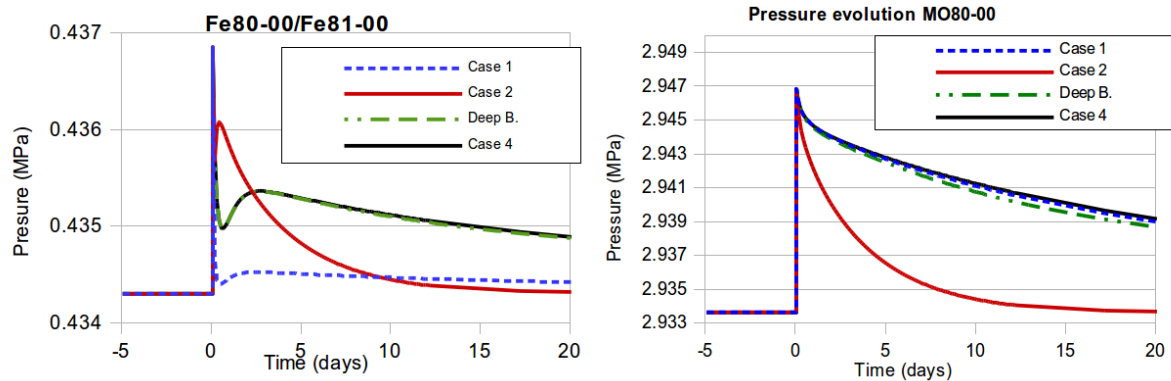
Figure 17: Comparisons between well pressure of base cases and the case with a deeper bottom boundary (a) shallow wells, (b) deep well

Results

On the one hand the great vertical resolution of the mesh used in the Chapter 3 allows to capture the small pressure variations in the vertical direction, in order to simulate a precise value of bottomholes pressure. On the other hand the larger horizontal cells dimensions are sufficient to represent the stress field, that varies on large spatial scales. All tests show that the diffusion process is not influenced by the discretization resolution. Time and space evolutions of pore pressure are the same in all the cases of Test 1 and Test 2. This means that the simulation I performed are not sensibly influenced by the cell dimension choice and no large bias are introduced.

Table 2: Depth, coordinates and distance from 20 May 2012 epicenter of the 40 wells of the network

Well	Depth (m) (m)	Latitude (gg.dddddd)	Longitude (gg.dddddd)	Distance to epicenter (km)
BO20-00	131	44.51548488	11.26721321	41.62
BO28-00	67	44.55840621	11.37351344	38.51
BO49-00	193	44.49842897	11.31455011	43.94
BO55-01	84	44.47901421	11.47104547	49.47
BOF8-00	60	44.51757465	11.30221038	41.69
BOF9-00	200	44.68330915	11.2814521	23.25
BOG0-00	183.5	44.35956169	11.74259339	71.62
FC14-02	170.3	44.21171648	12.11132932	102.93
FC16-01	218	44.16666339	12.44165538	125.53
FC20-00	108.5	44.22482655	12.02317034	97.17
FC83-01	90.6	44.20072104	12.06119357	101.18
FC90-00	125	44.14693624	12.22443526	114.37
FE75-00	30	44.8602666	11.83261552	47.89
FE80-00	40	44.9464043	11.28081503	7.62
FE81-00	40	44.93866056	11.31711108	8.94
MO08-00	256	44.82011129	11.11523489	11.75

C: Regional network of wells

Well	Depth (m) (m)	Latitude (gg.dddddd)	Longitude (gg.dddddd)	Distance to epicenter (km)
MO43-01	148	44.79181955	11.13449087	13.09
MO48-01	224	44.85375016	11.23661736	3.98
MO64-00	73	44.52912392	11.06369232	42.06
MO72-01	104	44.58855247	10.86132416	44.25
MO80-00	300	44.88130241	11.07821382	11.86
MO81-00	116	44.57248601	10.79600243	49.07
PC27-02	120	44.92700362	9.89474685	105.36
PC56-03	94	45.051607	9.65608761	125.29
PC96-00	80	44.99069341	9.73427147	118.41
PR23-02	166	44.86724681	10.21458591	80.1
PR32-00	109	44.78125514	10.32198637	72.62
PRB3-00	110	44.82654851	10.18290363	82.88
PRB4-00	45	44.84457873	10.15215814	85.15
RA34-02	120	44.38228549	12.19214977	95.01
RA58-00	460	44.46849367	11.96112	74.59
RE15-00	170	44.8240315	10.75434144	38.13
RE25-00	160	44.71979219	10.51722579	59.29
RE55-00	150	44.696126	10.60988933	53.4
RE79-01	60	44.6531867	10.47312445	65.24
RN02-00	36.5	43.964388	12.709194	156.47
RN03-00	28	44.03228494	12.4603134	136.71
RN04-00	50	44.06283107	12.55287263	139.82
RN05-00	96	44.0678851	12.50062182	136.33
RN06-00	34.7	43.967479	12.716267	156.67

D: VARIABLES AND PARAMETERS

Table 3: List of variable and parameters used in this thesis

Symbol	Variable	Unit of measurement
$\mathbf{q}$	Darcy velocity	m/s
K_H	Hydraulic conductivity	m/s
p	Pore pressure	Pa
ρ	Density	kg/m^3
g	Gravitational acceleration	m/s^2
k	Permeability	m^2
k_r	Relative permeability	—
k_β	Effective permeability of phase β	m^2
μ	Viscosity	$Pa \cdot s$
v	Speed	m/s
ϕ	Porosity	—
S	Fluid saturation	—
X	Mass fraction	—
$\tau_0 \tau_\beta$	Tortuosity	—
d_β^c	molecular diffusion coefficient	m^3/s
q^c	Mass sink or source	kg/s
T	Temperature	°C
λ	Thermal conductivity	$W/(m \cdot K)$
u	Enthalpy	J
h	Internal energy	J
c	Specific heat	$J/(kg \cdot K)$
ϵ_{ij}	Strain tensor	—
σ_{ij}	Stress tensor	Pa

Table 4: List of variable and parameters used in this thesis

Symbol	Variable	Unit of measurement
G	Rigidity	Pa
ν	Drained Poisson modulus	$-$
ν_u	Undrained Poisson modulus	$-$
H	Biot's constant	Pa
K	Compressibility	Pa
K_u	Undrained compressibility	Pa
E	Young's modulus	Pa
m	Mass	Kg
A	Wave amplitude	m
f	Wave frequency	s^{-1}
γ	Pressure sensitivity	Pa^{-1}
α_s	Porosity sensitivity	$-$
T_i	Particle period of i-th mode	s
e	Energy density	J/m^3
M	Magnitude	$-$
r	Distance	m
τ	Tangential stress	Pa
σ_n	Normal stress	Pa
μ_f	Friction	$-$
Γ	Friction angle	Degrees
V_s	Shear wave velocity	m/s
B	Skempton's coefficient	$-$
Δh	Water level change	m
R_s	Ratio of oxidized methane in summer	$-$
R_v	Ratio of oxidized methane in winter	$-$
β	Volumetric thermal expansion coefficient	$°C^{-1}$
C	Cohesion	Pa
d	Fault slip	m
M_0	Seismic moment	$N \cdot m$

D: Variables and parameters

BIBLIOGRAPHY

Akita, F. and Matsumoto, N. (2004). Hydrological responses induced by the tokachi-oki earthquake in 2003 at hot spring well in hokkaido, japan. *Geophysical Research Letters 31.* doi:10.1029/2004GL020433.

Amorosi, A., Farina, M., Severi, P., Preti, D., Caporale, L., and Dio, G. D. (1996). Genetically related alluvial deposits across active fault zones: an example of alluvial fan-terrace correlation from the upper quaternary of the southern po basin, italy. *Sedimentary Geology, 102(3-4), 275–295.* doi:10.1016/0037-0738(95)00074-7.

Bachmann, C., Wiemer, S., Goertz-Allmann, B., and Woessner, J. (2012). Influence of pore-pressure on the event-size distribution of induced earthquake. *Geophys. Res. Lett., 40(1),72-77.*

Bachmann, C., Wiemer, S., Woessner, J., and Hainzl, S. (2011). Statistical analysis of the induced basel 2006 earthquake sequence: introducing a probability-based approach for ehnhancedgeothermal system. *Geophysic. J. Int., 186, 793-807.*

Bachmat, Y. (1964). The general equations of hydrodynamic dispersion in homogeneous, isotropic, porous mediums. *JOURNAL OF GEOPHYSICAL RESEARCH VOL. 69, NO. 12.*

Baisch, S., Vörös, R., Rother, E., Stang, H., Jung, R., and Schellschmidt,

Bibliography

R. (2010). A numerical model for fluid injection induced seismicity at soultz-sous-forêts. *Int. J. Rock Mech. Min. Sc., 47(3), 405-413.*

Bilek, S. L. and Ruff, L. (2002). Analysis of the 23 june 2001 mw = 8.4 peru underthrusting earthquake and its aftershocks. *Geophysical Research Letters*, 29(20):21–1–21–4. 1960.

Biot, M. (1941). General theory of three-dimensional consolidation. *Journal of Applied Physics 12: 155-164.*

Bonori, O., Ciabatti, M., Cremonini, S., Giovanbattista, R. D., Martinelli, G., Maurizzi, S., and Zantedeschi, E. (2000). Geochemical and geophysical monitoring in tectonically active areas of the po valley (northern italy). case histories linked to gas emission structures. *Geogr. Fis. Dinam. Quat., 23(2000), 3-20.*

Bordoni, P., Azzara, R., Cara, F., Cogliano, R., Cultrera, G., Giulio, G. D., Fodarella, A., Milana, G., Pucillo, S., Riccio, G., Rovelli, A., Augliera, P., Luzi, L., Lovati, S., Massa, M., Pacor, F., Puglia, R., and Ameri, G. (2012). Preliminary results from emersito, a rapid response network for site-effect studies. *Annals Of Geophysics, 55(4).* doi:10.4401/ag-6153.

Borgia, A., Pruess, K., Kneafsey, T. J., and Oldenburg, C. M. (2011). Using tough2/eco2h for modeling high-pressure and high-temperature co2-enhanced geothermal energy extraction from saline systems. *American Geophysical Union, Fall Meeting 2011, abstract IN33C-1473.*

Brodsky, E., Roeloffs, E., Woodcock, D., Gall, I., and Manga, M. (2003). A mechanism for sustained groundwater pressure changes induced by distant earthquakes. *J. Geophys. Res., 108(B8), 2390, doi:10.1029/2002JB002321.*

Brown, G. O. (2002). Henry darcy and the making of a law. *WATER RESOURCES RESEARCH, VOL. 38, NO. 7, 1106.* doi:10.1029/2001WR000727.

Cao, W. and Zhang, S. (2005). Study on the statistical analysis of rock damage based on mohr-coulomb criterion. *Journal of Hunan University (Natural Science), 2005-01.*

Capaccioni, B., Tassi, F., Cremonini, S., Sciarra, A., and Vaselli, O. (2015). Ground heating and methane oxidation processes at shallow depth in terre

calde di medolla (italy): Observations and conceptual model. *J. Geophys. Res. Solid Earth, 120.* doi:10.1002/2014JB011635.

Catalli, F., Meier, M., and Wiemer, S. (2013). The role of coulomb stress changes for injection-induced seismicity: The basel enhanced geothermal system. *Geophys. Res. Lett., 40(1),72-77.*

Cesca, S., Braun, T., Maccaferri, F., Passarelli, L., Rivalta, E., and Dahm, T. (2013). Source modelling of the m5–6 emilia-romagna, italy, earthquakes (2012 may 20-29). *Geophysical Journal International, 193, 1658–1672.* doi:10.1093/gji/ggt069.

Chanton, J. and Liptay, K. (2000). Seasonal variation in methane oxidation in a landfill cover soil as determined by an in situ stable isotope technique. *Global Biogeochem. Cycles, 14, 51-60.* doi:10.1029/1999GB900087.

Chin, L. Y., Raghavan, R., and Thomas, L. (2001). Fully-coupled geomechanics and fluid-flow analysis of wells with stress-dependent permeability. *SPE J. 5, 32-45.*

Cocco, M., Ardizzoni, F., Azzara, R., Dall'Olio, L., Delladio, A., Bona, M. D., Malagnini, L., Margheriti, L., and Nardi, A. (2001). Broadband waveforms and site effects at a borehole seismometer in the po alluvial basin (italy). *Annals Of Geophysics, 44(1).* doi:10.4401/ag-3611.

Convertito, V., Catalli, F., and Emolo, A. (2013). Combining stress transfer and source directivity: the case of the 2012 emilia seismic sequence. *Scientific Reports |3:3114 |.* doi: 10.1038/srep03114.

Cooper, H., Bredehoeft, J., Papadopulos, I., and Bennett, R. (1965). The response of well-aquifer systems to seismic waves. *Journal of Geophysical Research 70: 3915-3926.*

Cremonini, S. (2010). Scan subaerial pockmarks exist?, international workshop: I sinkholes. gli sprofondamenti catastrofici nell'ambiente naturale ed, in quello antropizzato. *(Roma, 3-4 Dicembre 2009), pp. 29-34, ISPRA, Roma.*

Dando, P., Hughes, J., Leahy, Y., Taylor, L., and Zivanovic, S. (1994). Earthquakes increase hydrothermal venting and nutrient inputs into the aegean. *Continental ShelfResearch, Vol. 15, No. 6, pp. 655-66.*

Bibliography

David, C., Wong, T., Zhu, W., and Zhang, J. (1994). Laboratory measurements of compaction-induced permeability change in porous rocks: Implication for generation and maintenance of pore pressure excess in the crust. *Pure and Applied Geophysics, v. v.143pp.425-456.*

Deichmann, N., Kraft, T., and Evans, K. F. (2014). Identification of faults activated during the stimulation of the basel geothermal project from cluster analysis and focal mechanisms of the larger magnitude events. *Geothermics*, 52:84 – 97. Analysis of Induced Seismicity in Geothermal Operations.

Dublanchet, P., Bernard, P., and Favreau, P. (2013). Interactions and triggering in a 3-d rate-and-state asperity model. *J. Geophys. Res. - Solid Earth, 118(5), 2225-2245.*

Duff, I. S. (1977). A set of fortran subroutines for sparse unsymmetric linear equations. *AERE Harwell Report R 8730, 1977.*

Dunfield, P. F. et al. (2007). Methane oxidation by an extremely acidophilic bacterium of the phylum verrucomicrobia. *Nature, 450(7171),879-882.* doi:10.1038/nature06411.

Edwards, A. L. (1972). Trump: A computer program for transient and steady state temperature distribution in multidimensional systems. *National Technical Information Service, National Bureau of Standards, Springfield, VA.*

Elkhoury, J., Brodsky, E., and Agnew, D. (2006). Seismic waves increase permeability. *Nature, 441(7097) pp. 1135-1138.*

Ellsworth, W. (2013). Injection-induced earthquakes. *Science, 341.*

Emergeo-Working-Group (2012). Technologies and new approaches used by the ingv emergeo working group for real-time data sourcing and processing during the emilia romagna (northern italy) 2012 earthquake sequence. *ANNALS OF GEOPHYSICS, 55, 4, p. 689-695, 2012.* doi: 10.4401/ag-6117.

Esha, D. W. and Benedicta, R. W. (1996). Thermal/hydrological modeling of the radioactive scrap and waste facility (rswf) with the tough2 (transport of unsaturated groundwater and heat) code. *MRS Proceedings / Volume 465 / 1996. DOI: http://dx.doi.org/10.1557/PROC-465-1109.*

Evans, J. P. (1997). Permeability of fault- related rocks, and implications for hydraulic structure of fault zones. *JOURNAL OF STRUCTURAL GEOLOGY.* 10.1016/S0191-8141(97)00057-6.

Finsterle, S. (1999). Itough2 user's guide. *Report LBNL-40040, Lawrence Berkeley National Laboratory, Berkeley, Calif.*

Fischer, D., Mogollón, J. M., Strasser, M., Pape, T., Bohrmann, G., Fekete, N., Spiess, V., and Kasten, S. (2013). Subduction zone earthquake as potential trigger of submarine hydrocarbon seepage. *Nature Geoscience.* doi:10.1038/ngeo1886.

Floodgate, G. and Judd, A. (1992). The origins of shallow gas. *Cont. Shelf Res., 12, 1145-1156.*

Fournier, N. and Chardot, L. (2012). Understanding volcano hydrothermal unrest from geodetic observations: Insights from numerical modeling and application to white island volcano, new zealand. *J. Geophys. Res., 117, B11208.* doi:10.1029/2012JB009469.

Ge, S. and Stover, S. (2000). Hydrodynamic response to strike- and dip-slip faulting in a half-space. *Journal of Geophysical Research, 105(B11), 25513 - 25524.*

Gennes, P. G. D. (1983). Hydrodynamic dispersion in unsaturated porous media. *Journal of Fluid Mechanics / Volume 136 / November 1983, pp 189- 200.* Cambridge University Press, DOI: http://dx.doi.org/10.1017/S0022112083002116.

Gischig, V. and Wiemer, S. (2013). A stochastic model for induced seismicity based on non-linear pressure diffusion and irreversible permeability enhancement. *Geophys. J. Int., 194(2), 1229-1249.*

Gischig, V., Wiemers, S., and Alcolea, A. (2014). Balancing reservoir creation and seismic hazard in enhanced geothermal system. *Geophys. J. Int., 198, 1585-1598.*

Goertz-Allmann, B. and Wiemer, S. (2013). Geomechanical modeling of induced seismicity source parameters and implications for seismic hazard assessment. *Geophysics, 78(1), KS25- KS39.*

Bibliography

Gomberg, J., Bodin, P., Larson, K., and Dragert, H. (2004). Earthquake nucleation by transient deformations caused by the m = 7.9 denali, alaska, earthquake. *Nature 427, 621-624.* doi:10.1038/nature02335.

Grecksch, G., Roth, F., and Kümpel, H. (1999). Coseismic well-level changes due to the 1992 roermond earthquake compared to static deformation of half-space solutions. *Geophys. J. Int. 138, 470-478.*

Grünthal, G. (2013). Induced seismicity related to geothermal projects versus natural tectonic earthquakes and other types of induced seismic events in central europe. *Geothermics.* doi:10.1016/j.geothermics.2013.09.009.

Guglielmi, Y., Cappa, F., Avouac, J., Henry, P., and Elsworth, D. (2015). Seismicity triggered by fluid injection-induced aseismic slip. *Science, 348(6240), 1224-1226.*

Hanson, R. and Hanson, T. (1996). Methanotrophic bacteria,. *Microbiol. Rev., 60, 439-471.*

Hao, J., Chen, J., Wang, W., and Yao, Z. (2013). Rupture history of the 2013 mw 6.6 lushan earthquake constrained with local strong motion and teleseismic body and surface waves. *Geophysical Research Letters*, 40(202):5371–5376. 2013GL056876.

Häring, M., Schanz, U., Ladner, F., and Dyer, B. (2008). Characterisation of the basel enhanced geothermal system. *Geotherm., 37, 469-495.*

Ioannides, T. and Verykios, X. (1997). Catalytic partial oxidation of methane in a novel heat-integrated wall reactor. *Catal. Lett., 47(3-4), 183.* doi:10.1023/A:1019077626264.

Jasim, A., Whitaker, F. F., and Rust, A. C. (2015). Impact of channelized flow on temperature distribution and fluid flow in restless calderas: Insight from campi flegrei caldera, italy. *Journal of Volcanology and Geothermal Research, 303, 157-174.*

Jónsson, S., Segall, P., Pedersen, R., and Björnsson., G. (2003). Post-earthquake ground movements correlated to pore-pressure transients. *Nature 424, 179-183 (10 July 2003).* doi:10.1038/nature01776.

140

Kelkar, S., Lewis, K., Karra, S., Zyvoloski, G., Rapaka, S., Viswanathan, H., Mishra, P., Chu, S., Coblentz, D., and Pawar, R. (2014). A simulator for modeling coupled thermo-hydro-mechanical processes in subsurface geological media. *International Journal of Rock Mechanics and Mining Sciences, Volume 70, September 2014, Pages 569-580, ISSN 1365-1609, http://dx.doi.org/10.1016/j.ijrmms.2014.06.011.*

Kim, S. K., Bae, G., and Lee, K. K. (2015). Improving accuracy and flexibility of numerical simulation of geothermal heat pump systems using voronoi grid refinement approach. *Geosciences Journal.* doi:10.1007/s12303-014-0061-3.

Kipp, K., Hsieh, P., , and Charlton, S. (2008). Guide to the revised ground-water flow and heat transport simulator: Hydrotherm — version 3. *U.S. Geological Survey Techniques and Methods 6-A25, 160 p.*

Kraft, T. and Deichmann, N. (2014). High-precision relocation and focal mechanism of the injection-induced seismicity at the basel {EGS}. *Geothermics*, 52:59 – 73. Analysis of Induced Seismicity in Geothermal Operations.

Labuz, J. and Zang, A. (2012). Mohr–coulomb failure criterion. *Rock Mech Rock Eng (2012) 45:975–979.* DOI 10.1007/s00603-012-0281-7.

Lay, T. and Wallace, T. (1995). Modern global seismology. *Academic Press, San Diego.*

Lee, C., Kelson, K., and Kang, K. (2000). Hanging wall deformation and its effect on buildings and structures as learned from the chelungpu faulting in the 1999 chi-chi taiwan earthquake. *In: Lo C-H and Liao W-I (eds.) Proceedings of International Workshop Annual Commemoration of Chi-Chi Earthquake, Science Aspect, pp. 93–104. Taipei, Taiwan: National Center for Research on Earthquake Engineering.*

Lin, A., Ren, A., and Wu, X. (2008). Co-seismic thrusting rupture and slip distribution produced by the 2008 mw 7.9 wenchuan earthquake, china. *Tectonophysics. Volume 471, Issues 3-4, 15 June 2009, Pages 203-215.* doi:10.1016/j.tecto.2009.02.014.

Makhnenko, R. and Labuz, J. (2013). Saturation of porous rock and measurement of the b coefficient. *ARMA 13-468.*

Bibliography

Manga, M., Beresnev, I., Brodsky, E. E., Elkhoury, J. E., Elsworth, D., Ingebritsen, S. E., Mays, D. C., and Wang, C.-Y. (2012). Changes in permeability caused by transient stresses: Field observations, experiments, and mechanisms. *Reviews of Geophysics*, 50(2):n/a–n/a. RG2004.

Manga, M. and Brodsky, E. (2006). Seismic triggering of eruptions in the far field: volcanoes and geysers. *Annual Reviews of Earth and Planetary Sciences, vol. 34, 263-291.*

Manga, M., Brumm, M., and Rudolph, M. (2009). Earthquake triggering of mud volcanoes. *Marine and Petroleum Geology, vol. 26, 1785-1798.*

Manga, M. and Wang, C. (2007). Earthquake hydrology. *University of California Berkeley, Berkeley, CA, USA Elsevier B.V.*

Marcaccio, M. and Martinelli, G. (2012). Effects on the groundwater levels of the may-june 2012 emilia seismic sequence. *Ann. Geophys., 55, 4.*

Marsily, G. D. (1986). Quantitative hydrogeology. *Academic Press, Orlando, FL.*

Mavko, G., Mukerji, T., and Dvorkin, J. (1998). The rock physics handbook. *Cambridge University Press.*

Mer, J. L. and Pierre, R. (2001). Production, oxidation, emission and consumption of methane by soils: A review. *Eur. J. Soil Biol., 37(1), 25-50.* doi:10.1016/S1164-5563(01)01067-6.

Miller, S., Collettini, Chiaraluce, L., Cocco, M., Barchi, M., and Kaus, B. (2004). Aftershocks driven by a high-pressure co2 source at depth. *Nature 427 (6976), 724-727.*

Mogi, K., Mochizuki, H., and Kurokawa, Y. (1989). Temperature changes in an artesian spring at usami in the izu peninsula (japan) and their relation to earthquakes. *Tectonophysics, 159, 95–108.*

Moridis, G. and Pruess, K. (1995). Flow and transport simulations using t2cg1, a package of conjugate gradient solvers for the tough2 family of codes. *Lawrence Berkeley Laboratory Report LBL-36235, Berkeley, CA.*

142

Moridis, G. and Pruess, K. (1998). T2solv: An enhanced package of solvers for the tough2 family of reservoir simulation codes. *Geothermics, Vol. 27, No. 4, pp. 415 - 444.*

Narasimhan, T. N. and Witherspoon, P. A. (1976). An integrated finite difference method for analyzing fluid flow in porous media. *Water Resour. Res. 12(1), 57-64.*

Nespoli, M., Rinaldi, A., and Wiemer, S. (2015a). Tough2-seed: A coupled fluid flow mechanical-statistical model for the study of injection-induced seismicity. *PROCEEDINGS, TOUGH Symposium 2015.*

Nespoli, M., Todesco, M., Capaccioni, B., and Cremonini, S. (2015b). Ground heating and methane oxidation processes at shallow depth in terre calde di medolla (italy): Numerical modeling. *J. Geophys. Res. Solid Earth, 120.* 10.1002/2014JB011636.

Nespoli, M., Todesco, M., Serpelloni, E., Belardinelli, M. E., Bonafede, M., Marcaccio, M., Rinaldi, A. P., Anderlini, L., and Gualandi, A. (2015c). Modeling earthquake effects on groundwater levels: evidences from the 2012 emilia earthquake (italy). *GEOFLUIDS.* 10.1111/gfl.12165.

Nostro, C., Stein, R., Cocco, M., Belardinelli, M., and Marzocchi, W. (1998). Two-way coupling between vesuvius eruptions and southern apennine earthquakes, italy, by elastic stress transfer. *J. Geophys. Res., 103(B10), 24487-24504.* doi:10.1029/98JB00902.

Oglesby, D., Day, S., Li, Y.-G., and John, E. (2003). The 1999 hector mine earthquake: The dynamics of a branched fault system. *Bulletin of the Seismological Society of America, Vol. 93, No. 6, pp. 2459–2476, December 2003.*

Okada, Y. (1992). Internal deformation due to shear and tensile faults in a half-space. *Bull. Seism. Soc. Am., 82, No. 2, 1018-1040.*

Oldenburg, C. M., Moridis, G. J., Spycher, N., and Pruess, K. (2004). EOS7C version 1.0: TOUGH2 module for carbon dioxide or nitrogen in natural gas (methane) reservoirs. *Paper LBNL-56589.* doi:10.2172/878525.

Oldenburg, C. M., Pruess, K., and Benson, S. M. (2001). Process modeling of co2 injection into natural gas reservoirs for carbon sequestration and

enhanced gas recovery. *Energy Fuels, 2001, 15 (2), pp 293-298. DOI: 10.1021/ef000247h.*

Ori, G. (1993). Continental depositional systems of the quaternary of the po plain (northern italy). *Sedimentary Geology, 83(1-2), 1–14.* Doi:10.1016/S0037-0738(10)80001-6.

Palchik, V. (2006). Application of mohr-coulomb failure theory to very porous sandy shales. *Int J Rock Mech Mining Sci-43(7):1153-1162.*

Paterson, M. and Wong, T.-F. (2005). Experimental rock deformation. *The brittle field, 2nd edn. Springer-Verlag, Berlin.*

Paull, C., Lorenson, T. D., Borowski, W. S., Ussler, W. I. I. I., Olsen, K., and Rodriguez, N. M. (2000). Isotopic composition of ch4, co2 species, and sedimentary organic matter within samples from the blake ridge: Gas source implications. *Proceedings Ocean Drilling Program, Scientific Results, vol. 164, edited by C. K. Paull et al., pp. 67-78, Ocean Drilling Program, College Station, Tex.* doi:10.2973/odp.proc.sr.164.207.2000.

Peaceman, D. (1977). Fundamentals of numerical reservoir simulation. *Elsevier,Amsterdam, Netherlands.*

Pezzo, G., Boncori, J., Tolomei, C., Salvi, S., Atzori, S., Antonioli, A., Trasatti, E., Novali, F., Serpelloni, E., Candela, L., and Giuliani, R. (2013). Coseismic deformation and source modeling of the may 2012 emilia (northern italy). *Seismological Research Letters Vol, 84, N° 4 July/August.*

Pinder, G. F. and Gray, W. G. (2008). Essentials of multiphase flow in porous media. *Wiley, 258 pages.* ISBN: 978-0-470-31762-4.

Priolo, E., Romanelli, M., Barnaba, C., Mucciarelli, M., Laurenzano, G., Dall'Olio, L., Zeid, N. A., Caputo, R., Santarato, G., Vignola, L., Lizza, C., and Bartolomeo, P. D. (2012). The ferrara thrust earthquakes of may-june 2012: preliminary site response analysis at the sites of the ogs temporary network. annals of geophysics, 55(4). *Géotechnique, 4 (4), 143 -147.* doi:10.4401/ag-6172.

Pruess, K. (1982). Development of the general purpose simulator mulkom. *Report Lawrence Berkeley Laboratory.*

144

Pruess, K., Oldenburg, C., and Moridis, G. (1999). TOUGH2 user's guide, version 2.0. *Paper LBNL-43134.*

Pruess, K., Oldenburg, C., and Moridis, G. (2012). Tough2 user's guide, version 2.1. *Lawrence Berkeley National Laboratory, Berkeley, Calif.*

Rannaud, D., Cabral, A., and Allaire, S. (2008). Modeling methane migration and oxidation in landfill cover materials with tough2-lgm. *Water Air Soil Pollut., 198(1-4), 253-267.* doi:10.1007/s11270-008-9843-4.

Regione-Emilia-Romagna and ENI-AGIP (1998). Riserve idriche sotterranee della regione emilia romagna. *S.EL.CA., Firenze, 119 pp.*

Rice, J. and Cleary, M. (1976). Some basic stress diffusion solutions for fluid-saturated elastic porous media with compressible constituents. *Rev. Geophys. Space Phys. 14, 227–241.*

Rinaldi, A., Rutqvist, J., and Cappa, F. (2014). Geomehcanical effects on co2 leakage through fault zones during large-scale underground injection. *Int. J. Greenh. Gas Contr., 20, 171-131.*

Rinaldi, A., Todesco, M., and Bonafede, M. (2010). Hydrothermal instability and ground displacement at the campi flegrei caldera. *Physics of the Earth and Planetary Interiors*, 178(3-4):155 – 161.

Rinaldi, A., Vandemeulebrouck, J., Todesco, M., and Viveiros, F. (2012). Effects of atmospheric conditions on surface diffuse degassing. *J. Geophys. Res., 117, B11201.* doi:10.1029/2012JB009490.

Rinaldi, A. P., Vilarrasa, V., Rutqvist, J., and Cappa, F. (2015). Fault reactivation during co2 sequestration: Effects of well orientation on seismicity and leakage. *Greenhouse Gas Sci Technol. doi: 10.1002/ghg.1511.*

Roeloffs, E. (1996). Poroelastic techniques in the study of earthquake-related hydrologic phenomena. *Adv. Geophys. 37, 135- 195.*

Roeloffs, E. (1998). Persistent water level changes in a well near parkfield, california, due to local and distant earthquakes. *Journal of Geophysical Research: Solid Earth (1978-2012) Volume 103, Issue B1, pages 869-889, 10 January.*

Bibliography

Roeloffs, E. and Quilty, E. (1996). Water level and strain changes preceding and following the august 4, 1985 kettleman hills, california, earthquake. *Pure Appl. Geophys, Volume 149, Issue 1,pp 21-60.*

Rojstaczer, S., Wolf, S., and Michel, R. (1995). Permeability enhancement in the shallow crust as a cause of earthquake-induced hydrological changes. *Nature, 373, 237-239.*

Romanak, K. D., Bennett, P. C., Yang, C., and Hovorka, S. D. (2012). Process-based approach to co2 leakage detection by vadose zone gas monitoring at geologic co2 storage sites. *Geophys. Res. Lett., 39, L15405,.* doi:10.1029/2012GL052426.

Rutqvist, J. (2011). Status of the tough-flac simulator and recent applications related to coupled fluid flow and crustal deformations. *Computers and Geosciences, Volume 37, Issue 6, June 2011, Pages 739-750, ISSN 0098-3004, http://dx.doi.org/10.1016/j.cageo.2010.08.006.*

Rutqvist, J., Rinaldi, A., Cappa, F., and Moridis, G. (2015). Modeling of fault activation and seismicity by injection directly into a fault zone associated with hydraulic fracturing of shale-gas reservoirs. *J. Petrol. Sc. Eng., 127, 377-386.*

Rutqvist, J., Wu, Y., Tsang, C., and Bodvarsson, G. (2002). A modeling approach for analysis of coupled multiphase fluid flow, heat transfer, and deformation in fractured porous rock. *Int. J. Rock Mech. Min. Sc., 39, 429-442.*

Saibi, H. (2011). 3d numerical model of the obama hydrothermal-geothermal system, southwestern japan. *Computational Geosciences, Volume 15, Issue 4, pp 709-719.*

Samuelson, J. and Spiers, C. (2012). Fault friction and slip stability not affected by co2 storage: Evidence from short-term laboratory experiments on north sea reservoir sandstones and caprocks. *Int. J. Greenh. Gas Contr., 11, S78-S90.*

Scognamiglio, L., Margheriti, L., Mele, F., Tinti, E., Bono, A., Gori, P. D., Lauciani, V., Lucente, F., Mandiello, A., Marcocci, C., Mazza, S., Pintore, S., and Quintiliani, M. (2012). The 2012 pianura padana emiliana seimic

146

sequence: locations, moment tensors and magnitudes. *Annals Of Geophysics, 55(4).* doi:10.4401/ag-6159.

Serpelloni, E., Anderlini, L., Avallone, A., V. Cannelli, V., Cavaliere, A., Cheloni, D., D'Ambrosio, C., D'Anastasio, E., Esposito, A., Pietrantonio, G., Pisani, A., Anzidei, M., Cecere, G., D'Agostino, N., Mese, S. D., Devoti, R., Galvani, A., Massucci, A., Melini, D., Riguzzi, F., Selvaggi, G., and Sepe., V. (2012). Gps observations of coseismic deformation following the may 20 and 29, 2012, emilia seismic events (northern italy): data, analysis and preliminary models. *Ann. Geophys., 55, 4; doi: 10.4401/ag-6168.*

Shapiro, S. and Dinske, C. (2009). Scaling of seismicity induced by non-linear fluid-rock interaction. *J. Geophys. Res., 114, B09307.*

Shapiro, S., Dinske, C., Langebruch, C., and Wenzel, F. (2010). Seismogenic index and magnitude probability of earthquakes induced during reservoir fluid stimulations. *The Leading Edge - Special Section: Microseismic, 304-309.*

Shi, Z., Wanga, G., Wang, C.-Y., Manga, M., and Liu, C. (2014). Comparison of hydrological responses to the wenchuan and lushan earthquakes. *Earth and Planetary Science Letters Volume 391, 1 April 2014, Pages 193-200.* doi:10.1016/j.epsl.2014.01.048.

Shuangyang, L., Yuanming, L., Shujuan, Z., and Deren, L. (2009). An improved statistical damage constitutive model for warm frozen clay based on mohr–coulomb criterion. *Cold Regions Science and Technology Volume 57, Issues 2–3, July 2009, Pages 154–159.* doi:10.1016/j.coldregions.2009.02.010.

Singh, S. K., Ordaz, M., Alcántara, L., Shapiro, N., Kostoglodov, V., Pacheco, J. F., S. Alcocer, C. G., Quaas, R., Mikumo, T., , and Ovando, E. (2000). The oaxaca earthquake of 30 september 1999 (mw = 7.5): A normal-faulting event in the subducted cocos plate. *Seismological Research Letters, January/February 2000, v. 71, p. 67-78.* doi:10.1785/gssrl.71.1.67.

Skempton, A. (1954). The pore-pressure coefficients a and b. *Géotechnique, 4 (4), 143 –147.* doi: 10.1680/geot.1954.4.4.143.

147

Bibliography

Steacy, S., Gomberg, J., and Cocco, M. (2005). Introduction to special section: stress transfer, earthquake triggering, and time-dependent seismic hazard. *J. Geophys. Res., 110(B05S01).* doi:10.1029/2005JB003692.

Sundh, I., Mikkelä, C., Nilsson, M., and Svensson, B. H. (1995). Potential aerobic methane oxidation in a sphagnum dominated wetland—controlling factors and relation to methane emission. *Soil Biol. Biochem., 27, 829-837.*

Todesco, M. (2008). Hydrothermal fluid circulation and its effect on caldera unrest, caldera volcanism, analysis modelling and response. *Edited by Joachim Gottsmann and Joan Martí, chapter 11.*

Todesco, M., Rinaldi, A. P., and Bonafede, M. (2010). Modeling of unrest signals in heterogeneous hydrothermal systems. *Journal of Geophysical Research: Solid Earth. Vol. 115, Issue B9. doi=10.1029/2010JB007474.*

Valley, B. and Evans, K. (2009). Stress orientation to 5 km depth in the basement below basel (switzerland) from borehole failure analysis. *SWISS JOURNAL OF GEOSCIENCES 102(3):467-480.* doi:10.1007/s00015-009-1335-z.

Wang, C., Cheng, L.-H., Chin, C.-V., and Yu, S. (2001). Coseismic hydrologic response of an alluvial fan to the 1999 chi-chi earthquake, taiwan. *Geology; 29;831-834.* doi:10.1130/0091-7613(2001)029<0831:CHROAA>2.0.CO;2.

Wang, C. and Chia, Y. (2008). Mechanism of water level changes during earthquakes: Near field versus intermediate field. *Geophysical Research Letters. GEOPHYS RES LETT 06/2008; 35(12).* DOI:10.1029/2008GL034227.

Wang, C. and Manga, M. (2010). Hydrologic responses to earthquakes and a general metric. *Geofluids (2010) 10, 206-216.* doi: 10.1111/j.1468-8123.2009.00270.x.

Wang, C., Wang, C., and Manga, M. (2004). Coseismic release of water from mountains - evidence from the 1999 (mw=7.5) chi-chi, taiwan earthquake. *Geology, 32, 769-772.*

Wang, C.-y. and Manga, M. (2014). Earthquakes and water. In Meyers, R. A., editor, *Encyclopedia of Complexity and Systems Science*, pages 1–38. Springer New York.

148

Wang, Z., Fukao, Y., and Pei, S. (2009). Structural control of rupturing of the mw7.9 2008 wenchuan earthquake, china. *Earth Planet. Sci. Lett., 279 (2009), pp. 131-138.*

Weingarten, M. and Ge, S. (2014). Insights into water level response to seismic waves: A 24 year high- fidelity record of global seismicity at devils hole. *Geophysical Research Letters 01/2014, 41(1).* doi:10.1002/2013GL058418.

Wessel, P. and Smith, W. (1998). New, improved version of genericmapping tools released. *Eos Trans. AGU, 79, 579.* doi:10.2172/878525.

Whalen, S., Reeburgh, W. S., and Sandbeck, K. A. (1990). Rapid methane oxidation in a landfill cover soil. *Appl. Environ. Microbiol., 56(11),3405-3411.*

Whiticar, M. (1999). Carbon and hydrogen isotope systematics of bacterial formation and oxidation of methane. *Chem. Geol., 161(1-3),291-314.* doi:10.1016/S0009-2541(99)00092-3.

Whiticar, M. and Faber, E. (1986). Methane oxidation in sediment and water column environments-isotope evidence. *Org. Geochem.,10(4-6), 759-768.* doi:10.1016/S0146-6380(86)80013-4.

Wibberley, C. A. and Shimamoto, T. (2003). Internal structure and permeability of major strike-slip fault zones: the median tectonic line in mie prefecture, southwest japan zones. *JOURNAL OF STRUCTURAL GEOLOGY.*

Yale, D. (1984). Network modelling of flow, storage and deformation in porous rocks. *Ph.D. Thesis, Stanford University, Calif.*

Zoback, M. (2010). Reservoir geomechanics. *Cambridge University Press, pp. 449.*